Diese Dissertation haben begutachtet:

Prof. Dr. Albert Young

Prof. Dr. Martin Fertl

DISSERTATION

Systematic Investigation of an RxB Spectrometer's Magnet System

Ausgeführt zum Zwecke der Erlangung des akademischen Grades eines Doktors der technischen Wissenschaften unter Leitung von

Prof. Dr. Eberhard Widmann
Stefan-Meyer Institut für subatomare Physik
der Österreichischen Akademie der Wissenschaften

eingereicht an der Technischen Universität Wien Fakultät für Physik

von
DI Daniel Moser
Matr.-Nr. 1026511
Märzstraße 61/22, 1150 Wien

Ort, Datum

Unterschrift

Abstract

The Standard Model of Particle Physics comprises the basis of our current understanding of particle physics. Even though it has predicted many particles and phenomena, there are limitations to it, illustrated by experiments, that endorse modifications to it. A promising tool to test the Standard Model is the beta decay of the free neutron. Measuring observables in this decay can be used to check the unitarity of the Cabibbo-Kobayashi-Maskawa matrix and to directly search for couplings beyond the Standard Model weak interaction. In this work, we present the NoMoS experiment, which utilizes a novel type of momentum spectrometer, that can be used as a high precision experiment in neutron physics. We discuss the method, design, systematic investigations and give an estimation for the experimental uncertainty in the measurement of the Fierz interference term b in free neutron beta decay.

Zusammenfassung

Das Standardmodell der Teilchenphysik stellt unser derzeitiges Verständnis der Teilchenphysik dar. Obwohl es bisher eine Menge an Teilchen und Phänomenen vorhersagen konnte, zeigen sich seine Limitierungen in immer mehr Experimenten. Ein vielversprechendes Werkzeug um das Standardmodell zu testen, ist der Betazerfall des freien Neutrons. Messungen der Observablen in diesem Zerfall dienen sowohl dazu, die Unitarität der Cabibbo-Kobayashi-Maskawa Matrix zu testen, als auch um direkt nach zusätzlichen Kopplungen in der schwachen Wechselwirkung im Standardmodell zu suchen. In dieser Arbeit präsentieren wir das NoMoS Experiment, welches eine neuartige Methode der Impulsspektroskopie einsetzt und als Hochpräzisionsexperiment im Neutronenbetazerfall genutzt werden kann. Wir erläutern die Methode, das Design, systematische Untersuchungen und geben Abschätzungen zu den experimentellen Unsicherheiten in der Bestimmung des Fierz-Interferenzterms b im Betazerfall des freien Neutrons.

Contents

1. Introduction **7**

2. Theory **10**

2.1. Beta Decay of the Free Neutron 10
2.1.1. The Standard Model Perspective of Neutron Decay 12
2.1.2. Current Friction Points in Neutron Beta Decay 14
2.1.3. Physics Beyond the Standard Model 16
2.2. Charged Particle Motion in Electromagnetic Fields 17
2.2.1. Helical Particle Motion 19
2.2.2. Deviations from the Helical Particle Motion 22
2.3. Algorithms used for Simulations 24
2.3.1. Electric Field 25
2.3.2. Magnetic Field 25
2.3.3. Particle Tracking 27
2.3.4. Numerical Integration 27

3. The NoMoS Experiment **29**

3.1. Measurement Principle 29
3.1.1. Comparison to Conventional Magnetic Spectroscopy 29
3.1.2. Application for other Beta Decays 30
3.2. Features 32
3.2.1. Decay Volume 32
3.2.2. Filter 32
3.2.3. Aperture 34
3.2.4. $R \times B$ Drift Region 34
3.2.5. Detection Region 34
3.3. Magnetic Field in NoMoS 35
3.4. Detection System 36
3.4.1. $R \times B$ Drift Detector 36
3.4.2. Secondary Detection System 36
3.5. Design Considerations 37
3.5.1. Conductor Technology 37

3.5.2. $R \times B$ Coil Geometry . . . 38
3.5.3. Measurement Sites and Statistics . . . 43
3.5.4. Overall Cost . . . 47
3.5.5. Featured Configurations . . . 50
3.6. The Transfer Principle . . . 50
3.6.1. The Transfer Function . . . 50
3.6.2. Input Functions . . . 51
3.6.3. Systematic Weighting Functions . . . 51
3.7. Systematic Effects . . . 52

4. Ingredients of the Transfer in NoMoS **54**
4.1. Input Functions . . . 54
4.1.1. Decay Spectrum . . . 55
4.1.2. Neutron Beam Profile . . . 55
4.2. Systematic Effects with Weighing Character . . . 56
4.2.1. Aperture Edge Effect . . . 57
4.2.2. Backscattering at Main Detector . . . 57
4.3. Particle Motion in the Transfer Function . . . 58
4.3.1. $R \times B$ Drift: Radial Magnetic Field Gradient . . . 58
4.3.2. Adiabatic Particle Motion . . . 59
4.4. Complete Transfer Equations . . . 61
4.5. Transfer and its Properties . . . 66
4.5.1. The Transfer Explicitly Put Together . . . 66
4.5.2. The Order of the Integration and Behaviour of the Integrand 68
4.5.3. The Integrand I_6 Dependent on p_e . . . 70
4.5.4. Subsequent Integration Dimensions . . . 74

5. Systematic Effect Investigations **76**
5.1. Methodology of Investigation . . . 76
5.1.1. (Modified) Magnetic Field Lines . . . 77
5.1.2. (Monte Carlo) Particle Tracking . . . 83
5.1.3. Mimicking Observable Deviation by Systematic Parameter Uncertainty . . . 84
5.2. Determining Systematic Parameters . . . 88
5.2.1. With (Modified) Magnetic Field Lines . . . 88
5.2.2. With Systematic Particle Tracks . . . 95
5.2.3. Full Monte Carlo Simulations . . . 98
5.2.4. Measurements during Experimental Runs . . . 104
5.3. Interconnecting the Transfer Function with Monte Carlo Data . . . 106
5.4. Systematic Parameter Sensitivities with the Transfer Function . . . 110
5.4.1. Collection of Systematic Effect Sensitivities . . . 110

5.4.2. Dependence of Sensitivities on Second Parameters 114
5.4.3. Additional Fit Parameters 115
5.5. Ideas for Testing Systematic Effects in the Experiment 115
5.5.1. Curvature Angle α 116
5.5.2. Modifying Magnetic Field Ratios 116
5.5.3. Changing the Aperture Opening 116

6. Summary **117**

7. Outlook into Further Investigations **119**
7.1. Modifications to the Transfer 119
7.1.1. Angular B-Field Gradient in the $R \times B$ Region 119
7.1.2. Considering the first order drift movement in the curvature vector $\vec{R}$ 120
7.1.3. Earth Magnetic Field 122
7.1.4. Magnetic Field Inhomogeneities 123
7.2. Investigations with Particle Tracking 124
7.2.1. Non-Adiabatic Pitch Angle Increase in the $R \times B$ Region . . 124
7.2.2. Phase Angle Relations 128

A. Coil Set-Up Data **132**

B. Systematic Parameters of the Super-conducting System **138**

C. Thoughts on Magnetic Field Measurement in NoMoS **140**
C.1. Magnetic Sield Sensors 140
C.2. Positioning of the Sensors 140

Bibliography **142**

1. Introduction

The current basis of our understanding of fundamental particle physics is well described within the Standard Model of Particle Physics (SM). It successfully predicted a plethora of particles and phenomena in the past. Presently, it consists of quantum field theories of the strong, the weak and the electromagnetic interaction. Nonetheless, some recent discoveries demonstrate the limitations of the SM in its current form. Significant extensions of the SM are required to explain for example the neutrino mass, both dark matter and dark energy, or the baryon asymmetry. These possible extensions include additional couplings in the interactions, indicating new particles like additional bosons, leptoquarks or super-symmetric particles.

A wide variety of experiments probing the vast phenomena of nature can be conducted to both test the Standard Model as well as to directly search for Beyond Standard Model (BSM) physics. In the high energy sector, colliders like the LHC at CERN explore the remnants of high energy particle collisions. At the low energy precision frontier, experiments try to find small effects in fundamental processes. A particularly interesting one is the weak beta decay. Through its decay products, it provides an abundance of observables that can be used to test the SM and search for BSM physics.

The weak interaction is described using weak eigenstates, which are transformed from the mass eigenstates using the Cabibbo-Kobayashi-Maskawa(CKM)-matrix [KM73]. This indicates the possibility of flavour mixing of quarks in this interaction. A striking test of the SM is to determine the elements of the CKM-matrix from weak decay observations and check the unitarity of the matrix (it is unitary by design) [A$^+$10]. Furthermore, one can derive limits on BSM couplings by observing the decays' observables. The SM tests are currently most accurately performed using super-allowed nuclear $0^+ \rightarrow 0^+$ decays [HT15, HT18]. Nonetheless, they are dependent on nuclear corrections and due to the fact that they are pure Fermi decays, they are not sensitive to potential tensor couplings in the weak interaction (but only sensitive to potential scalar couplings). An attractive alternative, that has no nuclear corrections and high sensitivity to both scalar and tensor couplings, is the decay of the free neutron [G$^+$95].

The beta decay of the free neutron is a purely leptonic decay with only first generation particle participants. The transition is a mixed Fermi and Gamow-Teller one. A neutron decays into a proton (transforming a down into an up-quark), emitting a W^- boson, further decaying into an electron and an electron-antineutrino with a mean lifetime of $\tau_\mathrm{n} = 879.4 \pm 0.6$ s [Z+20](Particle Data Group). The Hamiltonian for this interaction in the SM is restricted by the V-A theorem (based on experiments by Wu et al. [WAH+57] and Goldhaber et al. [GGS58]) and can be written as [LY56, FGM58]

$$\mathcal{H}_\mathrm{W} = \frac{1}{\sqrt{2}} \left[\bar{\psi}_\mathrm{p} \gamma_\mu \left(C_\mathrm{V} + C_\mathrm{A}\gamma^5\right) \psi_\mathrm{n}\right] \left[\bar{\psi}_\mathrm{e} \gamma_\mu \left(1 - \gamma^5\right) \psi_\nu\right]$$

While the Hamiltonian $\mathcal{H}_\mathrm{W}$ will be discussed in more detail in the theory chapter 2, it highlights the coupling coefficients C_V and C_A for the vector and axial-vector terms, which enable parity violation in the decay.

Most neutron decay observables in the SM only depend on the ratio of axial-vector to vector couplings $\lambda = C_\mathrm{A}/C_\mathrm{V} = L_\mathrm{A}/L_\mathrm{V}$ (the L_i are the left-handed couplings on nucleon level and implicitly contain nuclear and radiative corrections [Sha71]). There is a master formula, relating the mean lifetime and the ratio λ to the corresponding matrix element of the CKM matrix, V_ud, shown below [CMS04, CMS19]

$$|V_\mathrm{ud}|^2 \tau_\mathrm{n} (1 + 3|\lambda|^2) = \text{const.}$$

This nicely illustrates, that by measuring the mean lifetime and determining λ from any of the variety of other decay observables, V_ud can be determined, a critical input to a CKM unitarity test for couplings to the up quark. λ is currently most precisely determined (on the 10^{-3} level [Z+20]) by measurements of the electron asymmetry correlation coefficient A (also on the 10^{-3} level [Z+20]). One alternative observable for a λ determination, that can both be measured by an asymmetry measurement and spectroscopy of the decay's proton spectrum, is the electron-antineutrino correlation coefficient a. The aSPECT collaboration has resently published a measurement of a with an unprecedented precision of $\Delta a/a = 0.8\,\%$ [B+20], also reaching the 10^{-3} level in the determination of λ. The Nab experiment aims to further improve this with an ultimate goal of $\Delta a/a \sim 0.1\,\%$ [F+18].

The neutron decay observables can also be used to give limits on non-SM couplings, like scalar and tensor couplings. One particularly interesting observable is the so-called Fierz interference term b, which is zero in the SM. It is linearly dependent on scalar and tensor couplings, giving high sensitivity to them [GANC16]. It can

be determined from electron decay spectroscopy as well as from energy dependent electron asymmetry $A(E_e)$ measurements (systematic uncertainty due to uncertainties in the calibration and detector efficiency are strongly suppressed compared to the former method). The UCNA collaboration performed energy spectroscopy [H$^+$17a, H$^+$17b] ($\Delta b = \pm 0.09$) as well as an energy dependent electron asymmetry measurement [S$^+$20b] ($\Delta b = \pm 0.048$) whereas the PERKEO collaboration [SRA$^+$20] determined b from beta asymmetry data ($\Delta b = \pm 0.021$). All results are compatible with zero.

In this work, we present a novel type of momentum spectrometer, intended to measure the spectra of the neutron decay's charged products, the electron and proton. It is called NoMoS, the Neutron decay prOducts Momentum Spectrometer. It is based on an idea by Lobashev [Lob98], using a curved magnetic field to spread particles according to their momentum. The effect used is the $R \times B$ drift, a drift derived from the gradient drift. That is why we call this type of momentum spectrometer an $R \times B$ spectrometer. With NoMoS, we aim to measure a and b in a first goal with an accuracy of $\Delta a/a \lesssim 1\,\%$ and $\Delta b \lesssim 6 \times 10^{-3}$, respectively, and in the long term with an ultimate accuracy of $\Delta a/a < 0.3\,\%$ and $\Delta b < 10^{-3}$, respectively. Furthermore, additional observables are planned, like the weak magnetism constant κ, not determined so far in neutron beta decay.

The scope of this work is as follows: First, we discuss the theory behind this experiment and motivate it further in Chapter 2. This chapter also includes fundamentals of particle dynamics, providing an important foundation for all further discussions. In Chapter 3, we present the experiment NoMoS with all its features and intricacies, highlighting important design considerations. A powerful tool, used to investigate almost all systematic effects in NoMoS, is the so-called Transfer function. It uses analytic assumptions about the particle transport and convolves input functions numerically into a drift distance spectrum at the detector. This mechanism is examined in-depth in Chapter 4. The overall results of our systematic investigations of NoMoS are presented in Chapter 5, where we focus on electrons (determination of the Fierz inferference term b). The protons require further investigations into post-acceleration and detector technology and will therefore be covered in later works. In the end, we give a summary as well as an outlook into more detailed systematic effects for higher accuracy in Chapters 6 and 7, respectively.

2. Theory

In this chapter, we first discuss the theoretical background of the NoMoS experiment in Sec. 2.1, concisely introducing the weak interaction. This includes a discourse about the process of neutron beta decay, its properties within the SM and BSM with current friction points, as well as the observables to motivate their measurement. Furthermore, Sec. 2.2 deals with the principles behind charged particle motion in electromagnetic fields. A proper understanding in this regard is required for the consideration of most systematic effects in this work. Last but not least, the algorithms used for field calculations, particle tracking as well as numerical integration are presented in Sec. 2.3.

2.1. Beta Decay of the Free Neutron

The beta decay of the free neutron is well described within the V - A theory of the weak interaction in the SM (experimentally indicated by Wu et al. [WAH$^+$57] and Goldhaber et al. [GGS58] and written down by Lee and Yang [LY56] and Feynman and Gell-Mann [FGM58]). The corresponding bosons of the weak interaction are the two charged W^- and W^+ as well as the neutral Z^0 boson, respectively. The states of interaction are not the mass eigenstates but rather weak eigenstates, given by a mixing matrix, called Cabibbo-Kobayashi-Maskawa(CKM)-matrix, showing the ability of the weak interaction to change the flavour in its processes. The neutron decays into a proton (turning a down-quark into an up-quark), emitting a W^- boson, which further decays into an electron and an electron-anti-neutrino with a mean lifetime of $\tau_\mathrm{n} = 879.4 \pm 0.6$ s [Z$^+$20] (Particle Data Group).

The SM Hamiltonian for this interaction $\mathcal{H}_\mathrm{W}$, consisting of vector minus axial-vector terms is shown below

$$\mathcal{H}_\mathrm{W} = \frac{1}{\sqrt{2}} \left[\bar{\psi}_\mathrm{p} \gamma_\mu \left(C_\mathrm{V} + C_\mathrm{A}\gamma^5\right) \psi_\mathrm{n}\right] \left[\bar{\psi}_\mathrm{e} \gamma_\mu \left(1 - \gamma^5\right) \psi_\nu\right]$$

The Hamiltonian $\mathcal{H}_{\mathrm{W}}$ includes the wave functions ψ_{p}, ψ_{n}, ψ_{e} and ψ_{ν} for the proton, neutron, electron and electron-anti-neutrino, respectively as well as the gamma matrices γ_{μ} and γ^5. The first term is the hadronic part whereas the second part is leptonic. The coefficients C_{V} and C_{A} are general couplings for the vector and axial-vector term, respectively, and can be written dependent on the weak Fermi coupling constant G_{F} and the corresponding CKM-matrix element V_{ud} according to

$$C_{\mathrm{V}} = G_{\mathrm{F}} V_{\mathrm{ud}} g_{\mathrm{V}}, \quad C_{\mathrm{A}} = G_{\mathrm{F}} V_{\mathrm{ud}} g_{\mathrm{A}}. \tag{2.1}$$

g_{V} and g_{A} should not be confused with the coupling constants on quark level, which is why we use the variable L_i instead, also indicating the left-handedness of the SM. The coefficients L_{V} and L_{A} implicitly include nuclear and radiative corrections [Sha71].

A general (model independent) formula for the differential decay probability $\mathrm{d}^3\Gamma$ can be derived from Fermi's Golden Rule leading to [JTW57a, JTW57b]

$$\begin{aligned} \mathrm{d}^3\Gamma &= \mathcal{W}(E_{\mathrm{e}}) \frac{1}{(2\pi)^5} \frac{G_{\mathrm{F}}^2 |V_{\mathrm{ud}}|^2}{2} p_{\mathrm{e}} E_{\mathrm{e}} (E_0 - E_{\mathrm{e}})^2 dE_{\mathrm{e}} d\Omega_{\mathrm{e}} d\Omega_{\nu} \\ &\times \xi \left[1 + a \frac{\boldsymbol{p}_{\mathrm{e}} \cdot \boldsymbol{p}_{\boldsymbol{\nu}} c^2}{E_{\mathrm{e}} E_{\nu}} + b \frac{m_{\mathrm{e}} c^2}{E_{\mathrm{e}}} + \frac{\langle \boldsymbol{s}_{\mathrm{n}} \rangle}{s_{\mathrm{n}}} \cdot \left(A \frac{\boldsymbol{p}_{\mathrm{e}} c}{E_{\mathrm{e}}} + B \frac{\boldsymbol{p}_{\boldsymbol{\nu}} c}{E_{\nu}} + D \frac{\boldsymbol{p}_{\mathrm{e}} \times \boldsymbol{p}_{\boldsymbol{\nu}} c^2}{E_{\mathrm{e}} E_{\nu}} \right) \right] \end{aligned} \tag{2.2}$$

Here, $\mathcal{W}(E_{\mathrm{e}})$ is a correction factor containing recoil-order, radiative and Coulomb corrections, G_F is the weak Fermi coupling constant, V_{ud} the upper left element of the Cabibbo-Kobayashi-Maskawa(CKM)-Matrix, p_{e}/p_{ν} and E_{e}/E_{ν} denote the momenta and energies of the electron/neutrino, respectively, E_0 is the maximum electron energy, m_{e} the electron mass, $\boldsymbol{s}_{\mathrm{n}}$ the neutron spin, $d\Omega_{\mathrm{e}}/d\Omega_{\nu}$ the solid angle differential factors of electron/neutrino, c the speed of light and ξ a factor, that is reciprocally proportional to the neutron decay rate. Figure 2.1 shows schematically the neutron beta decay and the attribution of the correlation coefficients a, A, B, C and D. The proton asymmetry C can be expressed by A and B (due to kinematics) and is therefore not part of Eq. 2.2. b is the Fierz interference term. These coefficients in turn are dependent on more fundamental parameters of a specific model. If one also considers the spin of the electron, further correlation coefficients appear.

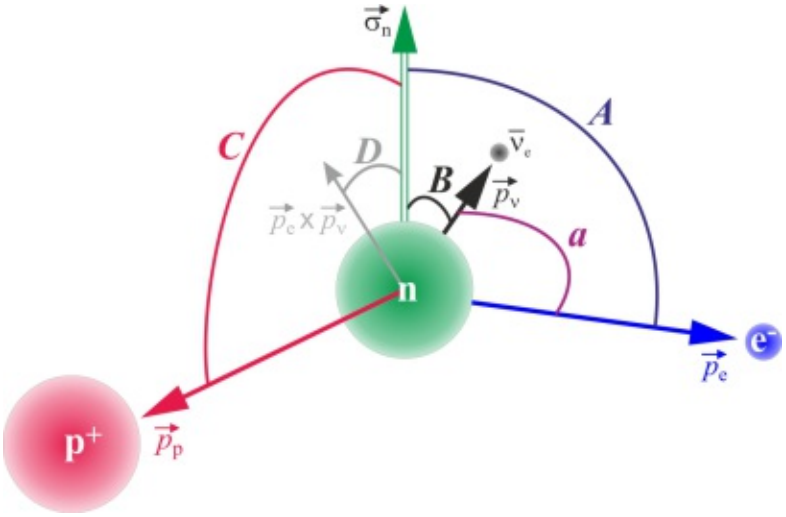

Figure 2.1.: A schematic view of the neutron beta decay. The angular correlation coefficients of the decay's products, a, A, B, C and D are shown relative to the neutron spin [Kon11].

2.1.1. The Standard Model Perspective of Neutron Decay

In the SM, all correlation coefficients can be expressed solely in terms of the ratio of axial-vector to vector coupling constant $\lambda = L_A/L_V$, e.g. the electron anti-neutrino correlation coefficient a

$$a = \frac{1-\lambda^2}{1+3\lambda^2}. \tag{2.3}$$

The measurement of a correlation coefficient such as a can be used to test the SM. If the differential decay probability (Equ. 2.2) is integrated over the solid angles and the electron energy, the following equation is obtained [CMS04]

$$|V_{ud}|^2 \tau_n (1+3L_A^2) = \text{const.} \tag{2.4}$$

In this equation, the conservation of vector currents (CVC) of the SM was used ($L_V = 1$ and therefore $\lambda = L_A$). The equation shows that, if the mean lifetime τ_n and any correlation coefficient determining λ, are measured, V_{ud} can be determined, compared to other results and used in the unitarity tests of the CKM-matrix (see Equ. 2.5 for the first row unitarity test, which should hold by design of the CKM-matrix).

$$|V_{\mathrm{ud}}|^2 + |V_{\mathrm{us}}|^2 + |V_{\mathrm{ub}}|^2 \stackrel{?}{=} 1 \tag{2.5}$$

The constant on the right side of Equ. 2.4 contains theoretical calculations of radiative corrections. The measurement of different correlation coefficients provides different perspectives, sensitivities and independent approaches to the determination of λ.

Due to kinematic conservation laws, a and therefore λ also influence the proton energy spectrum. This dependency is not trivial, yet, the Nachtmann approximation of the proton energy spectrum [Nac68, D$^+$00] provides a simple formula, illustrating the approximate dependency

$$\omega_p(T_p) \propto g_1(T_p) + a \cdot g_2(T_p) \tag{2.6}$$

with two proton kinetic energy T_p dependent functions g_1 and g_2 that result from the Nachtmann model. This influence on the proton energy spectrum is the basis of the λ determination with an $R \times B$ spectrometer such as NoMoS.

Experimental Status

Currently (PDG 2020), the best determination of λ is given solely by measurements of the electron asymmetry A ($\lambda = -1.2756 \pm 0.0013$, $\Delta\lambda/\lambda \approx 1 \times 10^{-3}$ [Z$^+$20]) with the formula of A given below

$$A = -2\lambda \frac{1+\lambda}{1+3\lambda^2}. \tag{2.7}$$

Nonetheless, a recent new result by the aSPECT collaboration of the electron-antineutrino coefficient a with previously unreached precision ($\Delta a/a = 0.8\%$) improves this alternative determination of λ significantly (new mean value $\lambda_a = -1.2686 \pm 0.0020$, $\Delta\lambda_a/\lambda_a \approx 1.6 \times 10^{-3}$ from PDG including aSPECT 2019 [Z$^+$20, B$^+$20]). Note, that the value of λ determined by the aSPECT collaboration differs by more than two sigma from the current Particle Data Group value (determined from beta asymmetry measurements).

This illustrates the importance of further independent measurements of a to determine λ. Furthermore, the electron-antineutrino coefficient a has different sensitivities to BSM physics compared to the electron asymmetry A [FGANC20].

An accurate determination of λ even has implications for the field of cosmology [DS11]. It inter alia is connected to baryogenesis, emphasizing the importance of neutron beta decay experiments even in other fields of study. NoMoS aims for a measurement with an ultimate accuracy of $\Delta a/a < 0.3\%$.

2.1.2. Current Friction Points in Neutron Beta Decay

Currently, there are multiple friction points in the SM in relation to the neutron beta decay, that motivate more independent measurements of the SM-observables. NoMoS provides a completely new and independent approach to this with an $R \times B$ spectrometer to measure the momentum spectra of the charged decay products.

CKM Unitarity Friction

V_{ud} is currently best determined by experiments of nuclear super-allowed $0^+ \rightarrow 0^+$ decays [HT15, HT18, Z$^+$20]

$$|V_{\mathrm{ud}}|^2 = 0.97148(20)/(1 + \Delta_{\mathrm{R}}^{\mathrm{V}}) \tag{2.8}$$

with the inner or universal electroweak radiative correction (RC) $\Delta_{\mathrm{R}}^{\mathrm{V}}$. Recent approaches to calculating this correction [S$^+$18a, S$^+$20a, CMS19] are roughly consistent with each other but larger than the 2018 PDG value. Using the most precise calculation through a dispersion relation calculation approach [S$^+$18a], V_{ud} is obtained as

$$V_{\mathrm{ud}} = 0.97370(10)_{\mathrm{exp.,nucl.}}(10)_{\mathrm{RC}}. \tag{2.9}$$

This value is roughly 2σ lower than the 2018 value and seems to violate the first row CKM unitarity. Further theoretical investigations of the RC and more independent experiments for the determination of V_{ud} have to be conducted to clarify this tension. Alternatively, V_{ud} can also be determined from neutron beta decay, nuclear mirror decays and pion decay. Neutron beta decay in particular provides an interesting alternative as it doesn't require nuclear corrections and still has potential to reduce experimental errors. Using Equ. 2.4, V_{ud} can be determined from measurements of the neutron lifetime τ_{n} and determination of the coupling ratio λ.

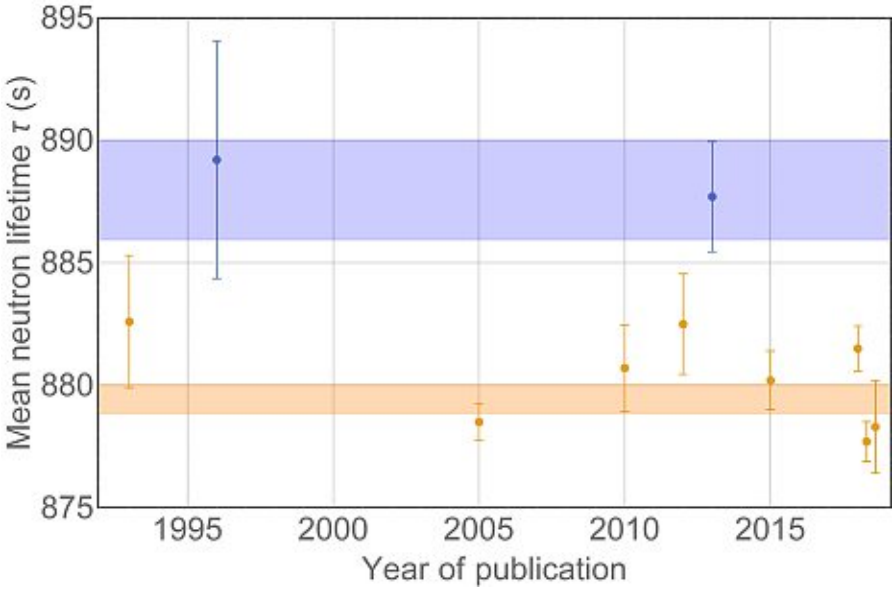

Figure 2.2.: Illustration of the mean lifetime measurement results from the two different methods through the years of publication, with their respective mean value and error bar [Z+20]. The bottle experiments are indicated in orange with the lower mean lifetimes, whereas the beam experiments retrieved higher values, indicated in blue.

Discrepancy in the Neutron Mean Lifetime

There are mainly two different methods to measure the neutron mean lifetime, bottle and beam experiments [WG11]. On the one hand, bottle experiments trap ultracold neutrons (gravitationally, magnetically etc.) and count the surviving neutrons at multiple times after filling the trap [S+05, PVSG10, S+12, A+15, SKF+18, P+18, E+18]. On the other hand, beam experiments count the decay products from a known neutron flux [B+96, Y+13]. Interestingly, results of these two different types of experiments have a significant discrepancy ($\approx 4\sigma$) (see Fig. 2.2).

There are multiple possible explanations ranging from experimental error to new physics (resulting in exotic decay channels and therefore missing decay products in beam experiments - which only look at the charged decay products) [Ber19, DSM+19, Tan19, Wie18, S+18b, Ser19, FG18, CMS18, CMS19, KJM+19]. Some of the proposed exotic decay branches and their current experimental limits are discussed in [FG20]. Clearing up this discrepancy and increasing the accuracy of the neutron mean lifetime is of utmost importance to better test the SM and to

search for physics beyond the SM.

Currently, multiple experiments try to tackle this discrepancy by reducing experimental errors and measuring the mean lifetime of the neutron with higher accuracy and systematically independent, like the τSPECT [Kar17], UCNτ [P$^+$19] and BL2 experiment [H$^+$19]. Furthermore, more independent approaches are proposed [Wei20].

λ Trend over Time

Another interesting observation is a time-dependent trend in λ determined by correlation coefficient measurements (values taken from electron asymmetry A measurements). There is a 5σ discrepancy between measurements conducted before 2002 versus after that year. A probable explanation is poor understanding of systematic uncertainties. Clearly, more independent determinations of λ should be conducted both by different experiment types and observables to shed more light on this matter.

2.1.3. Physics Beyond the Standard Model

There is a multitude of extensions to the SM, trying to tackle the short-comings of it [Her01, GANCS19, FGANC20]. One way is to assume additional couplings in the interaction, e.g. left-handed scalar and tensor interactions (L_S and L_T). This not only changes the correlation coefficients in their parameter dependence but also gives raise to observables, that would otherwise be zero. Equation 2.10 shows a assuming additional left-handed scalar and tensor couplings with the new parameter dependencies $x = L_\mathrm{S}/L_\mathrm{V}$ and $y = L_\mathrm{T}/L_\mathrm{A}$.

$$a = \frac{1 + \lambda^2 y^2 - x^2 - \lambda^2}{1 + x^2 + 3\lambda^2 y^2 + 3\lambda^2} \tag{2.10}$$

Even more, the so-called Fierz interference term b, which is zero in the SM, has contributions in this SM-extension.

$$b = 2\gamma \frac{x + 3y\lambda^2}{1 + x^2 + 3\lambda^2 y^2 + 3\lambda^2} \tag{2.11}$$

with the electromagnetic gamma factor $\gamma = \sqrt{1-(Z\alpha)^2}$ [SBNC06]. Especially its linear dependence on the non-SM parameters makes it sensitive to them. Integrating over the solid angles of Equ. 2.2, the effect of the Fierz term can be shown with the following approximation

$$\Gamma \approx \left(1 + b\frac{m_e}{E_e}\right)\Gamma_{\mathrm{SM}} \tag{2.12}$$

with the modified decay rate Γ compared to the SM decay rate Γ_{SM} (there is a well-understood Standard Model $1/E_{\mathrm{e}}$ dependent contribution at recoil order [BCC+12]). A measurement of the correlation coefficient B and b from neutron beta decay as well as b from ^{6}He on the 10^{-3}-level lead to similar prospective constraints as high energy physics ($\sqrt{s} = 14$ TeV) on scalar and tensor couplings in the weak interaction [B+16, GANCS19]. Furthermore, neutron decay is a mixed decay (in contrast to the pure Gamow-Teller super-allowed decays), resulting in a significant advantage in the sensitivity to tensor currents.

A first published measurement of b from energy spectroscopy was conducted by the UCNA collaboration [H+17a] ($b = 0.067(5)_{\mathrm{stat}}\binom{+90}{-61}_{\mathrm{sys}}$). The same collaboration later extracted the Fierz term from an energy-dependent electron asymmetry measurement with increased precision [S+20b] ($b = 0.066(41)_{\mathrm{stat}}(24)_{\mathrm{sys}}$). Another value is given by the PERKEO collaboration from a correlated determination with λ from a measurement of the electron asymmetry A [SRA+20] ($b = 0.017(20)_{\mathrm{stat}}(3)_{\mathrm{sys}}$). All results are fully compatible with the SM assumption $b = 0$. More accurate measurements of b are required to give more stringent constraints on L_{S} and L_{T}. NoMoS aims at an ultimate accuracy of $\Delta b < 10^{-3}$.

2.2. Charged Particle Motion in Electromagnetic Fields

A major part of this work's investigations require an extensive understanding of charged particle motion in electromagnetic fields. Not only does it serve as a basis for all analytic estimations of particle transport, but also for the numeric particle tracking. In this section, we will present the most fundamental relations required in charged particle transport as well as interesting derived quantities.

The Lorentz Force

In general, charged particle motion in electromagnetic fields is governed by the Lorentz force $\vec{F}_\mathrm{L}$ [Jac99]

$$\vec{F}_\mathrm{L} = q\left(\vec{E} + \vec{v} \times \vec{B}\right) \tag{2.13}$$

with the particle's charge q. It shows a force in the direction of the electric field $\vec{E}$ (subsequently also called E-field) as well a contribution perpendicular to the particle velocity $\vec{v}$ and the magnetic flux density $\vec{B}$ (which we subsequently call magnetic field or B-field). This fundamental relation provides us with a plethora of derived quantities that are of use to us.

Magnetic Flux Conservation

In the Standard Model, there are no magnetic monopoles. This statement is equivalent to $\boldsymbol{\nabla \cdot B} = 0$, Gauss's law for magnetism within the Maxwell equations [Jac99]. This leads to flux conservation of this vector field [Leh64]. The conserved magnetic flux Φ_B can be written as

$$\Phi_B = BA = \text{const.} \tag{2.14}$$

showing that the magnetic field B times a cross section A perpendicular to the vector field is constant. This formula inter alia leads to an analytic description of the local adiabatic pitch angle of a particle in the following sections.

Magnetic Field Lines

Every magnetic vector field $\vec{B}$ can be described in terms of two scalar functions α and β according to [Leh64]

$$\vec{B} = \nabla\alpha \times \nabla\beta \tag{2.15}$$

with the nabla operator or gradient ∇. So-called magnetic field lines are generated by the intersections between the surfaces $\alpha = \text{const.}$ and $\beta = \text{const.}$ and every field line can be specified by a certain pair of values α and β. These magnetic field lines illustrate the magnetic flux of the magnetic flux density $\vec{B}$ and are tightly connected to the magnetic flux conservation. A numerical approach to calculating the field lines is given in Ch. 5.

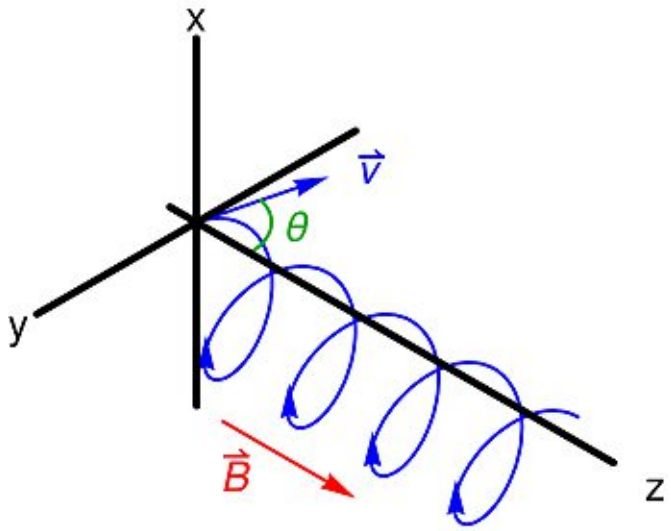

Figure 2.3.: Illustration of the basic helical motion of a charged particle in a magnetic field $\vec{B}$ (red). The path of the particle is depicted in blue and the pitch angle θ of the velocity $\vec{v}$ (blue) with respect to the B-field in green.

2.2.1. Helical Particle Motion

In the absence of an electric field, a charged particle performs a helical motion following a magnetic field line (Equ. 2.13 shows that the force direction is perpendicular to the magnetic field vector, therefore the particle's velocity in B-field direction is not affected). This helical motion can be described with a transversal and a perpendicular component relative to the B-field. The transversal velocity stays unaltered, defining the motion of the so-called guiding center. This guiding center will in first order follow the local magnetic field line. The Lorentz force leads to a gyrating motion of the particle around this guiding center - the perpendicular component - which is described by the local phase angle ϕ. The gyrating motion is illustrated in Fig. 2.3.

The gyration radius r_{G} is given by [Jac99]

$$r_{\mathrm{G}} = \frac{p \sin\theta}{qB} \tag{2.16}$$

with the relativistic momentum p and the pitch angle θ, whereas the gyration

frequency ω_G is

$$\omega_G = \frac{qB}{\gamma m} \tag{2.17}$$

with the relativistic factor γ and the particle's rest mass m. The pitch height h of the gyration is given by

$$h = \frac{2\pi p}{B} \cos\theta \tag{2.18}$$

Adiabaticity

Under specific circumstances, the motion of a charged particle in an electromagnetic field can be described by a set of analytic equations. The conditions are met for relative field gradients significantly smaller than 1 ($\Delta E/E << 1$, $\Delta B/B << 1$) during one gyration. There are multiple quantities that are conserved during this so called adiabatic particle motion, e.g. the magnetic moment μ [Leh64]

$$\mu = \frac{T_\perp}{B} \tag{2.19}$$

with the perpendicular kinetic energy component. As soon as general inhomogeneities are introduced, additional drifts appear. These sometimes can be approximated analytically as an effective drift acting on the adiabatic guiding center motion.

Adiabatic Change of Particle Properties

Using Equ. 2.14 and 2.16, one can derive a description of the local pitch angle θ dependent on the local magnetic field in the adiabatic limit [Jac99]

$$\frac{\sin^2\theta_0}{\sin^2\theta_1} = \frac{B_0}{B_1} \tag{2.20}$$

where we used $v_\perp = \sin\theta$ and $v_\parallel = \cos\theta$ for the two velocity components relative to the B-field. This relation inter alia shows that an increasing magnetic field leads to an increasing pitch angle, which in the extreme case results in the reflection of the particle (magnetic mirror effect). This can be shown by setting $\theta_1 = 90°$, giving

$$\sin\theta_{\max} = \sqrt{\frac{B_0}{B_{\max}}}, \tag{2.21}$$

the critical initial pitch angle, not being able to overcome a magnetic field maximum $B_{\max}$ anymore.

Furthermore, Equ. 2.14 shows how a group of magnetic field lines surrounded by the perpendicular cross-section A (a magnetic flux tube), will change its cross-section with B (the field lines gather or spread out from each other in the perpendicular coordinate). Using a circular form with cross section $A = r^2\pi$, it is easy to derive that

$$r_1 = r_0\sqrt{B_0/B_1} \tag{2.22}$$

or with the magnetic field ratio $r_B = B_1/B_0$

$$r_1 = r_0\sqrt{1/r_B} \tag{2.23}$$

with the indices depicting two different positions 0 and 1. A circle with radius r_0 will change to r_1 according to Equ. 2.23 when followed from position 0 to 1. This analytic description of a magnetic flux tube changing its cross section can be used to describe a particle's guiding center that follows a magnetic field line at radial position r_0.

Acceleration due to Electric Potential

In the presence of an electric field in addition to a magnetic field, the charged particle experiences an acceleration in direction of $\vec{E}$ on top of the helical motion. In the adiabatic limit and the special case of $\vec{E} \parallel \vec{B}$, analytic descriptions of the particle properties can be found. The position (here z) dependent adiabatic parallel kinetic energy component $T_\parallel^{\mathrm{ad}}(z)$ is

$$T_\parallel^{\mathrm{ad}}(z) = T_0 - q(U(z) - U_0) - \frac{B(z)}{B_0}T_0\sin^2\theta_0 \tag{2.24}$$

with the initial kinetic energy T_0, the position dependent electric potential $U(z)$ as well as its reference value at the initial position U_0, the magnetic field strength at position z, $B(z)$ and its reference value B_0 and the incident pitch angle θ_0. The first part of Equ. 2.24 describes the acceleration due to the electric potential whereas the second part considers the change of the parallel kinetic energy component due

to changes in the magnetic field B. The local pitch angle $\theta(z)$ can be described analogously

$$\sin^2\theta(z) = \frac{B(z)}{B_0}\frac{T_0\sin^2\theta_0}{T_0 - q(U(z) - U_0)} \tag{2.25}$$

2.2.2. Deviations from the Helical Particle Motion

For significant field gradients or the fields not aligned with each other, additional drifts appear. For small enough disturbances, approximate descriptions of the drifts can be found.

The $E \times B$ Drift

Charged particles in an electromagnetic field experience the so-called $E \times B$ drift [Jac99], if the electric field is not aligned with the magnetic field. This can be seen in the equation for the drift velocity $\vec{v}_{E\times B}$

$$\vec{v}_{E\times B} = c\frac{\vec{E}\times\vec{B}}{B^2} \tag{2.26}$$

where the cross product vanishes if the vectors are parallel. For electrons, this effect is negligible as their usual velocity is many orders of magnitude higher than typical $E \times B$ drift velocities. Protons on the other hand are strongly affected and special care has to be given to any electric fields in proton experiments. We refer to R. Jiglau's master thesis for an in-depth discussion about the post-acceleration electrode in NoMoS, which is necessary to accelerate protons to detectable energies and which introduces $E \times B$ drift effects, that have to be suppressed [Jig20]. Even small electric fields due to work function differences on the surface of the vacuum chamber can have destructive effects on a proton measurement.

The $R \times B$ Drift

In the presence of a circularly curved magnetic field, an effective drift perpendicular to the curvature radius $\vec{R}$ and the magnetic field $\vec{B}$ can be derived from the general gradient drift and the curvature drift [Sch60, Leh64, Jac99, DKMS05]

$$\vec{v}_{R\times B} = \frac{\gamma m v^2 \cos(\theta)}{qRB} f(\theta) \frac{\vec{R}\times\vec{B}}{RB} + \frac{\gamma m}{qB^2}\left(\dot{\vec{v}}_{R\times B}\times\vec{B}\right) \tag{2.27}$$

In the first term, γ is the relativistic factor, R and B are the norms of the respective vector quantities and $f(\theta)$ is a θ-dependent factor, that will be discussed in more detail later. This is the first order contribution to this drift while the second term leads to higher order contributions, where $\dot{\vec{v}}_{R\times B}$ is the time-derivative of the drift velocity, leading to an iterative equation. The second order term is

$$\vec{v}^{\,\mathrm{2nd}}_{R\times B} = \frac{\gamma m}{qB^2}\left(\dot{\vec{v}}^{\,\mathrm{1st}}_{R\times B}\times\vec{B}\right). \tag{2.28}$$

The θ dependent factor f comes from a reformulation of the velocity components appearing in the original formulas and equals to the following expression

$$f(\theta) = \frac{1}{2}\left(\cos\theta + \frac{1}{\cos\theta}\right) \tag{2.29}$$

It will be discussed extensively in Subsec. 3.1.1 due to its importance in the NoMoS experiment.

Omitting the higher order terms, the drift velocity can be integrated over time to obtain a first order drift distance [DKMS05]. This requires certain assumptions about the form of the curvature vector and the magnetic field. Assuming, that the curved B-field is circular with the time t (at $t = T$, the arc has finished the curvature angle α),

$$\vec{R} = \begin{pmatrix} 0 \\ \cos t\alpha/T \\ \sin t\alpha/T \end{pmatrix} R,\ \vec{B} = \begin{pmatrix} 0 \\ -\sin t\alpha/T \\ \cos t\alpha/T \end{pmatrix} B. \tag{2.30}$$

Building the cross product ($\left(\vec{R}\times\vec{B}\right)_x = RB$, $\left(\vec{R}\times\vec{B}\right)_{y,z} = 0$) and assuming all other quantities constant, integration over time is trivial (from 0 to the time period T) and we end up with only a non-zero contribution in the x-coordinate:

$$D^{\mathrm{1st}}_x = \frac{pv_\parallel T}{qRB} f(\theta),\ D^{\mathrm{1st}}_{y,z} = 0 \tag{2.31}$$

Using the curvature angle $\alpha = v_\parallel T/R$, this formula further simplifies into

$$D^{\mathrm{1st}}_x = \frac{p\alpha}{qB} f(\theta) \tag{2.32}$$

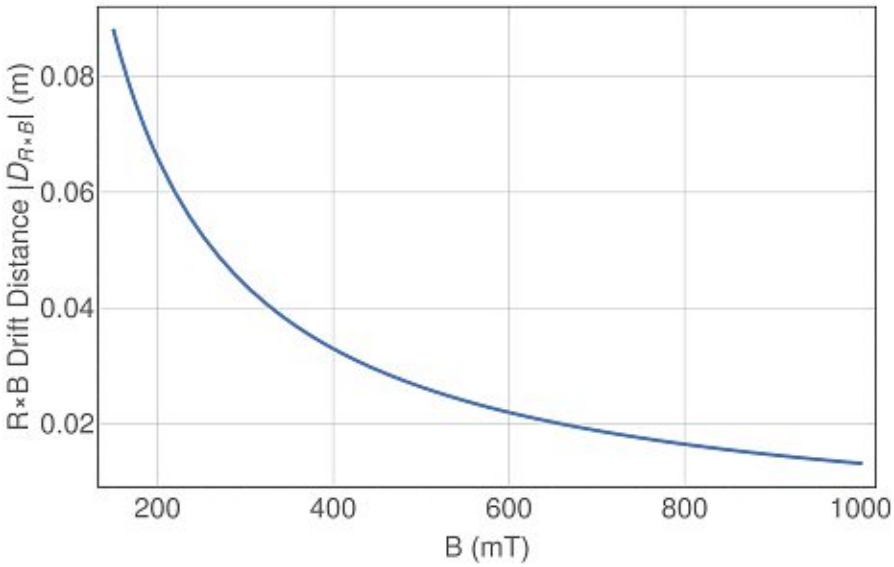

Figure 2.4.: The absolute drift distance of an electron with $p = p_{\max}$, $\theta = 45°$ and $\alpha = 180°$ dependent on the magnetic field B - according to Equ. 2.32.

Figure 2.4 shows the magnetic field dependence of the drift with a drift distance up to 9 centimeter for the maximum electron momentum in the neutron decay ($p_{\max} \approx 1187.28$ keV/c), a pitch angle θ of 45° and a curvature angle α of 180° (drift in negative x-direction - absolute value shown). Note, that the drift distance depends on the charge q, indicating that particles with opposite charge drift in opposite directions (e.g. the electrons and protons from neutron decay). This means that the two particle types are spatially separated, enabling a simultaneous measurement.

For some more developed forms of $\vec{R}(t)$ and $\vec{B}(t)$, analytic corrections can be found to describe more realistic behaviours. Also, higher order terms could be considered, although the second order term is already suppressed to a contribution on the 10^{-4} level.

2.3. Algorithms used for Simulations

The investigation of the NoMoS experiment requires accurate simulations of the electromagnetic fields as well as particle tracking. We use multiple approaches for simulating the electromagnetic fields, but all of them require some kind of

segmentation. This segmentation either happens in the full volume of interest, or only in the domains of field sources (surfaces of electrodes or current carrying volumes for the electric potential and magnetic field respectively). The result of these simulations are then fed into a particle tracking simulation using a Runge Kutta differential equation solver realized in C++.

2.3.1. Electric Field

The most important element in NoMoS that requires electric field investigations, is the electrode system used for the post-acceleration of protons (see [Jig20] for extensive discussion). As the post-acceleration electrode system is not part of this thesis, no major electric field simulations were required. All basic simulations were done with COMSOL - a finite element method program, that can inter alia be used for electric field simulations [COM].

2.3.2. Magnetic Field

The main focus of our studies is the magnetic field investigation of NoMoS. The primary part of the simulations was done with a C++ software called *magfield3* (courtesy of Ferenc Glueck [Glü11, Glü12]). This software segments the current carrying domains in a system (coils) and then sums all contributions at an arbitrary point in space using Biot-savart's law [Jac99]. Assuming enough segmentation of the source domains, this method is very fast and accurate in comparison to finite element methods.

magfield3 requires input data to define the coils in the system. Figure 2.5 shows a schematic view of a general circular magnetic coil with its defining parameters. It illustrates the basic parameters that define a coil.

In general, we define the coil size with the individual winding numbers shown in Equs. 2.33 and 2.34.

$$w = ls + (l-1)d_r \tag{2.33}$$

$$t = bs + (b-1)d_r \tag{2.34}$$

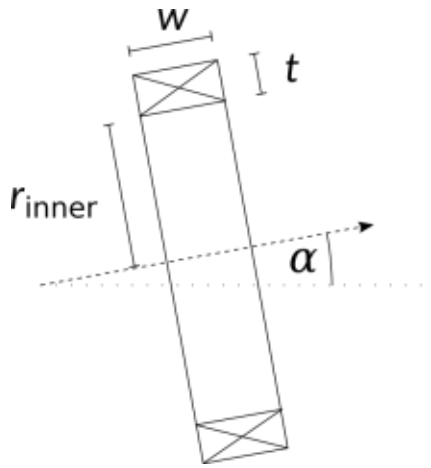

(a) A general circular coil with inner radius r_{inner}, width w, thickness t and a tilting angle α.

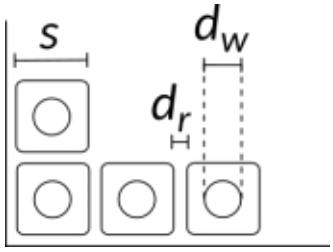

(b) The cross section of a general coil with normal conducting windings with an inner tube for water cooling. The sidelength of the conductor is s, the gap between conductors is d_r and the watertube diameter is d_w. The conductor might have an edge radius r_{e} (not indicated in the picture).

Figure 2.5.: Explanation about the general geometric properties of a circular coil in this work.

with the conductor side length s (in general, cross section could also be rectengular), the number of windings in width w and thickness t: l and b, respectively, as well as the insulation thickness d_r. Also, there is a clear relation between inner and outer coil radius

$$r_{\text{outer}} = r_{\text{inner}} + t \tag{2.35}$$

Magnetic Shielding Materials

In case magnetic materials are investigated ($\mu > 1$), *magfield3* is brought to its limits. For this special case, we again make use of COMSOL, which uses a relaxation method to solve the magnetic field when magnetic materials are in the system.

2.3.3. Particle Tracking

A crucial part of our analysis necessitates simulated particle tracks through our system. This is achieved in general using numerical differential equation solvers. The differential equation at hand is the sum of forces

$$\vec{F} = m\vec{a} = \vec{F}_L \tag{2.36}$$

using the Lorentz force in Equ. 2.13. Another courtesy of Ferenc Glück is the provision of a software for particle tracking (Kassiopeia [F+17], used for the KATRIN experiment [Glü13]). The specialty of this is the inclusion of *magfield3*. This means, that at any exact particle point, the magnetic field can accurately be calculated on the fly instead of relying on interpolation of a magnetic field map. This software is used for every particle tracking investigation in this work, including Monte Carlo simulations.

2.3.4. Numerical Integration

The methods of numerical integration are a vast field of numerical science, deserving of an extensive discussion. Unfortunately, this exceeds the scope of this work drastically, which is why we only have short mentions of the used methods.

The framework of our choice is the *Mathematica* software [Wol]. It provides many

powerful tools for different mathematical operations, including numerical integration. It offers a plethora of numerical integration rules and strategies. The former defines a rule of sample points and weights of the integrand while the latter defines how the numerical error is reduced and optimized. As we are working with higher dimensional integrations (d = 6), the choice is either a conventional multidimensional rule or a Monte Carlo approach. Due to the fact, that we have useful information about the integrand, we chose the so-called *Multidimensional-Rule* [KU98, GM83] over the MonteCarlo rule, overall giving better performance. Concerning the integration strategy, we chose the *GlobalAdaptive* strategy, which subdivides the integrand only in the subregion with the biggest error estimate.

3. The NoMoS Experiment

This chapter will extensively discuss the NoMoS experiment. First, the measurement principle is explained, showing the utilization of the $R \times B$ drift in Sec. 3.1. After that, the purposes and intricacies of the respective areas of the experiment are discussed in Sec. 3.2. Then, in Sec. 3.3, the magnetic field design of the experiment is introduced. Without delving too far into the technical details, the detection principle is shown in Sec. 3.4 (see in progress PhD thesis of W. Khalid [Kha21]). Subsequently, we discuss important design considerations for NoMoS in Sec. 3.5. Next, we introduce the idea of the so-called transfer function, which is capable of semi-analytically describing particles moving through the system and being affected by the systematic effects, resulting in a spatial particle distribution at the detector (see Sec. 3.6). Last but not least, we list the systematic effects of NoMoS in Sec. 3.7.

3.1. Measurement Principle

NoMoS is a $R \times B$ spectrometer [Lob98, WKA13, M$^+$19], named after the $R \times B$ drift (see Subsec. 2.2.1), used for attaining spectral information of the investigated particles. As shown in Equ. 2.32, particles with momentum p will drift a specific distance perpendicular to the curvature radius $\vec{R}$ and the B-field. If this drift distance can be resolved on a detector, information about the momentum can be obtained. The $R \times B$ drift in the context of our spectrometer will be further discussed in the following.

3.1.1. Comparison to Conventional Magnetic Spectroscopy

As can be seen from the drift formula (Equ. 2.32), the drift distance is also dependent on the local pitch angle θ. Due to this, the pitch angle has to be known to a certain degree for the proper determination of the drift. This is also

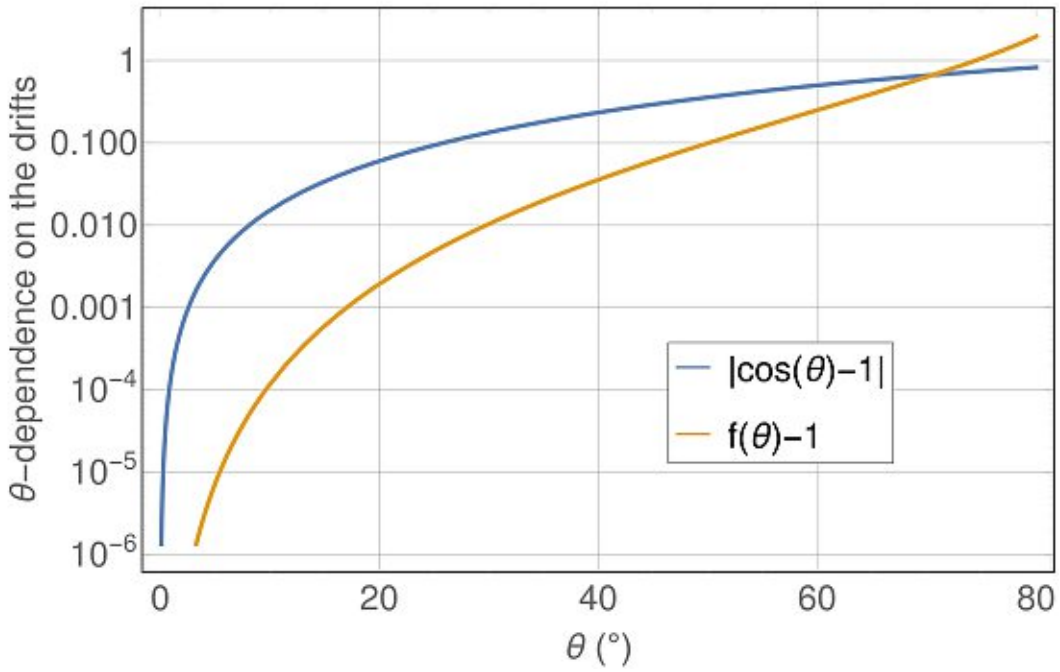

Figure 3.1.: Comparison of the θ dependent factors in the measurement principles of the conventional magnetic spectrometer and the $R \times B$ spectrometer.

the case for a conventional momentrum spectrometer, using a B-field gradient to force charged particles on a circular motion, proportional to their gyration radius. There, the pitch angle determines the perpendicular momentum component, which contributes to the radius. One can compare the respective dependency on the pitch angle to check the sensitivity on the drift, which is illustrated in Fig. 3.1. It shows that for pitch angles up to 30°, the dependency's deviation from one is at least one order of magnitude less for a $R \times B$ spectrometer than for a conventional magnetic one.

3.1.2. Application for other Beta Decays

We have shown in Fig. 2.4 that the total drift distance depends strongly on the magnetic field. To investigate the scope of application of a $R \times B$ spectrometer, we check the approximate total beam size dependent on the B-field and the maximum momentum $p_{\max}$ and pitch angle $\theta_{\max}$ of a general particle to be measured. Equ.

Table 3.1.: A selection of isotopes with their maximum momentum $p_{\max}$ [Nat20] and the minimum B-field $B_{\min}$ required to map it on a 10 centimeter detector in a $R \times B$ spectrometer.

Isotope	$p_{\max}$ (keV/c)	$B_{\min}$ (T)
^{109}Cd	286.8	0.0506
^{139}Ce	390.3	0.0688
^{45}Ca	571.7	0.1008
^{133}Xe	688.5	0.1214
^{113}Sn	716.4	0.1264
^{207}Bi1	875.8	0.1545
^{137}Cs	1020.2	0.1799
^{127}Te	1100.1	0.194
n β^-	1187.3	0.2094
^{207}Bi2	1416.7	0.2499
^{26}Al	1604.6	0.283
^{129}Te2	1918.1	0.3383
^{129}Te	2056.5	0.3627
^{68}Ga	2355.2	0.4154
^{114}In	2446.2	0.4315
^{107}In	2660.4	0.4692
^{38}K	3194.4	0.5634
^{30}P	3685.7	0.6501
^{18}Ne	3901.7	0.6882
^{6}He	3986.2	0.7031
^{14}O	4603.7	0.812
^{12}B	13870.6	2.4465
^{12}N	17841.7	3.1469

3.1 shows this quantity, additionally considering the additional reach due to the particle gyrating and the opening of an aperture x_{AA} (this will be further explained in the following section) defining the possible starting position of the particle.

$$x_{\max} = D_{R\times B}\left(p_{\max}, \theta_{\max}, B_{\min}\right) + 2r_G(p_{\max}, \theta_{\max}, B_{\min}) + x_{\mathrm{AA}} \tag{3.1}$$

Solving this equation for the required minimum B-field $B_{\min}$, assuming a detector size of 10 centimeters, a curvature angle $\alpha = 180°$ and $\theta_{\max} = 45°$, different decay spectra according to their maximum momentum $p_{\max}$ can be compared. This is listed in Table 3.1 for a selection of isotopes.

This extensive list of isotopes opens up interesting options for additional measurements in beta decay, if the required magnetic field can be reached.

3.2. Features

The most essential part of the NoMoS experiment is a toroidal coil structure, in which the curved magnetic field is created, the so called $R \times B$ region. However, this is not sufficient to conduct an experiment in neutron beta decay. There is a multitude of additional features required for conducting the experiment. First, free neutrons need to be guided towards a decay volume, from which the charged decay products are gathered. Then, commonly the angular phase space is restricted with a magnetic filter to suppress certain systematic effects in the system. After that, a well defined beam is defined by an aperture with a precise opening for the charged particle beam. All of this is grouped into the beam preparation area. Subsequently, the particles reach the $R \times B$ region, experiencing the drift. Finally, the particles reach the detection region where the beam is detected with a spatially resolving detector - the $R \times B$ drift detector. This procedure is illustrated in a 3D model of NoMoS in Fig. 3.2. The single regions are more thoroughly discussed in the following.

3.2.1. Decay Volume

In the first step of the NoMoS experiment, a neutron beam from a neutron source has to be guided into a dedicated zone, from which the charged decay products of the neutron decay can be magnetically gathered. This is the so-called decay volume. A magnetic field guides the particles out of the neutron beam, while the remains of the latter are dumped into a beam stop. In principle, the decay volume can be external but NoMoS is designed with the capability of gathering the particles on its own.

3.2.2. Filter

A magnetic filter uses the magnetic mirror effect to raise pitch angles of charged particles in an increasing magnetic field until they are reflected. This effect has a critical angle dependent on the B-field ratios between to points, according to Equ.

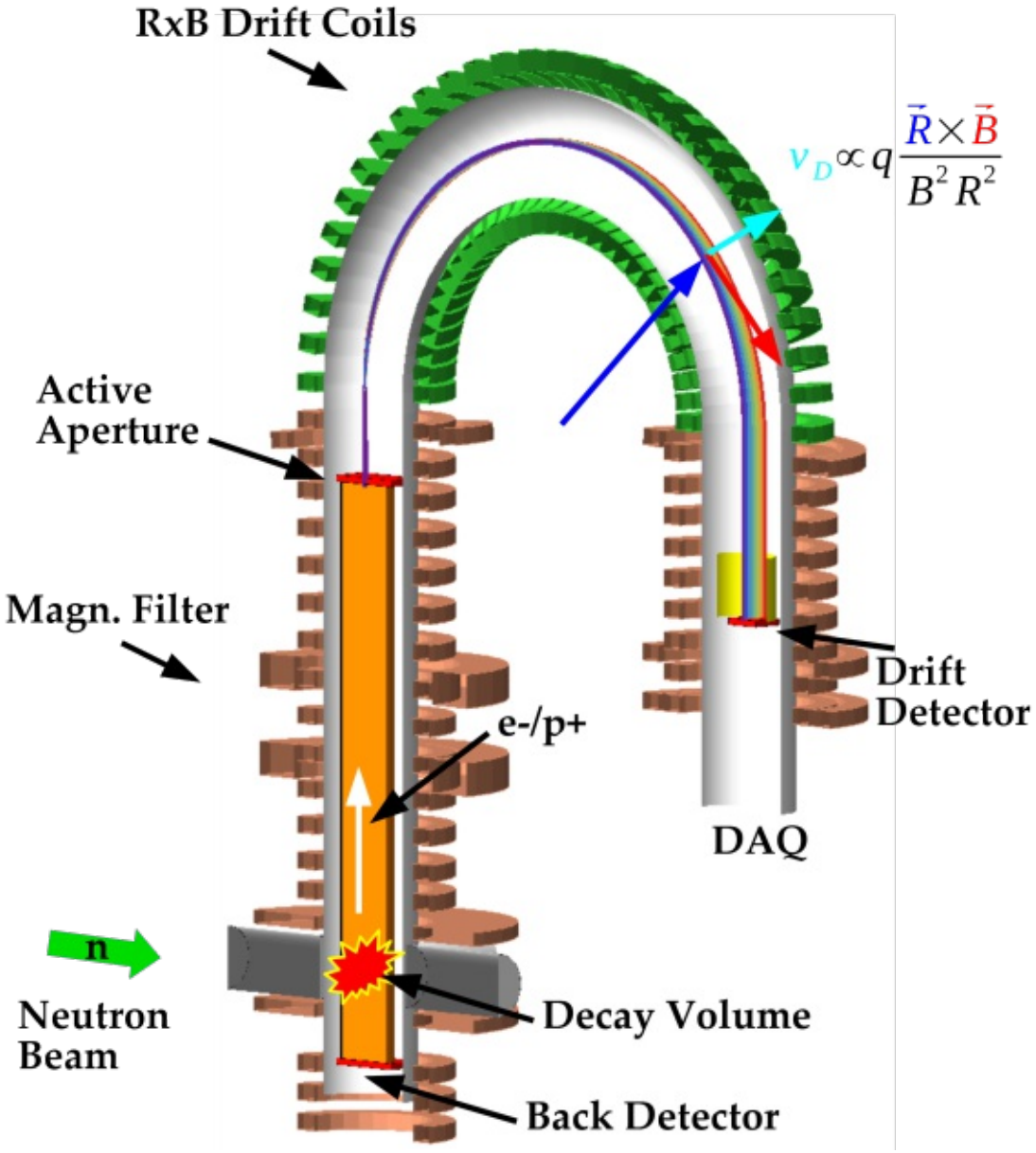

Figure 3.2.: A schematic view of the NoMoS experiment. The $R \times B$ coils are colored green whereas all other coils are copper colored. Neutrons enter the decay volume where the decay products are gathered down- and upwards. There is a back detector installed for the monitoring of the downwards headed particles. The upwards particles reach a magnetic filter, filtering pitch angles over a critical angle. Then, the particle beam is cut into a well-defined cross section by an active aperture (active means that some surfaces have detectors installed). Afterwards, the particle beam enters the $R \times B$ drift region where they experience the curved magnetic field and therefore the drift (indicated with rainbow colors). In the detection region, there is a spatial resolving detector installed.

2.21. For a ratio of two, the critical angle is 45°. All incident angles higher than this will be reflected at the magnetic field maximum (in a plane perpendicular to the beam). This is used to restrict the pitch angles entering the rest of the experiment for systematic effect suppression. In principle, this feature can be external, even though NoMoS has this feature installed. Alternatively, a similar effect can be achieved by decreasing the magnetic field, tilting the pitch angle forwards, changing the angle according to Equ. 2.20.

3.2.3. Aperture

For a well defined particle beam entering the spectrometer, some sort of shaping of the beam is required. This is most easily done using a collimator or aperture. It restricts particle transmission in a geometric region. This introduces an edge effect which in general is energy and angle dependent. Also, the transmission behaviour is going to depend on the local magnetic field, and therefore its homogeneity.

3.2.4. $R \times B$ Drift Region

After the filter and aperture, the particles enter the $R \times B$ drift region, where the toroidally arranged coils are located. These coils create a curved magnetic field and are the basis for the $R \times B$ drift to happen. The amount of curvature is given by the curvature angle α. In Fig. 3.2, the geometrical curvature angle is 180° (the real curvature angle α can be slightly different - see Subsec. 5.2.1). An intricacy of these coils is the natural formation of a radial magnetic field gradient $\nabla_r B$. This is due to the fact that on the inner side of the curvature, the coils (and therefore the electrical current) are denser compared to the outer side. This behaviour can not be suppressed, but only slightly modulated by coil/geometry parameters (see Subsec. 3.5.2).

3.2.5. Detection Region

The detection region is the last region in the path of the particles and provides a homogeneous magnetic field for the particles hitting the $R \times B$ drift detector. The detector itself will be discussed in more detail in the following section.

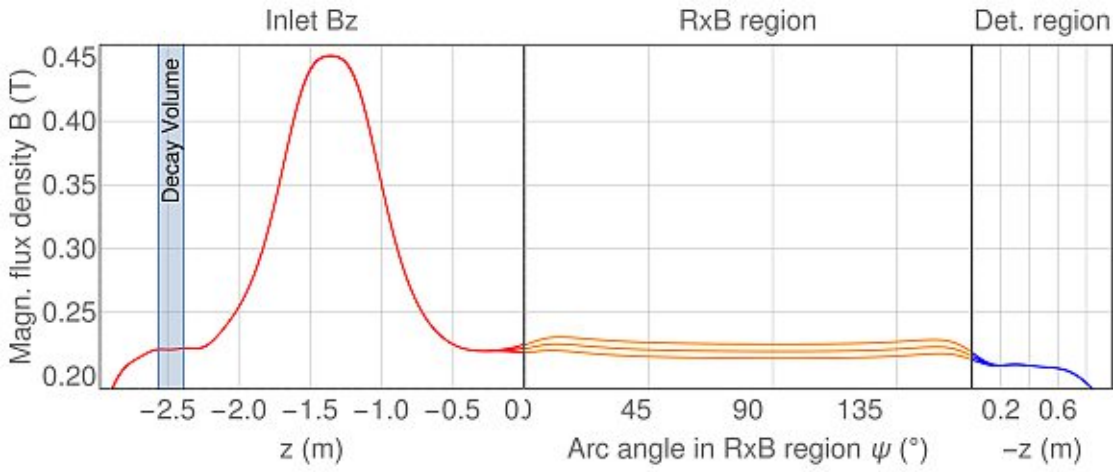

Figure 3.3.: The absolute magnetic field strength B through NoMoS along geometrical lines. The figure is separated into the beam preparation area, the $R \times B$ and the detection region.

3.3. Magnetic Field in NoMoS

A first glimpse at the magnetic design in NoMoS is shown in Fig. 3.3, illustrating the magnetic field norm through the system along geometrical lines (with different starting positions perpendicular to the B-field flux). The presented example is a normal conducting variant used as a standalone experiment (more about this in Sec. 3.5).

In the decay volume, a flat homogeneous field strength is observed, which then increases towards the magnetic filter with approximately double the strength. Afterwards it goes down again for a short homogeneous region at the aperture ($z = -0.3$ m). Just before the $R \times B$ region, the previously seemingly single line separates into multiple ones, that illustrate the $R \times B$ region's radial magnetic field gradient for different starting positions in y. Within in the $R \times B$ region, the field along the geometrical lines is somewhat homogeneous with inhomogeneities towards the borders of the region. Finally, in the detection region, the magnetic field drops slightly before a relatively homogeneous field at the detector (e.g. at $z = -0.45$ m).

3.4. Detection System

The NoMoS detection system consists of the main detector, responsible for resolving the drift of the electrons and/or protons and a secondary system of detectors, used to investigate systematic effects and to monitor the system.

3.4.1. $R \times B$ Drift Detector

We have mentioned before that a spatial resolving detector (in at least one dimension) is required for an $R \times B$ spectrometer. Additionally, two different charged particle types (electrons and protons - which in principle can be detected simultaneously) with very different energies can be observed from the decay. Therefore, a complex detection system needs to be designed. As the protons have very low energies ($T_{\mathrm{p,max}} \approx 751$ eV), post-acceleration is required to make them detectable (see master's thesis of R. Jiglau [Jig20]). A new detector principle, called pLGAD, is currently being developed for optimal detection efficiency (see in progress PhD thesis [Kha21] as well as prospective papers by W. Khalid).

3.4.2. Secondary Detection System

Besides the main detector, there are multiple secondary detection systems planned, which will be used for monitoring and better understanding of several systematic effects. The aperture has two detectors integrated for different purposes.

- **Scattering off from inner aperture faces**: The aperture in NoMoS is a clearly defined opening with a specific thickness. This finite thickness leads to inner faces of the opening, through which particles can scatter off and change their energy, pitch angle and position in the magnetic flux tube while entering the $R \times B$ drift region. To better understand this effect, the inner faces are active to detect deposited energy of the particles.

- **Backscattering from the $R \times B$ drift detector towards aperture**: There is a certain probability for particles to be backscattered from the main detector. If this happens, particles may re-enter the $R \times B$ drift region, drift again in the same direction and then either hit the aperture from the backside or go through the opening again. To investigate backscattering, the aperture's backside is made active to detect those particles.

Besides the aperture, there is yet another detection system, whose design and purpose depend on the measurement site (see Subsec. 3.5.3). The distinction is made by the decay volume being internal or external.

- **Internal decay volume**: In case NoMoS is used as a standalone experiment using the internal decay volume, the second hemisphere of the decay products' emission is monitored for absolute flux and systematic estimations. Additionally, the reflected particles from the filter are detected. This is done at the upstream end of the beam preparation area. $\approx 93\%$ of the decay flux is expected to hit this detector.

- **External decay volume**: If an external decay volume is used, the flux entering NoMoS is monitored. This is done by a detector, installed in the NoMoS decay volume, that measures the peripheral flux of the beam cross section.

3.5. Design Considerations

In such a complex experiment as NoMoS, there are a multitude of internal and external parameters that can be changed. For a specific configuration, not only the magnetic behaviour has to be considered, but also practical and engineering aspects. In this section, we discuss different conductor technologies, geometric coil parameters, possible measurement sites and corresponding expected statistics and overall cost of NoMoS. At the end, we present the featured configurations in this work.

3.5.1. Conductor Technology

Normal-conducting (NC) copper coils are a very mature technology that can fulfill a variety of needs, but have some restrictions and disadvantages. There is a limit in the coil operation current and therefore a limit in the magnetic field strength. Furthermore, the power consumption increases quadratically with the current. The superconductor (SC) technology provides an interesting alternative (note, that we will focus on the low temperature superconductor material NbTi). The major advantages of the single technologies are listed in Tab 3.2. One major point not included in the table are the systematic effects that may be influenced by the chosen conductor technology (if a different base magnetic field $B_{R\times B}$ is used).

Table 3.2.: The advantages of normalconducting technology and superconducting, respectively. Some are general, others specific to NoMoS.

	Normalconducting (Cu)	**Superconducting (NbTi)**
General	Less construction cost more adjustable (modular)	Less operation cost Flexible (higher) B-fields
NoMoS	Larger drift distance (possibly) higher momentum resolution (potentially) less backscattering	Less $E \times B$ drift (protons) smaller gyration radii Better B homogeneity

This will be treated in Ch. 5.

Even though the construction cost of a NC system is cheaper, in the long run, a SC system may be cheaper due to the smaller operation cost. The modification and adaptation possibilities in a NC system are a clear advantage over SC, as for the latter, changes after manufacturing are expensive and challenging. One of the biggest advantages of a SC NoMoS is the more flexible magnetic field strength. This is attractive to investigate systematic effects connected to the magnetic field, to modify the drift distance overall and to reduce $E \times B$ drift effects for protons ($\propto 1/B$). Furthermore, we have shown in Subsec. 3.1.2 that there is an interesting range of isotopes, that can better be accessed with a SC $R \times B$ spectrometer. Also, the achievable B-field homogeneity is better. Finally, another possible advantage for a NC system would be the higher drift resolution because the beam is bigger for smaller fields.

Conductor Geometry

Of course, there are different conductors available on the market for both technologies. For the rough coil sizes that we want to use, there are some candidates that have been discussed with external companies. In Tab. 3.3 we show the conductor parameters for a default type each that are investigated for NoMoS.

3.5.2. $R \times B$ Coil Geometry

One of the most characteristic parameters in the overall NoMoS geometry is the central curvature radius R_0. Nevertheless, its value is not chosen, but calculated

Table 3.3.: Default parameters of conductors for the two technologies. These were discussed with coil manufacturers.

	Parameter	**Value**
NC (Cu)	Side length s	8 mm*
	watertube diameter d_w	4 mm*
	edge radius r_e	1 mm
	Insulation resin thickness d_r	1 mm
	Maximum copper current density $i_{\max}$	$\sim$10 A/mm^2
	Maximum engineering current density† $i'_{\max}$	5 A/mm^2
SC (NbTi)	Cross section $l \times b$	1.19 × 0.64 mm
	Insulation thickness d_r	0.12 mm
	Critical current I_c at 3 Tesla	$\geq$ 495 A

* If higher total currents in the coil cross section are required, there are bigger conductors with bigger watertube diameters.

† The current density over the total current carrying cross section of a coil (rough value for managable water cooling).

with Equ. 3.2 by setting other parameters of the $R \times B$ region. This property is illustrated in Fig. 3.4, where other related parameters are also indicated.

As a formula, R_0 is given by

$$R_0 = r_{\text{outer}} + \left(\frac{w}{2} + d_{\text{gap}}\right) \cot \frac{\alpha_{\text{geo}}}{2(N-1)} \tag{3.2}$$

R_0 depends on the outer coil radius r_{outer}, the coil width w, the desired approximate safety gap between two consecutive coils d_{gap} as well as the geometric curvature angle α_{geo} and the total number of $R \times B$ coils N. We calculate R_0 as a passive parameter, as we want to fine-tune the single coil parameters and the integer number of coils. $\Delta\alpha$, indicated in Fig. 3.4, is given by

$$\Delta\alpha = \frac{\alpha_{\text{geo}}}{N-1} \tag{3.3}$$

Dependence of Radial Magnetic Field Gradient on Curvature Radius

As mentioned in Subsec. 3.2.4, there is a natural radial magnetic field gradient in the $R \times B$ region. Investigations into the coil geometry using the software mentioned in Subsec. 2.3.2, have shown that this quantity can be influenced by

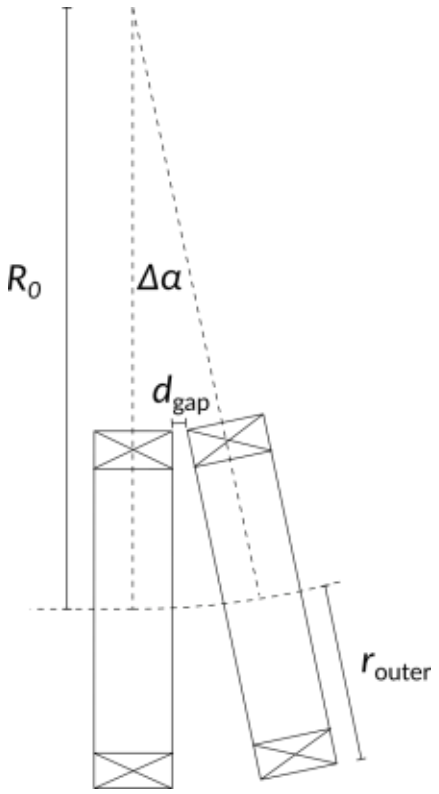

Figure 3.4: Two consecutive circular coils in the $R \times B$ region, beginning with the very first coil after the beam preparation area. The outer coil radius r_{outer} is given by Equ. 2.35, the angular step between the two coils is $\Delta\alpha$, the central curvature radius is R_0 and the safety gap between the coils is d_{gap}.

variation of the curvature radius. Figure 3.5 shows different radial gradient values (evaluated within a default beam size of 10 cm in the radial direction around the central curvature radius at $\alpha_{\text{geo}} = 90°$ of a $\alpha_{\text{geo}} = 180°$ $R \times B$ region). The variation of R_0 is accomplished by varying the total number of $R \times B$ coils N. All other coil parameters stay the same. Trends are indicated with a linear and an exponential decrease fit.

In general, the radial gradient can be reduced but not eliminated by making a bigger curvature radius. Furthermore, increasing the curvature radius is directly connected to higher construction cost and experiment size (both in general have tight limits).

Dependence of Radial Magnetic Field Gradient on Inner Coil Radius

One might hypothesize that increasing the inner coil radius r_{inner} of the $R \times B$ coils leads to a decrease of the radial gradient (due to the fact that for a general coil, homogeneity increases with the inner radius of the coil - while the absolute field strength decreases). The investigation of this shows a different result. Figure

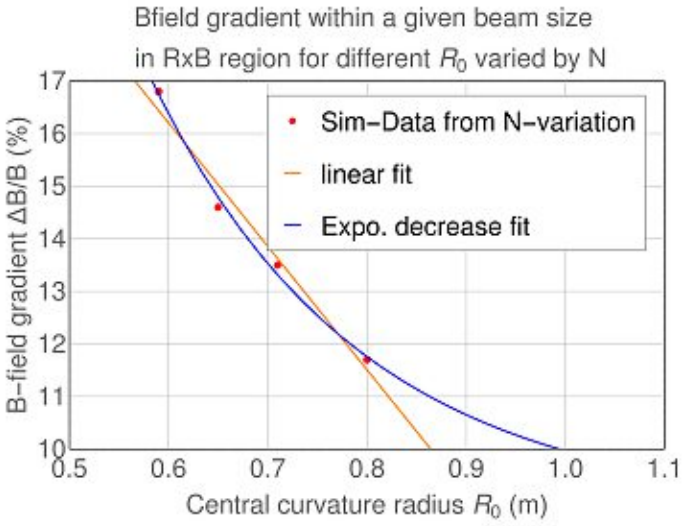

Figure 3.5.: The radial magnetic field gradient dependent on the central curvature radius R_0. The gradient is evaluated within a beam size of 10 cm around the center, at $\alpha_{\text{geo}} = 90°$ for a $R \times B$ region of $\alpha_{\text{geo}} = 180°$. The trend is highlighted by fitted linear and exponential decrease functions.

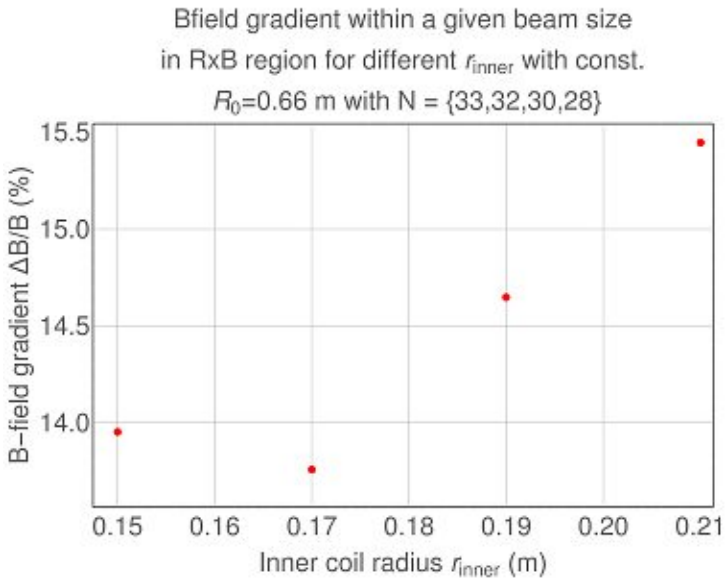

Figure 3.6.: The radial magnetic field gradient dependent on the inner coil radius r_{inner}. The gradient is evaluated within a beam size of 10 cm around the center, at $\alpha_{\text{geo}} = 90°$ for a $R \times B$ region of $\alpha_{\text{geo}} = 180°$. The central curvature radius R_0 is held constant by adjusting the number of coils N accordingly.

3.6 shows the gradient dependent on the inner coil radius r_{inner}, while a constant curvature radius is garanteed by varying N accordingly (respective value of N given in title of the figure).

This result shows that there is an optimum of the magnetic field gradient. This optimum is not global for the system but dependent on other parameters. Smaller inner radii restrict the possible vacuum tube diameter whereas bigger inner diameters lead to higher construction cost and power consumption.

Geometric Curvature Angle α_{geo}

For our investigations, we mainly focused on $\alpha_{\text{geo}} = 180°$ and 90°. The lower this angle, the less drift the particles experience (see linear dependence of α on the $R \times B$ drift in Equ. 2.32). Nonetheless, a quarter toroid segment has engineering and assembly advantages over half a toroid. Furthermore, the sensitivity of systematic parameters can be significantly changed, due to the fact that α strongly changes

Table 3.4.: Fundamental properties of the PF1B beam site at the ILL.

Property	**Value**
Neutron beam cross section $b \times l$	6×20 cm^2 (unpolarized, reducible)
Mean wavelength	$4 - 4.5$ Å
Equivalent flux density Φ_n	1.8×10^{10} n/cm^2/s
Neutron beam height from ground	1.4 m
Available experiment volume*	$2.4 \times 4.5 \times 5$ m^3
Maximum electrical power	330 kW
Maximum cooling power	330 kW

* The total available volume is longer. The given values are for the magnet system.

the form of the drift distance spectrum (see Subsec. 5.4.2). A proposed mechanical design by the company *Danfysik* shows a certain modularity, allowing for only 90° of $R \times B$ coils to be constructed, but enabling a 90° extension further down the line (more details in the following subsections). See [M$^+$20] for discussions on a 90 degree set-up.

3.5.3. Measurement Sites and Statistics

NoMoS requires a high flux neutron source to investigate neutron beta decay. In the following, we present a proposed list of feasible measurement sites, showing their neutron beam parameters and other boundary conditions. Furthermore, for the two existing beam sites, statistical estimates are given.

PF1B at Institute Laue-Langevin in Grenoble

The *Institute Laue-Langevin* (ILL) is a research facility with a nuclear reactor located in Grenoble, France. It has the worlds highest neutron flux as of today. There is a dedicated beam site for fundamental physics called PF1B [A$^+$06]. Its fundamental properties are shown in Tab. 3.4.

At the ILL, NoMoS is used as a standalone experiment as it has to provide its own decay volume. The neutron beam enters the experimental site from the side, requiring NoMoS to be oriented as shown in Fig. 3.2. The estimated detection rate of electrons and protons at the $R \times B$ drift detector is roughly 1kHz, respectively. This is calculated with the following steps:

1. Take the neutron beam equivalent flux Φ_n times the
2. neutron beam cross section $A_\mathrm{n} = l \times b = 6 \times 20\ \mathrm{cm}^2$ to retrieve the neutron intensity.
3. Construct the in-beam decay rate by multiplying with decay volume length L and dividing by the neutron velocity times the mean lifetime $v_\mathrm{n}\tau_\mathrm{n}$.
4. Consider that only one hemisphere enters the spectrometer (factor 1/2) and that the filter transmits only the fraction $1 - \sqrt{(r_\mathrm{F}-1)/r_\mathrm{F}}$ (with the filter magnetic field ratio $r_\mathrm{F} = B_\mathrm{F}/B_\mathrm{DV}$).
5. Assuming the aperture magnetic field ratio $r_\mathrm{A} = 1$, the aperture transmits the fraction $x_\mathrm{AA}y_\mathrm{AA}/(Lb)$ (with the aperture opening width and length x_AA and y_AA and the neutron beam cross section relative to the magnetic field with width b and length L).

This leads to the following formula and approximation for the detector signal rate n

$$n = \Phi_\mathrm{n} A_\mathrm{n} \frac{L}{v_\mathrm{n}\tau_\mathrm{n}} \frac{1}{2} \left(1 - \sqrt{\frac{r_\mathrm{F}-1}{r_\mathrm{F}}}\right) \frac{x_\mathrm{AA}y_\mathrm{AA}}{Lb} \approx 1060\,\mathrm{Hz} \tag{3.4}$$

The calculated approximation uses the following parameter values: $L = 0.1$ m, $v_\mathrm{n} = 2200$ m/s, $\tau_\mathrm{n} = 880$ s, $r_\mathrm{F} = 2$, $x_\mathrm{AA} = 1$ cm and $y_\mathrm{AA} = 3.5$ cm additionally to the aforementioned parameters' values.

PERC at FRM2 in Munich

The *Forschungs-Neutronenquelle Heinz Maier-Leibnitz* (FRM2) is a research reactor in Munich, Germany. *MEPHISTO*, a dedicated beam line for cold neutron physics, is currently under construction. Connected to this will be a super conducting magnet system, providing a highly optimized decay volume and filter for neutron decay experiments, called PERC [D$^+$08, K$^+$12, W$^+$19]. The basic parameters of this system are given in Tab. 3.5.

PERC provides spectrometers with a highly homogeneous and large decay volume with a flexible range of filter settings. At this experimental site, NoMoS is already provided with the decay products, requiring a different orientation, shown in Fig.

Table 3.5.: Fundamental properties of the instruments MEPHISTO and PERC at the FRM2.

	Parameter	Value
MEPHISTO		
	Neutron beam cross section	5×5 cm^2 (unpol.)
	Equivalent neutron flux	$\approx 1 \times 10^{10}$ n/cm^2/s
PERC		
	Decay volume B-field homogeneity	1×10^{-4}
	Decay volume length	8 meters
	Decay products' beam height	≈ 1.17 m
	Available decay volume B-field B_{DV}	0.5 - 1.5 T
	Available filter B-field B_{F} range	3 - 6 T
	Available field ratio r_{F} range	2 - 12

3.7.

Applying the same procedure for the expected statistics at the NoMoS detector as above, we arrive at a count rate of ≈ 1.4 kHz. We used the following values: $\Phi_{\mathrm{n}} = 1 \times 10^{10}$ n/s/cm^2, $A_{\mathrm{n}} = 25$ cm^2, $r_{\mathrm{F}} = 4$, $r_{\mathrm{A}} = 0.147$ (0.22/1.5), and the perpendicular decay product cross section at the aperture is $r_{\mathrm{A}} x_{\mathrm{AA}} y_{\mathrm{AA}}/(lb)$. The result we obtain is

$$n = \Phi_{\mathrm{n}} A_{\mathrm{n}} \frac{L}{v_{\mathrm{n}} \tau_{\mathrm{n}}} \frac{1}{2} \left(1 - \sqrt{\frac{r_{\mathrm{F}} - 1}{r_{\mathrm{F}}}}\right) \frac{r_{\mathrm{A}} x_{\mathrm{AA}} y_{\mathrm{AA}}}{lb} \approx 1420\,\mathrm{Hz} \tag{3.5}$$

European Spallation Source in Lund

The European Spallation Source in Lund [L$^+$11] is a new site for neutron physics experiments currently under construction in Lund, Sweden. There, a fundamental neutron physics beamline could be installed for strongly improved statistics, called ANNI [E. 16]. As the user program only begins with 2023, we only mention this here as long term possibility.

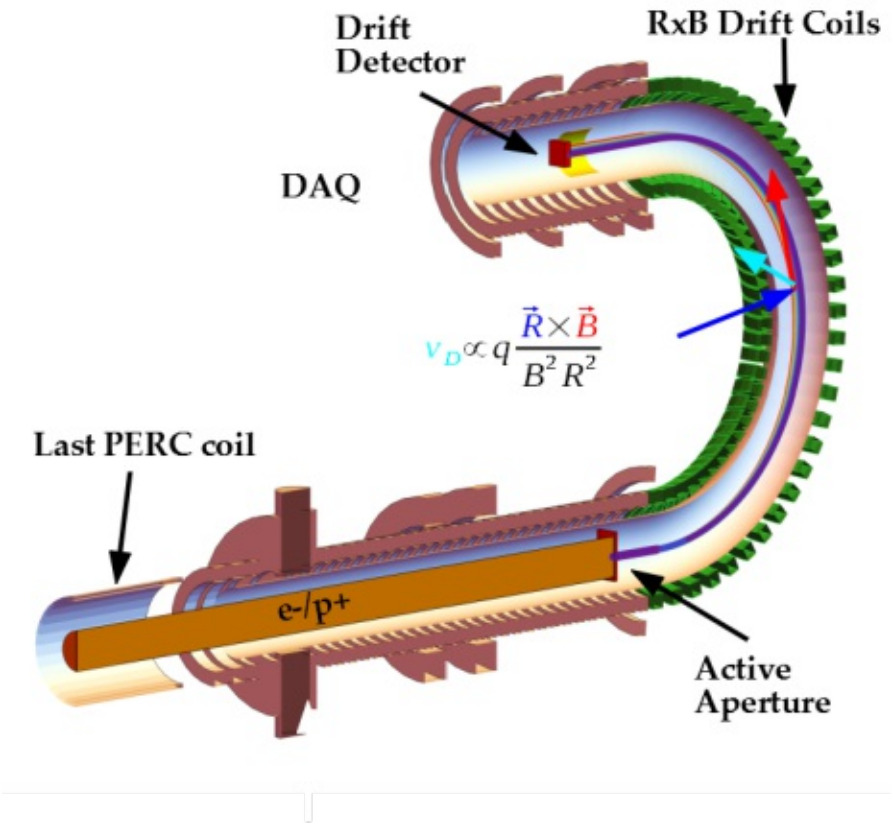

Figure 3.7.: An examplatory configuration of NoMoS at PERC, indicating the different orientation, the decay products already entering NoMoS as a combined beam as well as the last PERC coil.

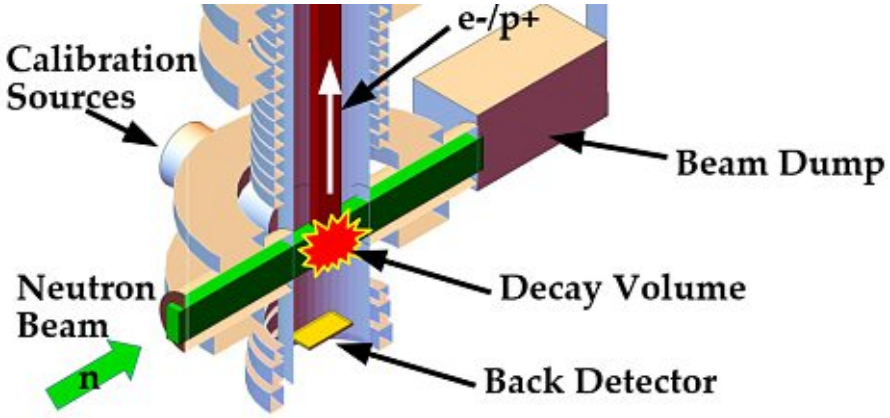

Figure 3.8.: NoMoS cut in half at the decay volume, showing the neutron beam in green, the decay products emitted upwards and downwards and a port for calibration sources.

3.5.4. Overall Cost

The overall cost of an experiment is a significant factor that influences most if not all design choices. Besides the raw coil cost, thoughts have to be given to the realization of the vacuum system, required peripherals as well as engineering considerations. The numbers given are estimates from market investigations as well as commissioned studies.

Vacuum System

To provide enough space for both electron and proton beams (for a simultaneous measurement), a rectangular cross section of 20×10 cm^2 is considered. Furthermore, the proton post-acceleration electrode system demands additional space. Last but not least, the distance of the protons the vacuum walls should be reasonably large to reduce surface work-function effects. This is why the default vacuum tube diameter is chosen to be 350 mm. With this, the vacuum tubing of a $\alpha_{\text{geo}} = 180°$ alone costs approximately 100 k€. The most complex part of the vacuum system is the double cross part for the decay volume, serving multiple purposes, shown in Fig. 3.8. It allows the neutron as well as the decay products' beam to enter. Also, it provides insert options for radioactive calibration sources, pressure gauges etc.

Peripherals

The most important peripherals include but are not limited to: power supplies, cooling solution, vacuum infrastructure (pumps, gates etc.) and monitoring of the aforementioned parts. In the following, we will focus on a normal conducting system, as more engineering investigations have been performed (by the NoMoS group and external companies) in this regard.

A normal conducting NoMoS with a base magnetic field of $B_{\mathrm{R\times B}} = 220$ mT has an electrical power consumption of roughly ≈ 300 kW (of course, there is a lot of handles and design choices influencing this). As there are multiple different currents needed (at high accuracy $\Delta I/I < 10^{-4}$), several smaller power supplies are required. Their price is significant with an estimated total of 300 k€.

In a NC system, cooling works with water being pumped through the conductor, which has an inner water tube. That way, the water can transport the produced heat away. To achieve proper cooling, the input pressure of the water has to be high enough, requiring a suitable pump. To get rid of the heat, the heated water commonly goes through a heat exchanger connected to a secondary water circuit. Such a pumping system costs in the order of 30 k€.

Especially for protons, a high vacuum quality is important to suppress residual gas interactions. As a rule of thumb, the vacuum should be at the level of 10^{-8} mbar. For an electron experiment, this level may not be required. The cost for pumping equipment may easily exceed 50k€.

Engineering Considerations

Considering the weight of the copper in a NC default configuration of NoMoS, special attention has to be given to the support structure. It has to hold the coils as well as the vacuum system firmly in place to provide the basis for an accurate experiment. Furthermore, as discussed in Subsec. 3.5.3, NoMoS is intended to be used at multiple experimental sites, which require different orientations. This means, that NoMoS also needs flexibility in its assembly. A design study by *Danfysik*, a coil company from Denmark, has resulted in a support structure for these difficult demands. The proposed structure is illustrated in Fig. 3.9. The cost of this structure (which is also capable of holding magnetic shielding if required) is estimated at ≈ 100 k€.

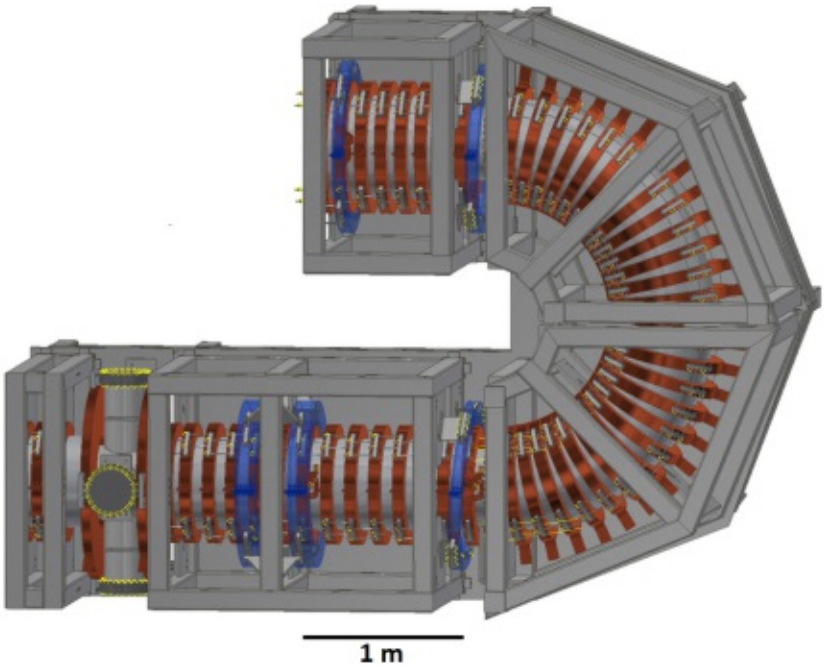

Figure 3.9.: A support structure design by *Danfysik*. It shows the vacuum tubing, the coils and the inner and outer support structure, holding everything together. The structure is separated into modules for more flexible assembly and different orientations.

3.5.5. Featured Configurations

In this work, we present two proposed designs of NoMoS, based on the two different conductor technologies, normal and super conducting. The coil data is presented in App. A. Both use a geometric curvature angle $\alpha_{\text{geo}} = 180°$, maximizing the experienced drift (higher α_{geo} leads to strong engineering obstructions). Furthermore, they have a dedicated decay volume and filter installed, not relying on external beam preparations. The base magnetic field of the NC and SC system are at roughly 220 mT and 1000 mT, respectively.

3.6. The Transfer Principle

The most crucial part of my work surrounds a principle, capable of semi-analytically calculating the expected particle beam at the detector without the need of a fully tracked Monte-Carlo-simulation - the so-called transfer function [WKA13] (note that the idea stems from the referenced paper but the method has since diverged strongly from that paper's approach). This function maps initial particle properties to positions at the detector. It requires input data in form of a momentum and pitch angle distribution and an analytic description of the transport effects through the system. It can further have functions describing systematic effects with a weighting character. All of this is discussed in detail below.

3.6.1. The Transfer Function

The basis of the mapping is the Dirac delta-function $\delta_x\,(x - x_0)$. This function equals to one if and only if the argument equals to zero. A simple transfer function T_x is the following equation

$$T_x(x_0, x_D, ...) = \delta_x\,[x_{\text{D}} - (x_0 + D_{R\times B})] \tag{3.6}$$

with the particle starting point x_0, the $R \times B$ drift $D_{R\times B}$ and the particle position on the detector x_{D}. The transfer function gives a non-zero value only if a particle starting at a specific starting point x_0 and experiencing a $R \times B$ drift equal to a particular position on the detector x_{D}. For any other detector position, drift or starting position, the delta-function returns zero. This means that this case is a one-to-one mapping. In the general case, the argument includes complex transport effects and many more parameters, leading to interdependent distributions of allowed phase spaces in the respective parameters.

3.6.2. Input Functions

The second part of the transfer concept are the input functions. There are multiple input parameters of a respective decay particle, that set the stage for the particle's particular transport through the system. This can include the energy/momentum, incident pitch angle and others. In general, these parameters follow a certain distribution ω_i. Such a distribution can be continuous or not. In our case we consider e.g. the initial momentum distribution of the decay products $\omega_{p^+/e^-}(p)$. This input function is then convoluted with the transfer function to retrieve a drift distance spectrum $G_x\left(x_\mathrm{D}\right)$. In a general form (in one dimension), this can be written as

$$G_x\left(x_\mathrm{D}\right) = \int\int\int \ldots T_x(p_1,\ldots)\omega_1(p_1,\ldots)\omega_2(p_1,\ldots)\ldots dp_i \tag{3.7}$$

This equation shows a multidimensional integration over all convoluting (input) parameters p_i, which sums up all possible contributions to the detector position x_D. The transfer function ensures that only the allowed parameter space, following a specific transport, contributes to the detector position. Furthermore, there can be more than one transfer (more spatial dimenions, e.g. T_y) and input functions (more particle inputs ω_i) with multiple input parameter dependencies.

3.6.3. Systematic Weighting Functions

Last but not least, there can be systematic effects with a weighting character. For example the aperture has a transmission dependent on the particle's position at the aperture. Therefore, this transmission function is multiplied to the integrand to additionally consider this restriction in the parameter space. In general, these functions depend on systematic parameters as well as input parameters. A general formula is given below

$$G_x\left(x_\mathrm{D}\right) = \int\int\int \ldots T_x(p_1,\ldots)\omega_1(p_1,\ldots)\omega_2(p_1,\ldots)\ldots W_1(p_1,\ldots)\ldots dp_i \tag{3.8}$$

The application of this principle for NoMoS will be thorougly discussed in Chapter 4. In the following section, we now list the systematic effects in NoMoS to get an overview.

3.7. Systematic Effects

In this section, we will give a complete list of systematic effects that may contribute in NoMoS. We separate them into effects that are covered in this work and ones that will be dealt with in other works. Even though we focus on systematic effects related to the magnetic field design, we also include a basic backscattering effect for electrons, as this changes the shape of the drift distance spectrum significantly, hence possibly influencing observable sensitivities on different systematics. The full list is shown in Tab. 3.6.

Table 3.6.: Full list of systematic effects appearing in the NoMoS experiment. The lower part covers effects that are not covered in this work.

Systematic effect	**Parameter(s)**
Magnetic field	
Absolute magnetic field level in $R \times B$ region	$B_{\mathrm{R\times B}}$
Filter magnetic field ratio	r_{F}
Aperture magnetic field ratio	r_{A}
$R \times B$ magnetic field ratio	$r_{\mathrm{R\times B}}$
Detector magnetic field ratio	r_{D}
Curvature angle	α
Radial gradient coefficients	G_1, G_2
Central magn. field line movement	$i_{\mathrm{j,Shift}}$ for $i \in \{x, y\}$, $j \in \{\mathrm{A}, R \times B, \mathrm{D}\}$
Detector	
Electron backscattering coefficients	c_1, c_2, c_3
Other	
Aperture dimensions	x_A, y_A
Neutron beam profile	$w_{n,i}$, $p_{n,i}$, $k_{i,j}$ for $i \in \{x, y\}$, $j \in [1, 2]$
Detector (not considered here)	
Full detector efficiency	η_{tot}
Detector misalignment	Δx_D,Δy_D,$\Delta\theta_D$, $\Delta\phi_D$
Non-active area	r_{active}
$E \times B$ drift and post-acceleration	$s_{E\times B}$, U_{accel}
Aperture scattering	-
Others (Not considered here)	
Earth magnetic field (see Chapter 7)	$B_{E,x}, B_{E,y}, B_{E,z}$
Workfunction elec. potential (protons)	$\Delta\Phi$
Doppler effect (for protons)	T_n
ExB drift in $R \times B$ region due to $\Delta\Phi$ (protons)	-
Stern Gerlach effect	-
Restgas interactions	-
Background effects	-

4. Ingredients of the Transfer in NoMoS

This chapter will throroughly discuss the transfer concept in NoMoS and explain the implementation of all aforementioned included systematic effects in the context of the transfer function. A clear boundary is drawn between these systematic effects and the ones related to the detection system. These will be covered in the PhD thesis of Waleed Khalid [Kha21] in detail. In the first part of this chapter, we illustrate all the ingredients of the transfer in NoMoS in Secs. 4.1 through 4.3. In Sec. 4.4, all components are combined to the full transfer that is used in this work. Note, that the transport through the system will be described in a specific frame. The motion in drift direction is pointing in x direction. Nonetheless, for the second perpendicular coordinate, used in the transfer function, the global y coordinate is suboptimal, due to the fact that we would have to descibe the curved path in y in addition to all transport effects. Instead, in the reference of the transfer function we always use a local perpendicular coordinate, whose origin follows the curved path through the system, still depicted by the variable y.

4.1. Input Functions

In this section, we discuss input functions defining the input parameter space of the particles entering NoMoS, e.g. the incident energy and angle. This is done using theoretical descriptions of the decay spectra. These systematic factors have a fundamental impact on the transfer spectrum shape and need to be understood accordingly well. They also include the observable dependence, that can be fitted with the drift distance spectrum.

4.1.1. Decay Spectrum

There are multiple established theoretical descriptions of the decay products' available energy spectra. They differ in varying amount of corrections and approximations. For both electrons and protons, we use [Glü93]. The electron spectrum $\omega_e(E_e)$ includes the Coulomb correction as well as the inner and outer radiative correction. The respective proton spectrum $\omega_p(E_p)$ includes the proton recoil, Coulomb and radiative corrections up to order-α. NoMoS mainly deals with the momenta instead of the energies, which is why in general, the spectra are transformed in this work using the following equations

$$E(p) = \sqrt{m^2 + p^2} \tag{4.1}$$

$$w(p)dp = w(E(p))dE(dp/dE) \tag{4.2}$$

As NoMoS works with unpolarized neutrons, the decay products are emitted isotropically, which is described by $\sin\theta_0$ for the incident azimuthal angle. The polar angle is uniformly distributed, which is why no function is required.

4.1.2. Neutron Beam Profile

Independent of whether or not NoMoS is used as a standalone spectrometer or in combination with an external decay volume, a neutron beam enters a decay volume, which is magnetically coupled to the rest of NoMoS. This beam has a specific cross section, density distribution, divergence and an orientation relative to the experiment. These properties influence the local neutron density within the collectable decay volume, requiring a description. In this work, we are limiting ourselves to a 2D density distribution description in the perpendicular coordinates of the particle's decay point $(x_{\mathrm{DV}}, y_{\mathrm{DV}})$. We approximate this distribution to zeroth order with a trapezoid per dimension $n_x(x_{\mathrm{DV}})$ and $n_y(y_{\mathrm{DV}})$, the former being illustrated in Fig. 4.1 with examplatory values. The chosen parameter set is the following (per coordinate):

- A total width w_{n}, giving the length of the beam's boundaries
- A plateau p_{n}, giving the length of the trapezoid plateau

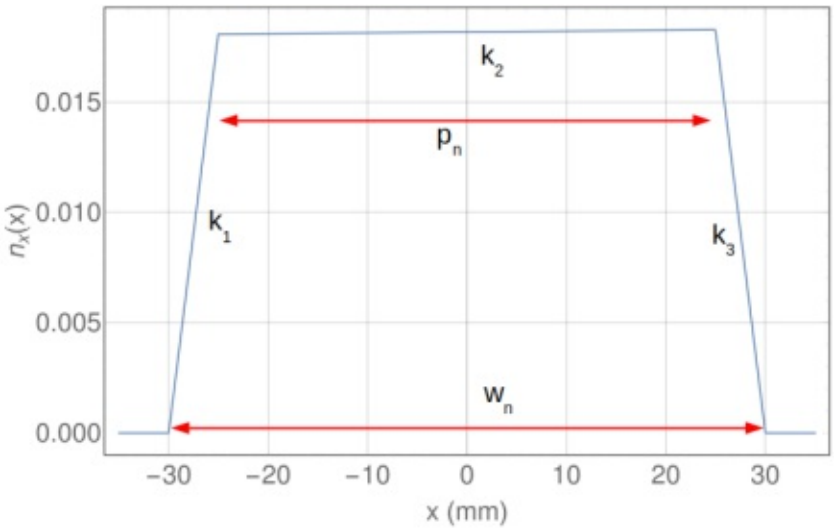

Figure 4.1.: Normed trapezoid distribution for the neutron beam density in the x-coordinate. The total width is $w_{\mathrm{n},x} = 60$ mm, the plateau $p_{\mathrm{n,x}} = 50$ mm, and the three slopes $k_{1,x}, k_{2,x}, k_{3,x}$ are 0.9, 0.001, and -0.9.

- Three slopes k_1, k_2, k_3, giving the slopes of the three different lines

Note, that k_3 is not an independent variable and can be expressed by the other parameters. For the 2D description, both single dimension functions are combined to

$$n(x_{\mathrm{DV}}, y_{\mathrm{DV}}) = n_x(x_{\mathrm{DV}}) n_y(y_{\mathrm{DV}}) \tag{4.3}$$

Eventhough a real neutron beam profile can be significantly more complex, this simplistic model should give a first glimpse on the experiment's sensitivity to it. In all further investigations, we will use the following values:

$$w_{\mathrm{n},x} = 60\,\mathrm{mm}, \quad p_{\mathrm{n,x}} = 50\,\mathrm{mm}, \quad k_{1,x} = 0.9, \quad k_{2,x} = 0, \quad k_{3,x} = -0.9 \tag{4.4}$$

$$w_{\mathrm{n},y} = 100\,\mathrm{mm}, \quad p_{\mathrm{n,y}} = 90\,\mathrm{mm}, \quad k_{1,y} = 0.9, \quad k_{2,y} = 0, \quad k_{3,y} = -0.9 \tag{4.5}$$

4.2. Systematic Effects with Weighing Character

This section tackles systematic effects in our system, that modify the transfer via a weighting function, e.g. the aperture edge effect.

4.2.1. Aperture Edge Effect

In our formulation of the transfer function, we calculate the particle position at the aperture (x_A, y_A). With this, the aperture transmission can to first order be described by a boolean function, that is restricted in x and y, shown in Equ. 4.6.

$$\text{Apert}(x_A, y_A) = \begin{cases} 1 & x_{A,\text{Offset}} - x_{AA}/2 < x_A < x_{A,\text{Offset}} + x_{AA}/2 \wedge \\ & y_{A,\text{Offset}} - y_{AA}/2 < y_A < y_{A,\text{Offset}} + y_{AA}/2 \\ 0 & \text{otherwise} \end{cases} \tag{4.6}$$

with $x_{A,\text{Offset}}$ being the aperture's offset from the origin and x_{AA} being the aperture's size in x, as well as their respective quantities in the y coordinate.

Of course, the aperture is more accurately described by a 3D object. This leads to a more complex transmission description as well as the possibility of scattering at the aperture (and changing the particle's properties). Nonetheless, the aforementioned approximation should give an informative view on the experiment's sensitivity to aperture properties. In all further investigations, the following numbers will be used (offset in x to roughly centralize the beam at the detector):

$$x_{AA} = 1\,\text{cm} \quad y_{AA} = 3.5\,\text{cm}, \quad x_{A,\text{Offset}} = 3\,\text{cm} \quad y_{A,\text{Offset}} = 0\,\text{cm} \tag{4.7}$$

4.2.2. Backscattering at Main Detector

Backscattering at the detector is a significant systematic effect that

1. reduces the number of detected primary particles
2. may lead to reduced deposited signal in the detector from a primary particle
3. may lead to secondary signal (protons that are reflected by the proton post-acceleration after backscattering)

The latter two points will not be covered in this work and the corresponding backscattering description, as this (as well as other detector related systematic effects) will be covered in Waleed Khalid's PhD thesis [Kha21]. We content ourselves with point 1 above, as this has the biggest effect on the drift spectrum. A very basic backscattering loss function for electrons on a silicon detector with a passivation layer of 15 nm (Al) is given below [Kha21]:

Table 4.1.: Fitted backscattering coefficients (see Equ. 4.8), courtesy of W. Khalid.

c_1	c_2	c_3
0.106	-1.043×10^{-4}	9.64×10^{-7}

$$\mathrm{BS}_{\mathrm{loss}}\left(T_e, \theta_{\mathrm{D}}\right) = 1 - \left(c_1 + c_2 T_e + c_3 \theta_{\mathrm{D}}^3\right) \tag{4.8}$$

The coefficients c_1, c_2 and c_3 are fitted to backscattering simulations with the results shown in Table 4.1. The function depends on the electron kinetic energy T_e and the impact pitch angle at the detector θ_{D}.

Note that we include the backscattering due to its significant effect on the form of the drift distance spectrum but we don't investigate its systematic effect on the observables as this will be covered in the PhD thesis of Waleed Khalid [Kha21].

4.3. Particle Motion in the Transfer Function

The $R \times B$ drift in its most basic form is given by Equ. 2.32. Nonetheless, this is just an approximation of the real world scenario, in which $\vec{R}$ and $\vec{B}$ do not behave ideally. Also, an $R \times B$ spectrometer has a significant radial gradient in the $R \times B$ region's magnetic field $\nabla_r B_{R\times B}$ that should be considered. Furthermore, the adiabatic transport has to be described properly through the system. These points are discussed in the following subsections.

4.3.1. $R \times B$ Drift: Radial Magnetic Field Gradient

Due to the fact that the drift directly depends on $B_{\mathrm{R\times B}}$, the radial B-field gradient B_∇ should be considered precisely. An accurate model describing the observed magnetic field B_∇ is a polynomial of second order

$$B_\nabla(y_{R\times B\,,\mathrm{GC}}) = B_{\mathrm{R\times B}}\left(1 - G_1\, y_{R\times B\,,\mathrm{GC}} + G_2\, y^2_{R\times B\,,\mathrm{GC}}\right) \tag{4.9}$$

with two coefficients G_1, G_2. This leads to a more realistic drift formula

$$D^{\mathrm{1st}}_{x,\nabla} = \frac{p\alpha}{qB_\nabla(y_{R\times B\,,\mathrm{GC}})} f\left(\theta_{R\times B}\right) \tag{4.10}$$

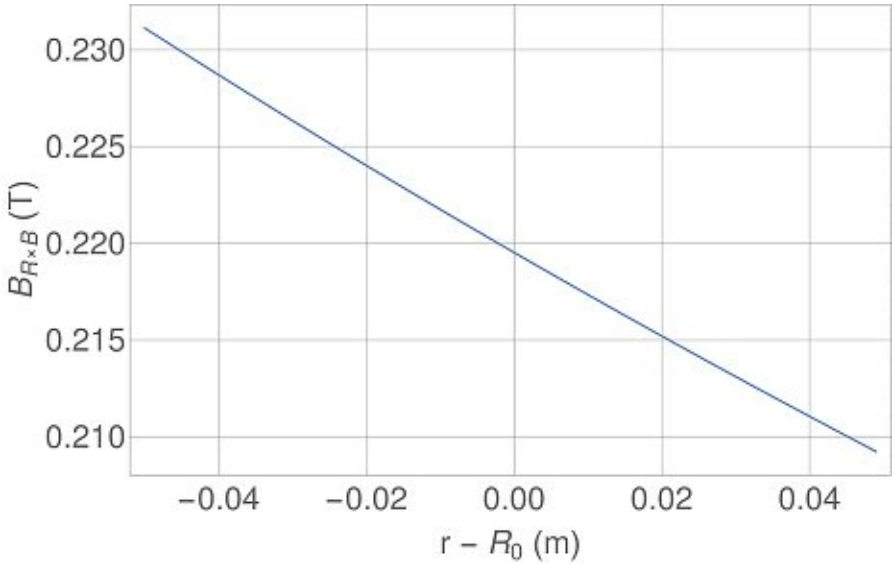

Figure 4.2.: The magnetic field's norm along the radial coordinate in the center of the $R \times B$ region. $x = y = 0$ and z represents the radial coordinate at an intermediate geometrical curvature angle of $\alpha_{\text{geo}} = 90°$. We subtract the central curvature radius R_0 from the radial coordinate r to indicate the geometrical center position.

In Fig. 4.2, the absolute magnetic field strength along the radial coordinate in the $R \times B$ region is shown (at the central point $\alpha_{\text{geo}} = 90°$, the radial coordinate points in z-direction $\hat{r} = \hat{z}$).

We show a more detailed investigation of the radial gradient's description in Sec. 5.2. Note, that in principle, due to the particles gyrating through the $R \times B$ region and the radial gradient not being linear, the mean magnetic field over one gyration is different compared to the mean magnetic field of the guiding center. This effect is roughly $\Delta B/B = 1 \times 10^{-4}$ for the biggest gyration radii (large momentum and large pitch angle). Nonetheless, in the first order guiding center motion, the gradient induces the $R \times B$ drift with the magnetic field at the guiding center position, not the particle position.

4.3.2. Adiabatic Particle Motion

In Sec. 2.2, we have shown how adiabatic particle motion can be described with the magnetic flux conservation. The particle position is required in several areas of NoMoS, which is why the local magnetic field ratios have to be known.

Motion due to Magnetic Flux Conservation

We define all ratios relative to the magnetic field at the decay point B_{DV}, leading to the following ratios:

$$r_{\mathrm{F}} = \frac{B_{\mathrm{F}}}{B_{\mathrm{DV}}}, \quad r_{\mathrm{A}} = \frac{B_{\mathrm{A}}}{B_{\mathrm{DV}}}, \quad r_{R\times B} = \frac{B_{R\times B}}{B_{\mathrm{DV}}}, \quad r_{\mathrm{D}} = \frac{B_{\mathrm{D}}}{B_{\mathrm{DV}}} \tag{4.11}$$

with the indices F, A, $R \times B$ and D for the filter, aperture, $R \times B$ and detection regions, respectively. All regions except the $R\times B$ region are defined as a 2D plane perpendicular to the magnetic field flux. We assume the respective magnetic fields in the different regions to be constant. The method of determination and more detailed definitions will be thoroughly discussed in Ch. 5. With these equations, a particle movement perpendicular to the magnetic field lines due to a changing B-field can be described with Equ. 2.23.

As an example, we look at the guiding center motion of a particle starting at the decay volume and moving to the aperture. We assume a perfect magnetic field where the central magnetic field line follows the central geometrical axis. Then, the following adiabatic equation can be defined for the position of the particle's guiding center (GC) at the aperture

$$x_{\mathrm{A,GC}} = x_{\mathrm{DV,GC}} \frac{1}{\sqrt{r_{\mathrm{A}}}} \tag{4.12}$$

Furthermore

$$x_{R\times B,\mathrm{GC}} = x_{\mathrm{A,GC}} \sqrt{\frac{r_{\mathrm{A}}}{r_{R\times B}}} = x_{\mathrm{DV,GC}} \frac{1}{\sqrt{r_{R\times B}}} \tag{4.13}$$

Motion of Central Magnetic Field Line

Nonetheless, the effect described above doesn't consider an important aspect of the real experiment. One of the biggest factors, influencing the ideal magnetic field design, is the cross talk between the beam preparation area and the detection region as well as the stray field from the $R \times B$ region within the others. With these effects, the central magnetic field line of the assumed flux tube may move away from the geometrical coordinate center. As the shift defined by Equ. 2.23 only describes movement relative to the central field line of the flux tube, such a movement has to be understood in addition.

This can easily be investigated by checking the central magnetic field line in the system and its position relative to the geometrical center (further discussed in Sec. 5.2). With this, the shifts $X_{\mathrm{A,Shift}}$,$X_{R\times B\ \mathrm{,Shift}}$,$X_{\mathrm{D,Shift}}$ and their corresponding y-axis counterparts can be determined. This leads to the following correction:

$$x_{\mathrm{A,GC}} = x_{\mathrm{DV,GC}}\frac{1}{\sqrt{r_{\mathrm{A}}}} + X_{\mathrm{A,Shift}} \tag{4.14}$$

or

$$x_{R\times B\mathrm{,GC}} = x_{\mathrm{DV,GC}}\frac{1}{\sqrt{r_{R\times B}}} + X_{R\times B\mathrm{,Shift}} \tag{4.15}$$

4.4. Complete Transfer Equations

The full transfer of particles through NoMoS is comprised of the input functions, systematic weighting functions and the adiabatic transport including movement due to magnetic field changes, the $R\times B$ drift (all mentioned in the sections above) as well as gyration effects. In detail, all effects are listed below:

- **Input functions**
  - Neutron beam profile $n(x_{\mathrm{DV}}, y_{\mathrm{DV}})$
  - Decay spectrum $\omega_e(p)\sin(\theta_0)$
- **Systematic weighting functions**
  - Aperture edge effect $\mathrm{Apert}(x_A, y_A)$
  - Backscattering at detector $\mathrm{BS}_{\mathrm{loss}}(T_e, \theta_{\mathrm{Det}})$
- **Particle transport (details in Tab. 4.2)**

This stepwise development of the particle transport can also be written mathematically, shown below for both perpendicular coordinates:

Table 4.2.: A structured summary of the transport steps taken by particles through NoMoS. See Fig. 4.3 and 4.4 for an illustration of the transport steps.

Region	**Transfer**	**Description**
Decay volume	$x_{\mathrm{DV}}, y_{\mathrm{DV}}$ $\downarrow$ $x_{\mathrm{DV,GC}}, y_{\mathrm{DV,GC}}$	particle emission point to guiding center (gyration)
	$\downarrow$	Adiabatic motion
Aperture	$x_{\mathrm{A,GC}}, y_{\mathrm{A,GC}} \rightarrow x_{\mathrm{A}}, y_{\mathrm{A}}$	Calc. particle position at the aperture (gyration)
	$\downarrow$	Adiabatic motion
$R \times B$ region	$x_{R\times B,\mathrm{GC}}, y_{R\times B,\mathrm{GC}}$ $\downarrow$ $x_{\mathrm{Drift,GC}}, y_{\mathrm{Drift,GC}}$	Add $R \times B$ drift
	$\downarrow$	Adiabatic motion
Detector	$x_{\mathrm{D,GC}}, y_{\mathrm{D,GC}}$ $\downarrow$ $x_{\mathrm{D}}, y_{\mathrm{D}}$	Guiding center to particle position on detector (gyration)

$$
\begin{aligned}
x_{\mathrm{D}} = \quad & [(x_{\mathrm{DV}} - r_{\mathrm{DV,G}} \cos\phi_{\mathrm{DV}}) \\
& \times \sqrt{1/r_{R\times B}} \\
& + D_{R\times B}\ ] \\
& \times \sqrt{r_{R\times B}\,/r_{\mathrm{D}}} + x_{\mathrm{D,Shift}} \\
& + r_{\mathrm{D,G}} \cos\phi_{\mathrm{D}}
\end{aligned} \tag{4.16}
$$

$$
\begin{aligned}
y_{\mathrm{D}} = \quad & (y_{\mathrm{DV}} - r_{\mathrm{DV,G}} \sin\phi_{\mathrm{DV}}) \\
& \times \sqrt{1/r_{\mathrm{D}}} + y_{\mathrm{D,Shift}} \\
& + r_{\mathrm{D,G}} \sin\phi_{\mathrm{D}}
\end{aligned} \tag{4.17}
$$

Equations 4.16 and 4.17 represent the argument of the transfer functions T_x and T_y used for NoMoS. The calculations include the gyration radius r_{G} at various positions as well as the local phase angle ϕ, both indicated with an additional index for the respective region. The aperture edge effect function requires the particle position at the aperture position, given by

$$x_{\mathrm{A}} = (x_{\mathrm{DV}} - r_{\mathrm{DV,G}} \cos\phi_{\mathrm{DV}}) \sqrt{1/r_{\mathrm{A}}} + x_{\mathrm{A,Shift}} + r_{\mathrm{A,G}} \cos\phi_{\mathrm{A}} \tag{4.18}$$

$$y_{\mathrm{A}} = (y_{\mathrm{DV}} - r_{\mathrm{DV,G}} \sin\phi_{\mathrm{DV}}) \sqrt{1/r_{\mathrm{A}}} + y_{\mathrm{A,Shift}} + r_{\mathrm{A,G}} \sin\phi_{\mathrm{A}} \tag{4.19}$$

with the gyration radius and phase angle at the aperture $R_{\mathrm{A,G}}$ and ϕ_{A}. Additionally, the $R \times B$ drift in Equ. 4.16 requires the y-position in the $R \times B$ drift region due to the radial magnetic field gradient. It is given by

$$y_{R\times B,\mathrm{GC}} = (y_{\mathrm{DV}} - r_{\mathrm{DV,G}} \sin\phi_{\mathrm{DV}}) \sqrt{1/r_{R\times B}} + y_{R\times B,\mathrm{Shift}} \tag{4.20}$$

Figure 4.3 and 4.4 illustrate Equs. 4.16 and 4.17 geometrically.

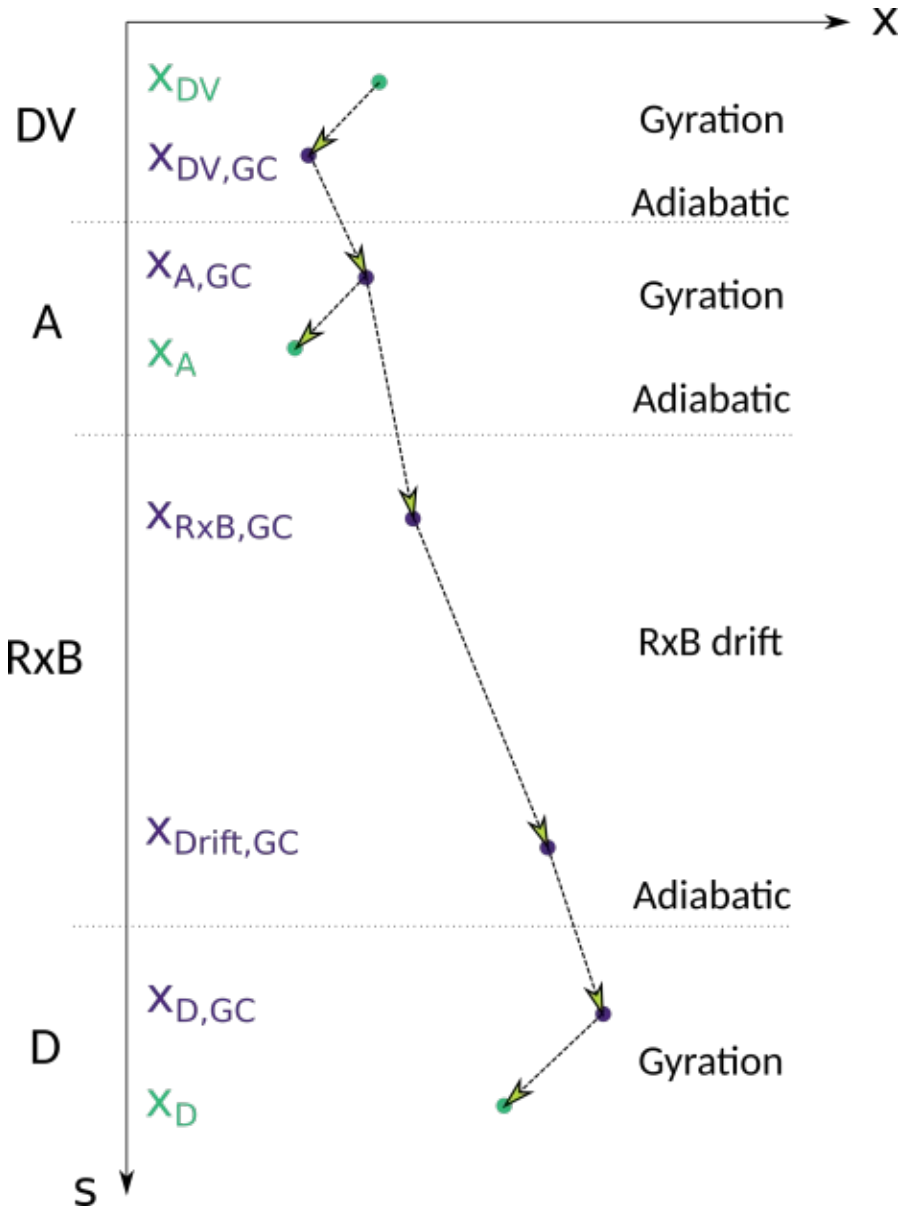

Figure 4.3.: An illustration of the adiabatic particle motion in x step by step through the NoMoS system, describing the steps taken between particle positions at specific regions of interest. Particle positions are colored turquoise, whereas guiding centers are depicted in purple. On the right side, effect sources are written between points.

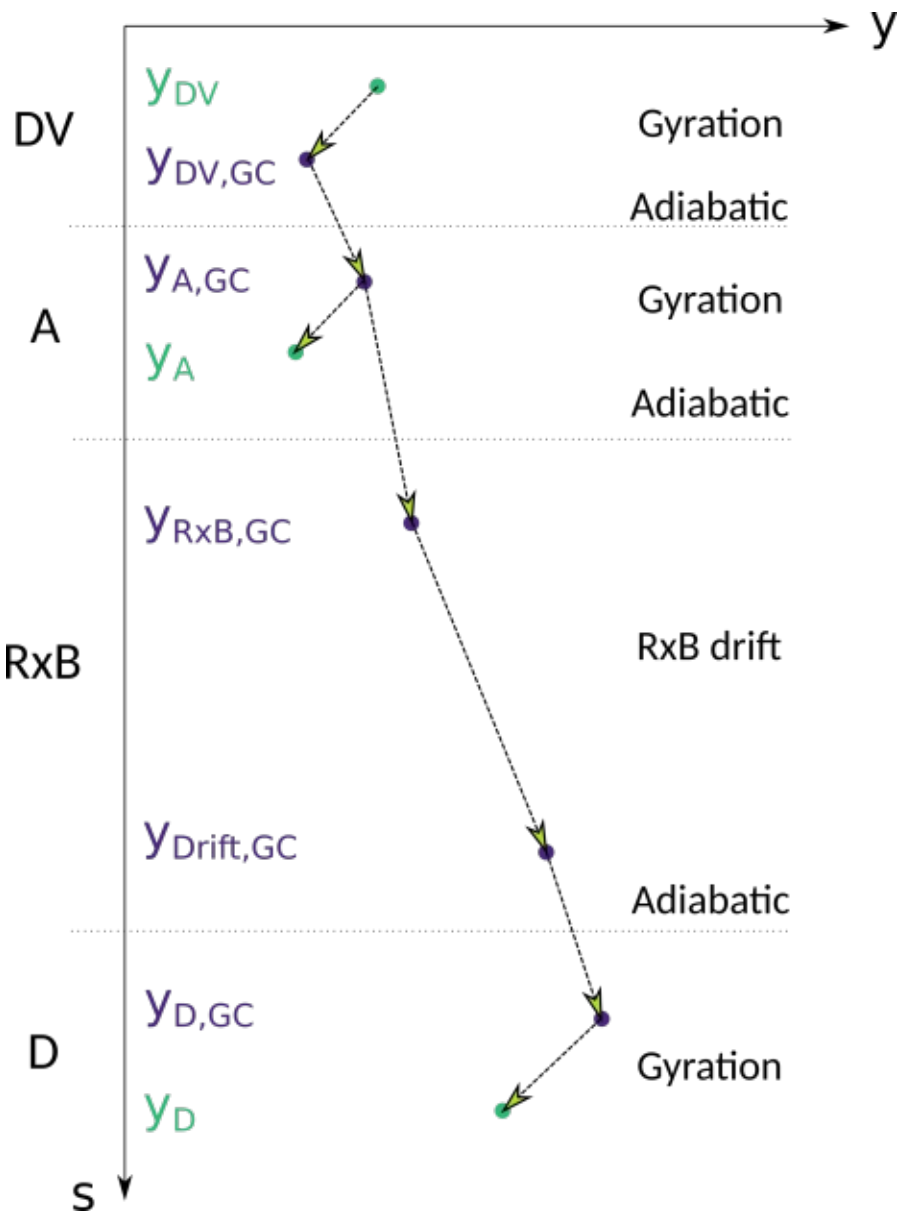

Figure 4.4.: An illustration of the adiabatic particle motion in y step by step through the NoMoS system, describing the steps taken between particle positions at specific regions of interest. Particle positions are colored turquoise, whereas guiding centers are depicted in purple. On the right side, effect sources are written between points. It also includes an optional drift, in case a correction to the $R \times B$ drift in y is considered.

4.5. Performing the Transfer and Investigating its Properties

In this section, the transfer is put together into an equation to produce a two-dimensional drift distance spectrum G. Afterwards, we look into the general behaviour of the integrand to optimize the integration. We will tackle the immense complexity of the transfer integration and show how the integration is conducted.

4.5.1. The Transfer Explicitly Put Together

The following equation shows a seven-dimensional numerical integral over an integrand dependent on systematic parameters s_i.

$$\begin{aligned} G\left(x_{\mathrm{D}}, y_{\mathrm{D}}, s_i\right) &= \int_{\mathcal{S}} \omega_e(p_e, b) \sin\theta_0 \\ &\quad T_x(\ldots, s_i) T_y(\ldots, s_i) \\ &\quad \mathrm{Apert}(x_{\mathrm{A}}, y_{\mathrm{A}}, s_i) \mathrm{BS}_{\mathrm{loss}}(p_e, \theta_0, s_i) n(x_{\mathrm{DV}}, y_{\mathrm{DV}}, s_i) \end{aligned} \tag{4.21}$$

with the seven-dimensional domain $\mathcal{S}$

$$\mathcal{S} = dy_{\mathrm{DV}} dx_{\mathrm{DV}} d\phi_{\mathrm{A}} dp_e d\phi_{\mathrm{DV}} d\phi_{\mathrm{D}} d\theta_0 \tag{4.22}$$

This equation can even be further expanded by integrating over detector bins (with the rectangular detector bin differentials $dx_{\mathrm{D,j}}$ and $dy_{\mathrm{D,j}}$ for bin j). Then, the equation for the drift distance spectrum just changes in its integration domain

$$\begin{aligned} G\left(j, s_i\right) &= \int_{\mathcal{T}} \omega_e(p_e, b) \sin\theta_0 \\ &\quad T_x(\ldots, s_i) T_y(\ldots, s_i) \\ &\quad \mathrm{Apert}(x_{\mathrm{A}}, y_{\mathrm{A}}, s_i) \mathrm{BS}_{\mathrm{loss}}(\ldots, s_i) n(\ldots, s_i) \end{aligned} \tag{4.23}$$

with the nine-dimensional domain $\mathcal{T}$

$$\mathcal{T} = dy_{\mathrm{DV}} dx_{\mathrm{DV}} d\phi_{\mathrm{A}} dp_e d\phi_{\mathrm{DV}} d\phi_{\mathrm{D}} d\theta_0 dx_{\mathrm{D,j}} dy_{\mathrm{D,j}} \tag{4.24}$$

Further discussions will treat the version with integrated bins. The arguments of the single functions in the integrand are as follows:

$$\begin{aligned} T_x &= T_x\left(x_{\mathrm{DV}}, p_e, \phi_{\mathrm{DV}}, \phi_{\mathrm{D}}, \theta_0, x_{\mathrm{D,j}}; \right. \\ &\quad \left. B_{\mathrm{R\times B}}, r_{\mathrm{R\times B}}\ , \alpha, y_{R\times B,\mathrm{GC}}(\ldots, y_{\mathrm{DV}}, y_{R\times B,\mathrm{Shift}}), G_1, G_2, r_{\mathrm{D}}\ , x_{\mathrm{D,Shift}}\right) \end{aligned} \tag{4.25}$$

T_x is the Delta function with Equ. 4.16 as its argument. It therefore adopts all of this equation's arguments. It depends on most integration- as well as a plethora of systematic parameters. Through $y_{R\times B,\mathrm{GC}}$ (Equ. 4.20), it is also coupled to the second detector dimension, complicating the integration (more discussed in the subsequent subsections).

$$\begin{aligned} T_y &= T_y\,(y_{\mathrm{DV}}, p_e, \phi_{\mathrm{DV}}, \phi_{\mathrm{D}}, \theta_0, y_{\mathrm{D,j}}; \\ &\quad B_{\mathrm{R\times B}}, r_{\mathrm{D}}\ , y_{\mathrm{D,Shift}}) \end{aligned} \tag{4.26}$$

T_y is the Delta function with Equ. 4.17 as its argument. It is simpler in its dependence than T_x as there is no drift and no coupling to the x-dimension.

$$\begin{aligned} \mathrm{Apert} &= \mathrm{Apert}\,(x_{\mathrm{DV}}, y_{\mathrm{DV}}, p_e, \theta_0, \phi_{\mathrm{DV}}, \phi_{\mathrm{A}}; \\ &\quad B_{\mathrm{R\times B}}, r_{\mathrm{A}}\ , x_{\mathrm{A,Shift}}, y_{\mathrm{A,Shift}}) \end{aligned} \tag{4.27}$$

The aperture function Apert depends on Equs. 4.18 and 4.19.

$$\begin{aligned} \mathrm{BS}_{\mathrm{loss}} &= \mathrm{BS}_{\mathrm{loss}}\,(p_e, \theta_0; \\ &\quad r_{\mathrm{D}}, c_1, c_2, c_3) \end{aligned} \tag{4.28}$$

The backscattering function $\mathrm{BS}_{\mathrm{loss}}$ has a managable amount of dependencies. Last but not least, the neutron beam profile n is

$$\begin{aligned} n &= n\,(x_{\mathrm{DV}}, y_{\mathrm{DV}}; \\ &\quad w_x, w_y, p_x, p_y, k_{1,x}, k_{2,x}, k_{1,y}, k_{2,y}) \end{aligned} \tag{4.29}$$

It depends on the particle's incident position as well as the profile parameters (four per dimension).

All in all, a nine-dimensional numerical integral is a highly complex task and there are 27 systematic parameters. Nonetheless, with a few tricks, this integral becomes manageable.

4.5.2. The Order of the Integration and Behaviour of the Integrand

Looking at the nine-dimensional domain to integrate over in Equ. 4.24, the order of integration is an important consideration for its success and performance. Furthermore, the integrand has to be investigated to choose the optimal integration routine.

Choosing the Best Integration Order

Whatever two first integration dimensions are chosen, they resolve the two delta functions / transfer functions T_x and T_y. The integration parameter is therefore replaced in all its appearances in the integrand, indicated in the following equation.

$$\int \delta\left(x - f(y)\right) g(x) dx = g(f(y)) \tag{4.30}$$

Two requirements to the first two integration dimensions are obtained from this:

- The argument of the transfer function (Equs. 4.16 and 4.17) has to be solvable for the intended parameter,
- the parameter has to be replaced in every appearance within the integrand with relative ease.

The momentum p_e and incident pitch angle θ_0 appear at many places of the transfer functions' arguments and are not a good fit for the first integrations. The integration over the detector bins should be integrated last as this is the clear summation of contributions. Due to the fact, that the arguments are very easily solvable for the particle's position at the decay volume (x_{DV},y_{DV}) and that performance is better, we chose these as the first integration dimensions over the phase angles.

How to Apply the Transfer Function

Solving Equs. 4.16 and 4.17 for x_{DV} and y_{DV}, we obtain

$$y_{\mathrm{DV}} = (y_{\mathrm{D}} - r_{\mathrm{D,G}} \sin\phi_{\mathrm{D}} - y_{\mathrm{D,Shift}}) \sqrt{r_{\mathrm{D}}} + r_{\mathrm{DV,G}} \sin\phi_{\mathrm{DV}} \tag{4.31}$$

and

$$\begin{aligned} x_{\mathrm{DV}} = \quad & \Big[(x_{\mathrm{D}} - r_{\mathrm{D,G}} \cos\phi_{\mathrm{D}} - x_{\mathrm{D,Shift}}) \sqrt{r_{\mathrm{D}}/r_{R\times B}} \\ & - D_{R\times B}\,(y_{R\times B,\mathrm{GC}})\Big] \\ & \times\sqrt{r_{R\times B}} + r_{\mathrm{DV,G}} \cos\phi_{\mathrm{DV}} \end{aligned} \tag{4.32}$$

Note, that in Equ. 4.32, the drift depends on $y_{R\times B,\mathrm{GC}}$, which in turn depends on y_{DV}. This has to be replaced as well. This circumstance couples the two coordinates with each other. The next step is to replace y_{DV} and then x_{DV} in every appearance within the integrand. This is the case in $\mathrm{Apert}(x_{\mathrm{A}}(x_{\mathrm{DV}}), y_{\mathrm{A}}(y_{\mathrm{DV}}))$ as well as in n directly. It leaves us with a seven-dimensional integral with the integrand I_7. Note, that in the following, we will treat all phase angles of gyration as independent variables. An independence between ϕ_{DV} and ϕ_{A} would be valid for a sufficiently large decay volume. In Subsec. 7.2.2, we discuss possible relations between the phase angles, that would simplify the integral. Nonetheless, we don't find such a easily describable relation.

The Integrand I_7 Dependent on ϕ_{A}

Next, we investigate the integrand I_7 dependent on the gyration phase angle at the aperture ϕ_{A} because there is a special behaviour to it, that we can use to improve the performance of the integral. Figure 4.5 illustrates this. The reason for this special form is that the aperture function Apert is a boolean type and only a restricted phase space of ϕ_{A} is allowed to go through.

An integration of I_7 with a conventional integration rule would not only be inefficient but even counter-productive. Looking at the functional dependence of x_{A} and y_{A} on ϕ_{A}, we obtain the following boundary points of the integrands stepping points

$$x_{\mathrm{A,Offset}} - x_{\mathrm{AA}}/2 == x_{\mathrm{A}}(\phi_{\mathrm{A,x,min}}), \quad x_{\mathrm{A,Offset}} + x_{\mathrm{AA}}/2 == x_{\mathrm{A}}(\phi_{\mathrm{A,x,max}}) \tag{4.33}$$

$$y_{\mathrm{A,Offset}} - y_{\mathrm{AA}}/2 == y_{\mathrm{A}}(\phi_{\mathrm{A,y,min}}), \quad y_{\mathrm{A,Offset}} + y_{\mathrm{AA}}/2 == y_{\mathrm{A}}(\phi_{\mathrm{A,y,max}}) \tag{4.34}$$

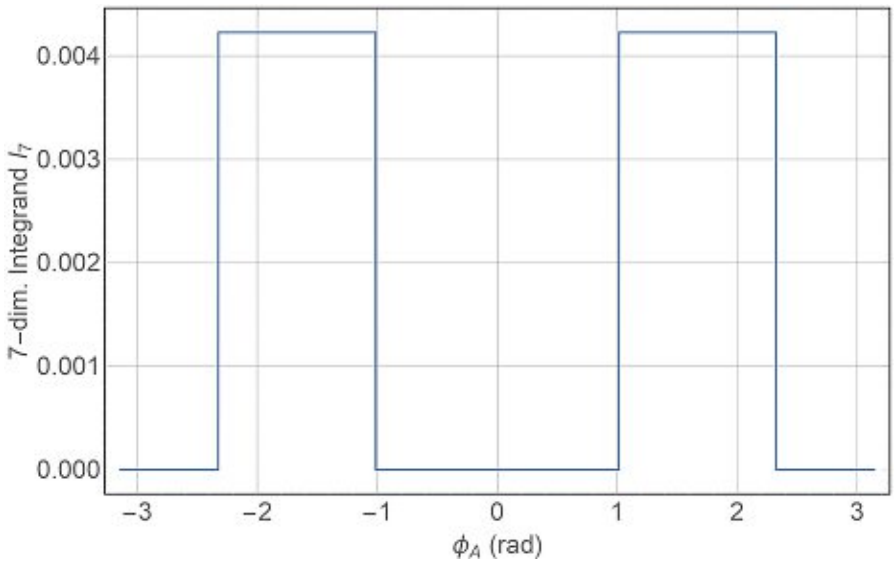

Figure 4.5.: The seven-dimensional integrand I_7 dependent on ϕ_A for examplatory parameter values.

These four equations represent the boundary points of a particle at the aperture in both coordinates. We can easily manually sum up these steps. We simply divide the region into subregions with the boundary points $\mathcal{B}$

$$\mathcal{B} = \{-\pi, \phi_{\mathrm{A,x,min}}, \phi_{\mathrm{A,x,max}}, \phi_{\mathrm{A,y,min}}, \phi_{\mathrm{A,y,max}}, \pi\}. \tag{4.35}$$

Note, that this list might have to be reordered, because of the periodicity of the trigonometric functions. Then, the integral over ϕ_A is

$$I_6 = \sum_{i=0}^{4} I_7 \left(\phi_\mathrm{A} = \frac{\mathcal{B}_{i+1} - \mathcal{B}_i}{2}\right) \times (\mathcal{B}_{i+1} - \mathcal{B}_i) \tag{4.36}$$

This sum evaluates the integrand at the center of each subregion and multiplies by the subregion's length in ϕ_A. Basically, it is just a Riemann sum.

4.5.3. The Integrand I_6 Dependent on p_e

After the integration over the phase angle at the aperture ϕ_A, we conduct the next over the momentum p_e. The reason for this is that we can again use information

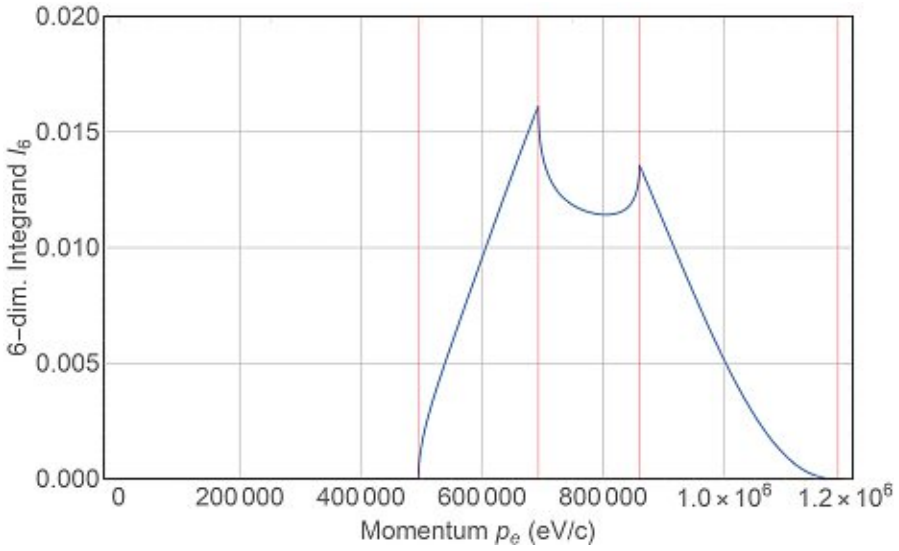

Figure 4.6.: The six-dimensional integrand I_6 dependent on the momentum p_e for examplatory parameter values. The red vertical lines represent boundary points $\mathcal{P}$, which are defined below.

about the transfer to optimize the integration. Figure 4.6 shows the integrand I_6 dependent on the momentum. This illustrates the possible momenta for a given detector position (and other defining parameters).

I_6 has two significant spikes and is continuous otherwise with a global limitation on both sides. The latter are the minimum and maximum momenta able to reach the specific detector position. The spikes can be explained by effects of the aperture. For this, we illustrate the aperture in Fig. 4.7 with different sized circles illustrating different gyration radii.

The aperture is shown as a blue boundary. Additionally, circles with different radii are shown, representing the gyration radius of a particle with varying momentum, according to Equ. 2.16. The two effects leading to the spikes in the integrand I_6 are:

- The transfer procedure calculates the detector signal at a specific detector position x_D. This, in combination with the momentum parameter, fixates the particle's guiding center at the aperture. By changing the momentum, another guiding center is required to reach the same detector position.
- The gyration radius and therefore the size of the indicated circle's segment that is able to be transmitted through the aperture is dependent on the

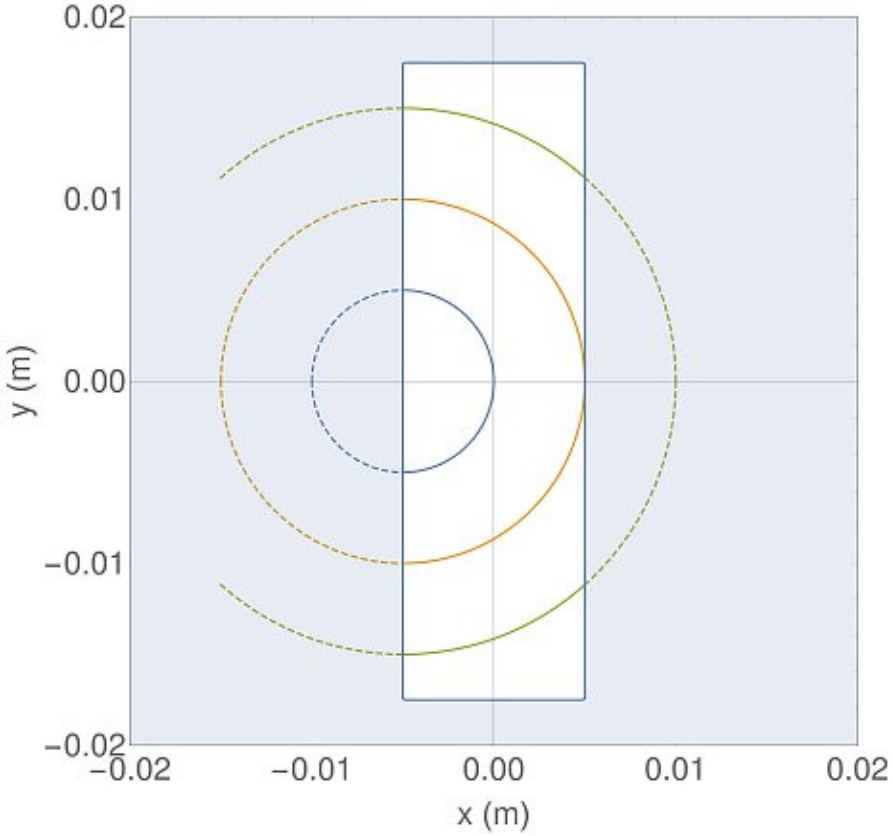

Figure 4.7.: An examplatory aperture opening and circles with different radii, representing possible phase angles at the aperture ϕ_A of a particle with its guiding center at $(x, y) = (-0.005, 0)$ m. If a segment of a circle is within the aperture opening, it is drawn full, otherwise dashed.

momentum.

These two effects result in a change of the allowed relative arc length, illustrated by the ratio of dashed to non-dashed circle segment in the figure. Due to the two boundaries per dimension, there are extremal points in the transmission. If the guiding center in Fig. 4.7 is figuratively moving from left to right, there is an increase of the integrand (the transmitted arc length) as long as the second boundary (at $x = 0.005\text{m}$) is not reached. Then, the integrand is reduced again until the first boundary is not a limiting factor to the circle any more, increasing the integrand towards the second maximum again.

This means, that we can calculate the momentum values of these spikes as well as the global limits, solving the equations

$$x_{\text{A,Offset}} - x_{\text{AA}}/2 == x_{\text{A}}(p_{\text{e,x,min}}), \quad x_{\text{A,Offset}} + x_{\text{AA}}/2 == x_{\text{A}}(p_{\text{e,x,max}}) \tag{4.37}$$

$$y_{\text{A,Offset}} - y_{\text{AA}}/2 == y_{\text{A}}(p_{\text{e,y,min}}), \quad y_{\text{A,Offset}} + y_{\text{AA}}/2 == y_{\text{A}}(p_{\text{e,y,max}}) \tag{4.38}$$

Note, that in general, x_{A} and y_{A} functionally depend on ϕ_{A}, which at this point has already been integrated out. Nonetheless, a trick can help partially solve this problem. Plotting $p_{\text{e,x,min}}$ and $p_{\text{e,x,max}}$ in Fig. 4.8 dependent on ϕ_{A} and confirming with other parameter values, there are global extrema in ϕ_{A}, giving us the extremal momenta values (the lowest value is always at $\phi_{\text{A}} = 0$ and the maximum at $\phi_{\text{A}} = -\pi = \pi$). In the worst case, this approximation overestimates the global boundaries, but never underestimates them.

The figure also shows a black line, indicating the maximum momentum from neutron decay p_{max}. The red lines in Fig. 4.6 result from the values $p_{\text{e,x,min}}(\phi_{\text{A}} = 0)$, $p_{\text{e,x,min}}(\phi_{\text{A}} = -\pi)$, $p_{\text{e,x,max}}(\phi_{\text{A}} = 0)$ and $p_{\text{e,x,max}}(\phi_{\text{A}} = -\pi)$.

Unfortunately, applying the same trick to the y-dimension doesn't work out the same way, due to the fact that there are no global minima and maxima for the whole parameter space. For example, this strongly depends on y_{D}, as is expected, because this determines, if a restriction in the y-coordinate plays a role in the integrand or not. Nonetheless, any further effect in y just leads to stronger restrictions of the integrand, potentially reducing the overall range of the non-zero integrand or adding additional features (like the spikes seen in Fig. 4.6). To make sure, that these structures are properly considered, we allow the integration procedure

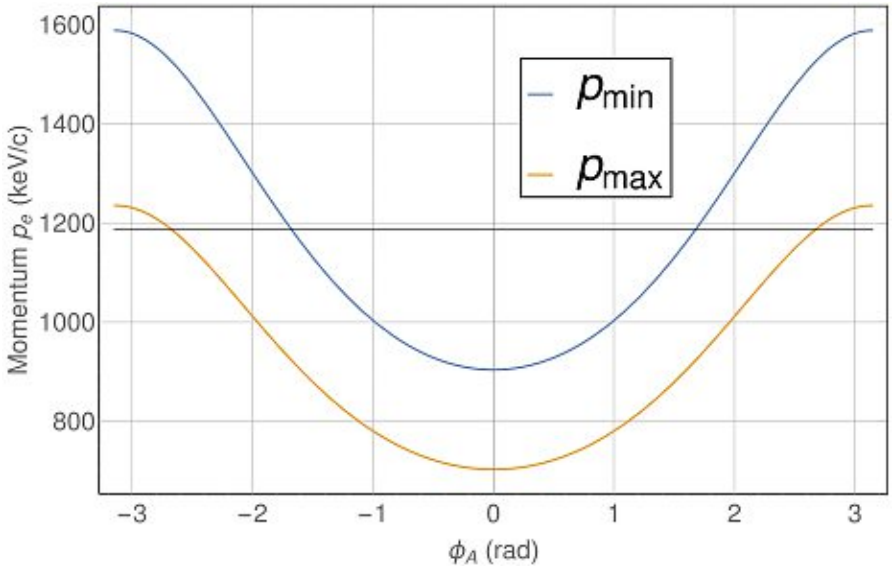

Figure 4.8.: The momentum limitations given by solving Equ. 4.37 dependent on ϕ_{A}. The horizontal black line indicates the maximum momentum of electrons in neutron beta decay. The minima of both functions always is at $\phi_{\mathrm{A}} = 0$ and the maxima at $\phi_{\mathrm{A}} = -\pi = \pi$.

to subdivide the regions multiple times (recursions in conjunction with the error estimation is handled by the so-called *Integration Strategy*, see Subsec. 2.3.4).

4.5.4. Subsequent Integration Dimensions

The remaining integration dimensions don't require any tricks and perform relatively smoothly (as the integrands are also very smooth). This then leads to a drift distance spectrum with bins that have been integrated over. An examplatory result of this procedure is shown in Fig. 4.9.

In this particular case, the chosen detector binning is of the form: $x_{\mathrm{D}} \in [-0.07, 0.045]$ m in steps of $\Delta x_{\mathrm{D}} = 0.005$ m, $y_{\mathrm{D}} \in [-0.055, 0.055]$ m in steps of $\Delta x_{\mathrm{D}} = 0.01$ m. This leads to a total of $23 \times 11 = 253$ bins. The shown figures interpolate the entries linearly. The numerical integration is computationally expensive with a rough computation time of 32 hours for a 16 core modern computation node. For further investigations with the transfer functions, shown in the next chapter, many drift distance spectrum calculations are required.

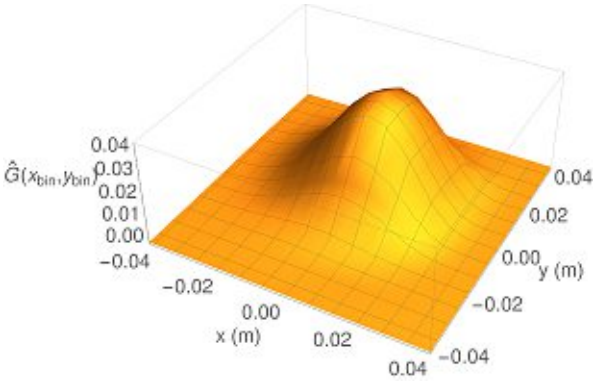

(a) A 3D plot of the normalized drift distance spectrum.

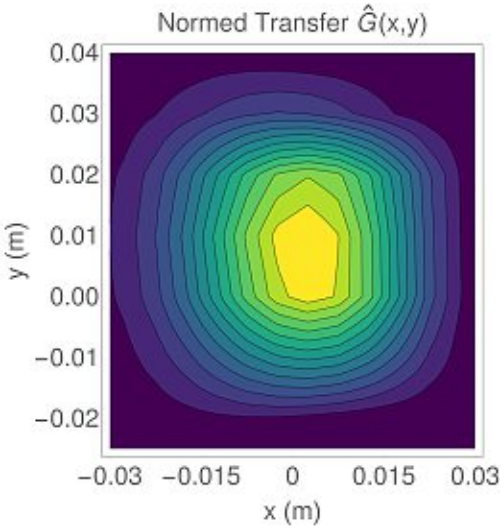

(b) A 2D contour plot of the normed drift distance spectrum.

Figure 4.9.: A normed drift distance spectrum $\hat{G}(x_{\text{bin}}, y_{\text{bin}}) = G_{\text{bin}} / \sum G_{\text{bin}}$ in different plotting styles for the NC configuration with electrons (drift in negative x-direction). Both plots use a linear interpolation of the bin values. The aperture has an offset of $x_{\text{A,Offset}} = 0.03$ m. Even though the spectrum values drop relatively quickly at the borders of the detector, the range of non-zero bin entries at least covers the plotted area.

5. Systematic Effect Investigations

This chapter is the highlight of this work, focussing on the presentation of our results from the systematic investigations for the Fierz term determination. Note that we discuss results for the normal conducting configuration only, as the investigations are completely analogous for the super-conducting variant. For the latter, we therefore only show the final numbers (the systematic parameters are listed in App. B). First, our methods of investigation are shown in Sec. 5.1. It explains the tools used to check systematic effects and extract sensitivities of observables on all systematics effects discussed in the previous chapters. Then, we present the determination of systematic parameters in NoMoS in Sec. 5.2, providing the input for the transfer as well as an indication for the parameters' accuracy. After that, we shortly compare an electron Monte Carlo drift distance spectrum with a transfer one in Sec. 5.3. Subsequently, results for observable sensitivities on systematic parameters are shown and discussed in Sec. 5.4 with a systematic effect budget for a determination of b. Finally, we propose experimental tests to further check systematic effects in Sec. 5.5.

5.1. Methodology of Investigation

There is a variety of methods that can be used to investigate an experiment's systematic effects. Even though Monte Carlo simulations have become more and more popular, we don't want to completely rely on them. This is why the transfer function was introduced. It is able to construct the detector signal by describing the particle transfer analytically and integrating over the phase space numerically. Additionally, there are multiple methods to determine systematic parameters. All of them will be discussed in the following subsections.

5.1.1. (Modified) Magnetic Field Lines

A basic but highly instructive technique is the investigation of magnetic field lines. They are defined with the following equation

$$\vec{r}_{i+1} = \vec{r}_i + s\hat{B}_i \tag{5.1}$$

with $\vec{r}_i$ being the i-th step (and the consecutive i+1 step) in the three-dimensional line, s a step size that should be chosen small enough, so that the solution converges to required accuracy, and the normalized magnetic field vector $\hat{B}_i$ at the position $\vec{r}_i$. With these, the overall magnetic field behaviour can be investigated. It illustrates the magnetic field flux, including the deviation of the central magnetic field line from the geometric center, as well as the change in the conserved flux cross section, discussed in Subsec. 4.3.2. For our investigations, a step size $s = 5 \times 10^{-4}$ m is enough for the required accuracy.

Interestingly, this tool can be expanded with some knowledge about the $R \times B$ drift. This expansion is illustrated in Equ. 5.2.

$$\vec{r}^{*}_{i+1} = \vec{r}^{*}_i + s\hat{B}_i + D^{1\text{st}}(\Delta\alpha_i)(R \hat{\times} B)_i \tag{5.2}$$

This modifies the magnetic field line with the first order $R \times B$ drift. The path then approximates the guiding center of a particle that follows a magnetic field line and experiences an $R \times B$ drift in the correct direction and amount. Here, $\Delta\alpha_i$ denotes the partial curvature angle covered between two consecutive stepping points, which is the same as the angle between two consecutive B-field vectors in 3D. The drift direction is therefore given by

$$(R \hat{\times} B)_i = \left(\vec{B}_i \hat{\times} \vec{B_{i+1}}\right). \tag{5.3}$$

We show examplatory modified magnetic field lines (for different momenta and starting points in x and y) in Fig. 5.1 through NoMoS in the yz-plane. Note, that we also developed an algorithm to add the second order $R \times B$ drift, but the effect was too marginal to include in our investigations.

We don't see any significant difference between the field lines for different momenta (purple is overlapping all other colours) due to the perspective not showing the dominant drift direction. The most significant observation of this plot is the imperfect behaviour of the B-field lines' perpendicular component compared to

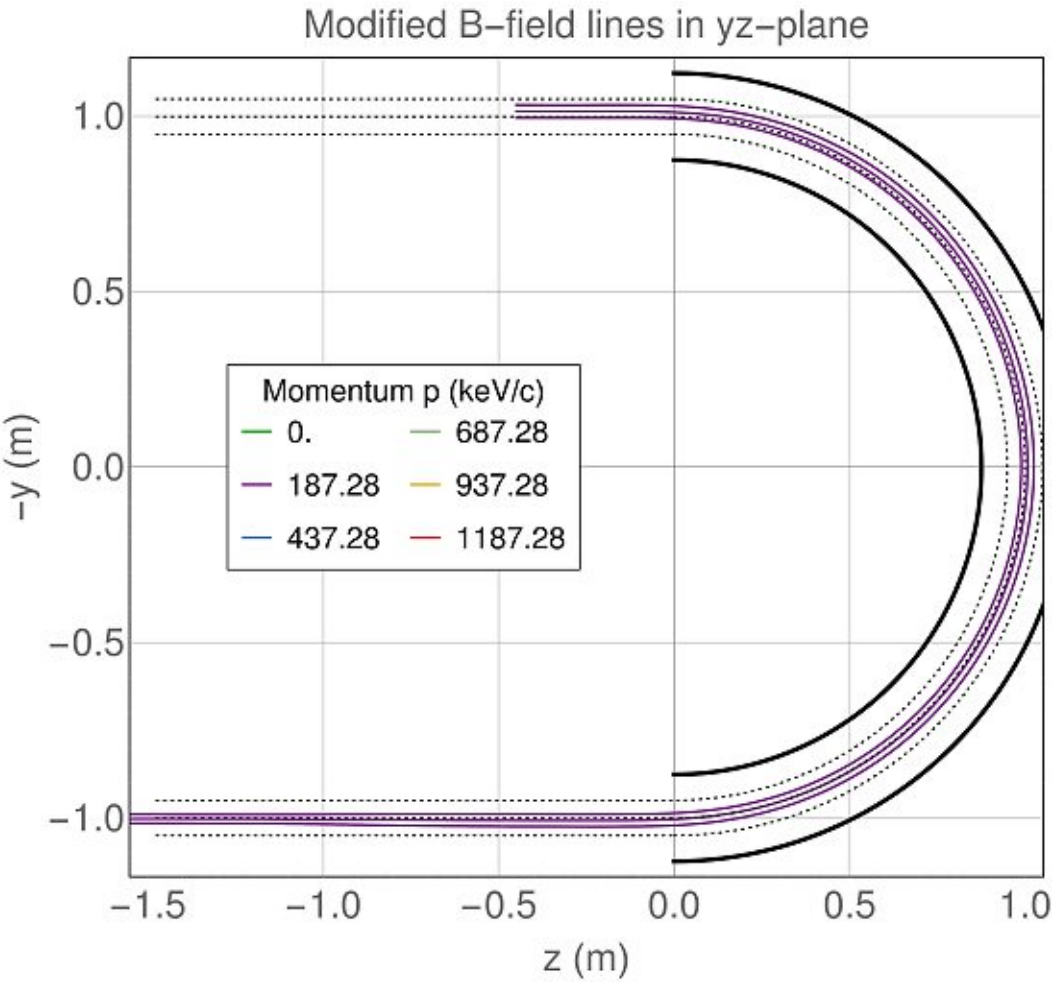

Figure 5.1.: Modified magnetic field lines for different momenta and a set of starting points (both in x and y) shown through NoMoS in the yz-plane. In dashed, we show the geometric central line as well as ± 5 cm around that. The thick black lines indicate a vacuum tube of a 350 mm diameter in the $R \times B$ region. Note, that only the purple lines are visible as all others overlap with it in this plot.

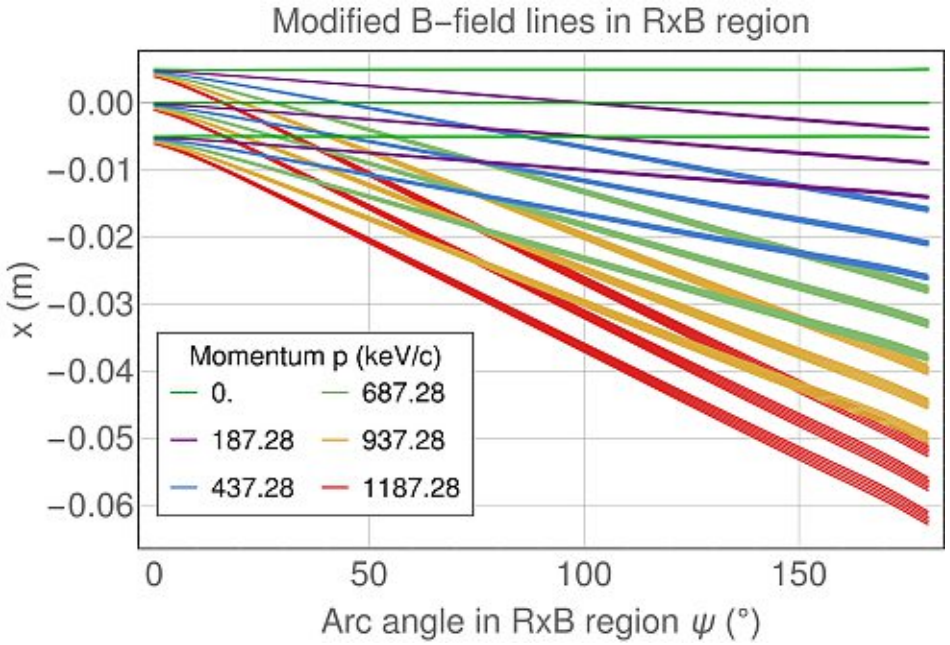

Figure 5.2.: Modified magnetic field lines for different momenta and a set of starting points (both in x and y) shown in the $R \times B$ region along the arc in x-direction. The $R \times B$ drift is applied continuously along the arc. Furthermore, lines that overlap at the beginning (lines with different y starting position), begin to spread out from each other. This is due to the radial magnetic field gradient, leading to different drifts for different y positions.

the geometric central line. This indicates the perpendicular motion of the central magnetic field line and will be discussed in more detail in Sec. 5.2.

Next, we show a more insightful perspective with the x-coordinate along the $R \times B$ region's arc in Fig. 5.2. It clearly shows the influence of the $R \times B$ drift on the field line linearly dependent on the momentum. As the curvature is gradually adding up linearly, also the drift in x-direction is linearly developing with the arc length.

Additionally, we see a separation into five separate lines per color, which indicates different drifts dependent on the starting point in y. This is expected due to the radial gradient in the $R \times B$ region.

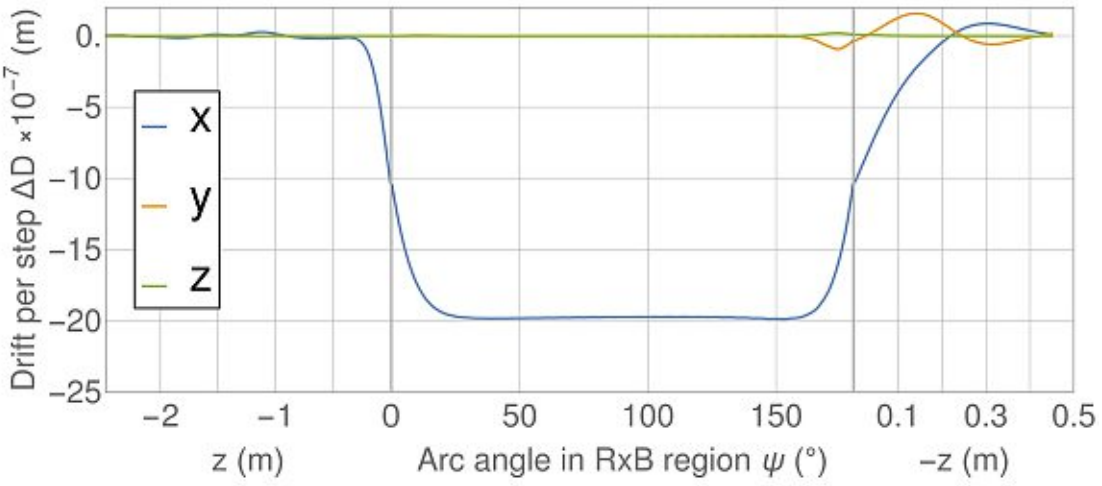

Figure 5.3.: The step-wise or incremental drift contribution per coordinate through NoMoS. This plot shows the main drift contribution in x as well as the secondary drift contributions in y and z. Note, that only every fifth step is given out from the algorithm to reduce the file size. Furthermore, the scale of this plot strongly depends on the step size of the magnetic field line.

Incremental Behaviour of the Modified Field Lines

A non-essential albeit interesting investigation is the incremental contribution to the $R \times B$ drift along a magnetic field line ΔD. It gives more insight into how the $R \times B$ drift is adding up and how the secondary drift directions are contributing to the motion. We show the incremental drift contribution per coordinate every fifth step of a magnetic field line (only every fifth step is stored) with maximum momentum p_{max} in Fig. 5.3.

We observe the main contribution in the x-coordinate with transitional zones at the entrance and exit of the $R \times B$ region. Also, in the detection region, there is a compensating contribution in positive direction due to the magnetic field lines forming a minor curvature in the other direction. The next biggest effect is in y (positive peak is roughly a tenth of the plateau in x). We expect a subordinate contribution in y at the end of the $R \times B$ region due to the fact that at that point, particles have drifted already in x (see outlook in Subsec. 7.1.2) and move into a more inhomogeneous area. Note, that the contribution varies in sign with compensating effect. The contribution in z is insignificantly small in comparison to the other contributions.

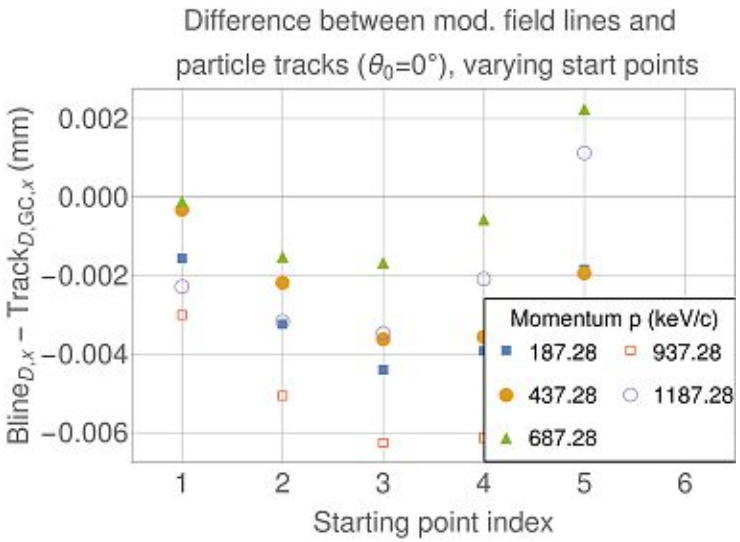

Figure 5.4.: The difference of the modified magnetic field lines and particle tracks' guiding centers at the detector in x for different starting points and momenta. The absolute difference is at or below 0.006 mm, showing exceptional agreement.

Validity of Modified Field Lines

The quality of the modified magnetic field lines has to be confirmed by comparing them with real particle tracks (simulated with the tracking software mentioned in Ch. 2). Figure 5.4 and 5.5 show the difference between modified magnetic field lines and particle tracks at the detector in the x and y-coordinate, respectively. Values are shown for different starting positions (represented with indices - representative points chosen) and different momenta.

On the one hand, we observe strong agreement between the modified field lines and simulated particle tracks in x-direction (the dominant drift direction) down to an accuracy below 0.01 mm. On the other hand, less agreement is seen in y-direction. There is a somewhat significant offset of ≈ -0.779 mm (average value) with minor momentum dependence ($\pm 4\%$ extremal relative variation) and no dependence on the incident angle θ_0. As the momentum dependence is low, we don't expect the first order $R \times B$ drift to be an explanation for the difference (even higher order drift terms are momentum dependent). A candidate for this effect might be a minor correction in the $R \times B$ drift in y due to imperfect forms of $\vec{R}$ and $\vec{B}$, that is

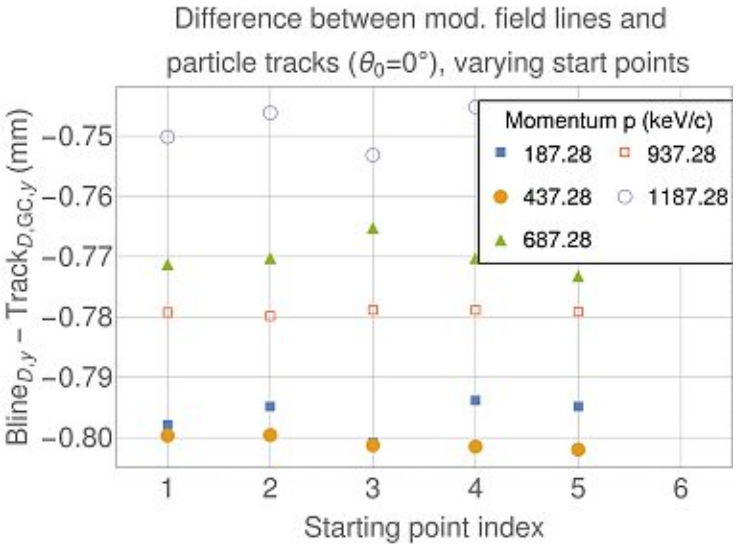

Figure 5.5.: The difference of the modified magnetic field lines and particle tracks' guiding centers at the detector in y for different starting points and momenta. The absolute difference is on the level of -0.779 mm (average value) with a variation of ± 0.025 mm.

not momentum dependent. For now, this offset can simply be incorporated into an additional shift ($y'_{R\times B,\mathrm{Shift}}$ and $y'_{\mathrm{D,Shift}}$). For further investigations, see the outlook chapter (Ch. 7).

5.1.2. (Monte Carlo) Particle Tracking

Undoubtedly, particle tracking is a powerful tool for systematic investigations, as it is the closest indication to how real particles would behave in our experiment. We simulate both hand-picked particle tracks and randomly selected particles (according to distributions - Monte Carlo). The former can directly be compared to the modified magnetic field lines, as can be seen in Subsec. 5.1.1, whereas Monte Carlo simulations give insight into average properties of a package of particles travelling through an experiment.

Full Monte Carlo Simulation

A full Monte Carlo Simulation in this work means, that we simulate a package of particles, whose properties follow particular distributions with weighted random values.

- Their energy follows the energy spectrum described in Subsec. 4.1.1
- Their incident pitch angle is isotropically distributed, according to $\sin\theta_{DV}$
- Their incident phase angle ϕ_{DV} is uniformly distributed ($\in [0, 2\pi]$)
- Their starting position is uniformly randomly diced, within a defined decay volume in x, y and z
- Note, that we don't include a neutron beam distribution

They are then tracked through the system. We not only store the final detector position but also some intermediate values. The stored quantities include the:

- Starting position $(x_{\mathrm{DV}}, y_{\mathrm{DV}}, z_{\mathrm{DV}})$
- Incident kinetic energy T_e, pitch and phase angle θ_{DV} and ϕ_{DV}
- Absolute magnetic field at the decay position B_{DV}

- Location of the maximum magnetic field $(x_\mathrm{F}, y_\mathrm{F}, z_\mathrm{F})$ as well as the absolute field strength B_F
- Position $(x_\mathrm{A}, y_\mathrm{A})$ at the aperture location $(z = z_\mathrm{A})$ as well as the local phase angle ϕ_A and the absolute magnetic field B_A
- Averaged absolute magnetic field strength within the $R \times B$ region $\bar{B}_{R\times B}$
- Detector position $(x_\mathrm{D}, y_\mathrm{D})$ at the detector location $(z = z_\mathrm{D})$
- phase angle ϕ_D, magnetic field B_D as well as pitch angle relative to the detector plane θ_D (not necessarily to the magnetic field) at the detector

Note, that we track many more particles than we analyse due to the fact, that we manually apply the aperture cut after the fact. This cut removes $\approx 90\%$ of electrons. We do this to be flexible in the aperture parameters.

Point Source

A point source is a chosen point in space as the decay position. Usually, also the incident kinetic energy and the pitch angle are fixed, while the incident phase angle is either diced uniformly or varied systematically. This is especially useful to investigate phase angle effects. For this, particles are emitted and tracked through the system while the phase angle at specific regions of interest is determined. Potential phase angle effects are discussed in the outlook (see Subsec. 7.2.2).

5.1.3. Mimicking Observable Deviation by Systematic Parameter Uncertainty

All systematic parameters going into the transfer function will have an inaccuracy dependent on the determination method (experimental or by simulation). These inaccuracies in general lead to an uncertainty in our fitted observables. There is an intricate method to investigate the sensitivity of the observables on such systematic parameters' inaccuracies, which is explained in the following.

Introducing Deviations in the Drift Distance Spectrum as a Fit Function

A deviation in a systematic parameter within a transfer spectrum is introduced, and the modified spectrum is used for a fit of a selected observable to a reference spectrum with no parameter variation. The amount of mimicked effect on the observable from the deviation introduced in the systematic parameter can be determined. The function, that needs to be minimized to perform the fit, is the sum of squared differences, the χ^2-function. An example of this function is shown with the Fierz term b as the observable and a variation in the systematic parameter p_1 in Equ. 5.4:

$$\begin{aligned}\chi^2(\Delta b)_{\Delta p_1} = \sum_{\text{bin}=1}^{N} & [G_{\text{Ref}}(\text{bin}, b=0, p_1, p_i, ..., p_n) \\ - & \; G_{\text{fit}}(\text{bin}, \Delta b, p_1 + \Delta p_1, p_i, ..., p_n)]^2\end{aligned} \tag{5.4}$$

with χ^2, dependent on the fit parameter Δb, the reference transfer spectrum G_{Ref} with the SM value of the Fierz term $b = 0$ and systematic parameters p_i, the modified transfer spectrum G_{fit} dependent on the fit parameter Δb and a parameter variation Δp_1. Note, that we didn't include any statistical uncertainty of the form $1/\sigma^2$ in Equ. 5.4, which is why all subsequent values will not be close to one.

In Fig. 5.6, we illustrate how the difference in the drift distance spectra materializes dependent on Δb. We construct linear interpolations of the reference drift distance spectrum as well as the modified spectra (in this example with $\Delta r_{\text{F}}/r_{\text{F}} = 1 \times 10^{-4}$ as the modified systematic parameter). We then evaluate the difference for $y = 0$ along the x-coordinate for different values of Δb in the modified spectrum, given by $G_{\text{Ref,Inter}}(x) - G_{\Delta r_{\text{F}},\text{Inter}}(\Delta b, x)$.

Manual Minimization of the χ^2-Function

We manually set up and minimize the function of squared differences χ^2. We do this on the one hand, because the computational intensity allows only a small amount of evaluated points for the observable and on the other hand to have better control over the fit parameter boundaries and optimization. The χ^2-function is manually minimized using a parable fit function

$$\chi^2_{\text{fit}}(\Delta b) = s(\Delta b - \Delta b_{\text{min}})^2 + o \tag{5.5}$$

We fit the scale s, the offset in the independent variable Δb_{min} (representing the mimicked effect) and the offset o. An examplary fit with a modification in the

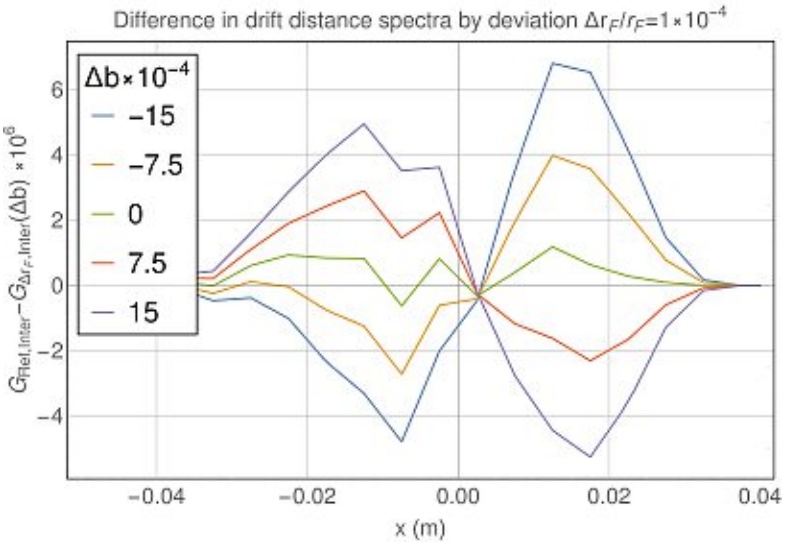

Figure 5.6.: Difference between interpolated reference drift distance spectrum and modified one by $\Delta r_\mathrm{F}/r_\mathrm{F} = 1 \times 10^{-4}$ for different values of Δb. Note, that the introduced modification induces a relatively small variation in the spectrum. As the difference reaches the limits of the numerical precision of the integral, the curves appear not very smooth. For larger modifications or more sensitive systematic parameters, the curve appears smoother.

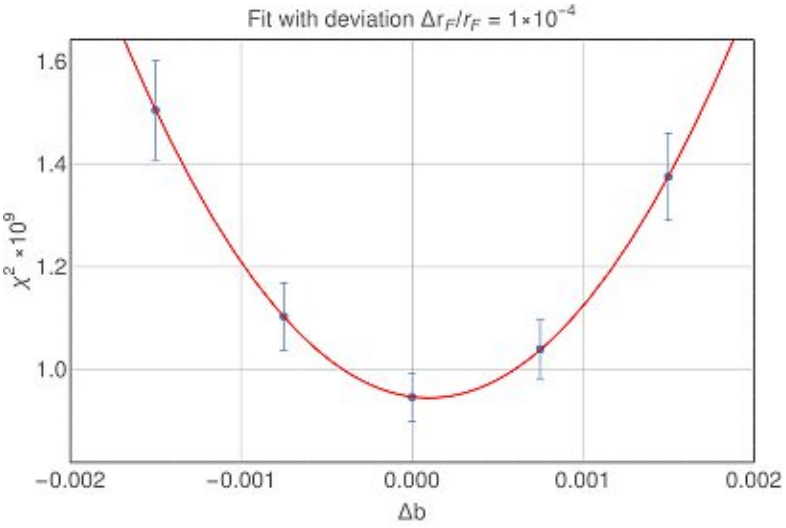

Figure 5.7.: A parable fit to the χ^2 distribution given for an introduced modification in the filter magnetic field ratio $\Delta r_\mathrm{F}/r_\mathrm{F} = 1 \times 10^{-4}$. The resulting fit parameter values are: $s = 2.19 \times 10^{-4}$, $\Delta b_\mathrm{min} = 0.9789 \times 10^{-4}$, $o = 9.45 \times 10^{-10}$. The errorbars shown are conservative error estimates from the numerical integration propagated to the χ^2-function.

systematic parameter of the filter magnetic field ratio r_F is shown in Fig. 5.7, with the fit results noted in the caption.

To be accurate in our analysis, we also perform a reference fit (fitting without an introduced deviation in a systematic parameter). This way, we obtain a fitted reference observable value b_0, whose accuracy is only restricted by the numerical and optimization errors. In the example of the Fierz term, we obtain $b_0 = 0$ within precision limit. If a deviation were to be obtained, the results from the sensitivity tests would have to be subtracted from the reference value. Note, that for Fig 5.7, five drift distance spectrum calculations are required in addition to the reference spectrum, in total taking eight days on a 16-core machine.

Scaling Factors as Sensitivity Parameters

As long as Δp is small enough, the mimicked effect Δb_min obtained by the fit behaves linearly with the value of Δp. With this linear assumption we introduce a systematic scaling factor k, as shown in Equ. 5.6.

$$\Delta b_{\min} = k\frac{\Delta p}{p} \longrightarrow k = \frac{\Delta b}{(\Delta p/p)} \tag{5.6}$$

This systematic scaling factor k is a measure of sensitivity. We calculate it with the transformed formula shown in Equ. 5.6. The advantage of this method is, that we can use realistic assumptions for the systematic parameter's uncertainty to calculate the prospective systematic uncertainty in b. With the obtained mimicked effect in the observable $\Delta b_{\min}$ of the example above (see Fig. 5.7), the systematic scaling factor calculates to $k_{r_\mathrm{F}} = 0.9689$. Now, we can make an estimation on the respective systematic uncertainty in b. Assuming and examplatory relative uncertainty in r_F of $\Delta r_\mathrm{F}/r_\mathrm{F} = 2 \times 10^{-4}$, we get

$$\Delta b_{r_\mathrm{F}} = k_{r_\mathrm{F}}\frac{\Delta r_\mathrm{F}}{r_\mathrm{F}} = 1.94 \times 10^{-4} \tag{5.7}$$

5.2. Determining Systematic Parameters

An accurate determination of the systematic parameters in NoMoS is of utmost importance to provide a high precision measurement of the observables. Due to the varying nature of the different systematic effects, multiple methods of determination are required. Some parameters are resolved using the modified magnetic field lines, others require systematic or Monte Carlo particle tracking (see previous section). We will also mention methods of experimental measurements of the systematic parameters, which are conducted during experiment runs in the last subsection.

5.2.1. With (Modified) Magnetic Field Lines

Many of the systematic effects connected to the magnetic field can be investigated with magnetic field lines. During an experimental run, a precise magnetic field map will be measured with experimental uncertainty in the measured field (absolute value and direction) as well as the positional uncertainty (find ideas for magnetic field measurements in Appendix C). This data is then compared to our magnetic field simulation, which is then fine-tuned to the data. The fitted simulation is subsequently used to calculate magnetic field lines.

The magnetic field lines' accuracy is on the one hand given by the simulations' accuracy as well as the accuracy of the stepping parameter s (the accuracy of the latter is only restricted by numerical errors). Interestingly, the inaccuracy of the magnetic field lines is not directly given by the positional uncertainty of the magnetic field map. Also, they are not influenced by a systematic offset in the absolute magnetic field measurement, because field lines are only defined by the direction of the B-field, not the overall scale. Tolerance investigations in the calculation of the field lines have to be conducted to fully illuminate their uncertainty. First estimations hint towards an inaccuracy lower than the inaccuracy of the field map positions (for now, we assume a precision of ± 0.1 mm). To confirm validity of the the magnetic field lines, they should be compatible with simulated particle tracks' guiding centres, which was shown in Subsec. 5.1.1.

Central Magnetic Field Line Shifts in Beam Prep. Area

To quantify the shift of the central magnetic field line at the regions of interest in NoMoS, we observe the central non-modified magnetic field line and its perpendicular movement through the system. Fig. 5.8 shows multiple magnetic field lines in the beam preparation area, starting in the decay volume with different starting positions in y. For the aperture value $y_{\mathrm{A,Shift}}$, we look at the central field line at the aperture position (vertical line at $z = -0.3$ m).

There are multiple features to be observed (filter and aperture location are marked with a green and orange line, respectively). The central line has a clear shift increasing towards the aperture and a turn towards the $R \times B$ region, initiating the curvature of the $R \times B$ region. The filter compacts all field lines around its location with also a minor impact on the central one, due to the increase of the magnetic field. The source of this shifting effect in general is the stray field from the $R \times B$ and detection regions.

Interpolating the central magnetic field line, we can evaluate the y coordinate at the aperture position ($z = -0.3$ m) and retrieve $y_{\mathrm{A,Shift}} = 7.188$ mm. The shift in x direction $x_{\mathrm{A,Shift}}$ is zero up to double-precision, due to the high homogeneity and symmetry in x.

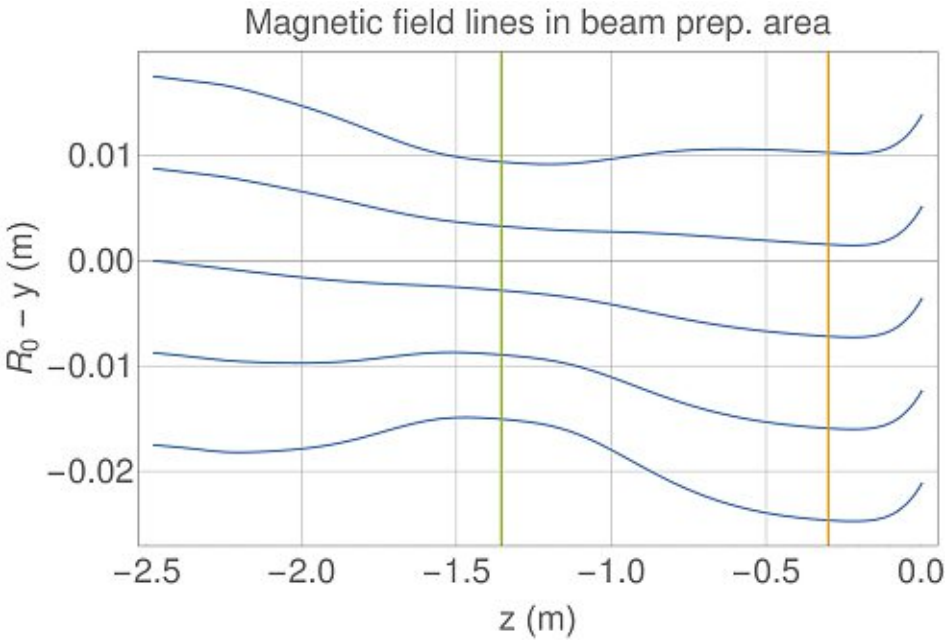

Figure 5.8.: Non-modified magnetic field lines through the beam preparation area along z for different starting points in y. We show the negative y coordinate subtracted from the central curvature radius R_0. In orange and green, the location of the aperture and filter are shown, respectively. Observing the central magnetic field line, there is a continuous shift in positive y direction, that is roughly 7 mm at the aperture.

Magnetic Field Profile in the $R \times B$ region

The most important region in NoMoS is of course the $R \times B$ region. A variety of systematic parameters are defined there. This includes the magnetic field defining parameters $B_{\mathrm{R\times B}}$, G_1 and G_2, as well as α and the central magnetic field line shift $y_{R\times B,\mathrm{Shift}}$ ($x_{R\times B,\mathrm{Shift}}$ doesn't enter our transfer description). Even though they all *can* be determined with magnetic field lines, the determination is not limited to it. Monte Carlo particle tracking as well as measurements of the experiment's magnetic field are strong tools to cross check and fine-tune results.

Figure 5.9 shows a multitude of aspects about the $R \times B$ region's magnetic field. Non-modified magnetic field lines are shown with their radial coordinate ($R_{yz} = \sqrt{y^2 + z^2}$) averaged over the $R \times B$ region. This value is then shown in the x-axis of the plot (minus the central curvature radius). One can see that the central data point (representing a central start in the decay volume) has an offset to zero, which displays $y_{R\times B,\mathrm{Shift}} = 6.77$ mm (we observe $x_{R\times B,\mathrm{Shift}} = 0$ mm).

In the y-axis of the plot, the magnetic field norm averaged over the $R \times B$ region is shown for the specific field lines in blue. We define the parameter $B_{\mathrm{R\times B}}$ as the respective value of the central magnetic field line with $B_{\mathrm{R\times B}}$= 219.679 mT (we will later see the good agreement with Monte Carlo simulations). Then, the data is fitted with the polynomial form of Equ. 4.9 to retrieve G_1 and G_2. Note, that we add the observed shift in y as an offset in the model, to centralize the central magnetic field line in the polynomial description. The coefficients turn out to be $G_1 = 0.9656$ and $G_2 = 0.9740$. Assuming a precision in the averaged magnetic field values of 5×10^{-4}, a fit with a significant amount of data points results in a precision of G_1 and G_2 on the 2×10^{-3} level.

Deeper Look into the Shifts in the $R \times B$ Region

Taking the average of the central field line's radial coordinate through the $R \times B$ region is only valid, if the radial length does not change too much, otherwise, the drift formula has to be adapted with another assumption for $\vec{R}$. Figure 5.10 shows magnetic field lines through the $R \times B$ region along the arc. We observe a slight increase over the arc for all lines as well as imperfections at the transition zones. This is due to the imperfect de-coupling of the magnetic field lines towards the $R \times B$ region's exits. Note that is is due to the magnetic field cross talk of the different areas. We expect that this can be reduced with magnetic shielding.

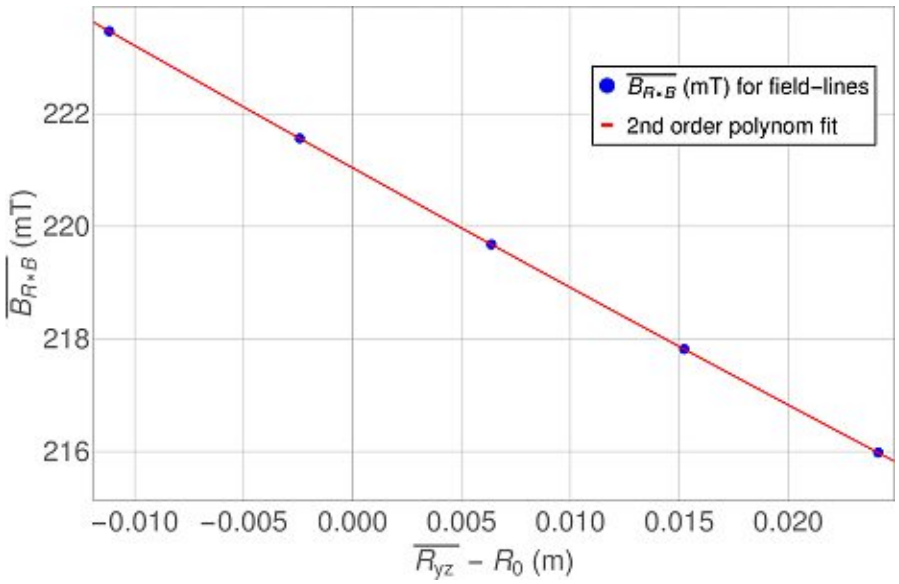

Figure 5.9.: Magnetic field lines with different starting points in y are followed and their mean curvature radius $\bar{R}_{\mathrm{yz}}$ in the $R \times B$ region is calculated. Then, the mean magnetic field norm $\bar{B}_{R\times B}$ is plotted dependent on $\bar{R}_{\mathrm{yz}} - R_0$. The red line indicates the polynomial fit to determine G_1 and G_2.

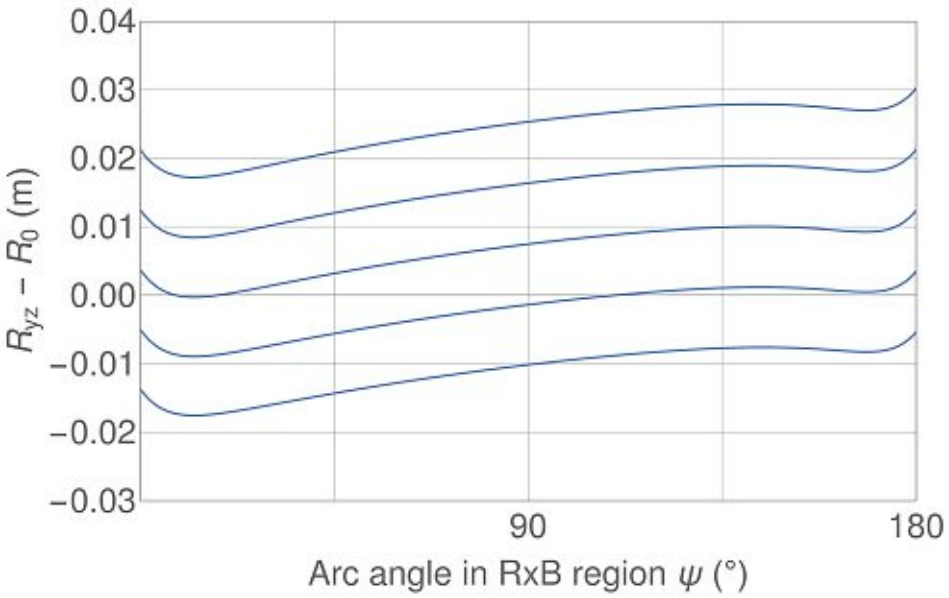

Figure 5.10.: Radial coordinate of magnetic field lines through the $R \times B$ region (along the arc angle ψ) minus the central curvature radius. We observe an increase over the arc as well as some intricacies at the transition zones.

Rough estimations have shown that the continuous change in the radial coordinate doesn't have to be considered in the short term goal in precision for NoMoS. Nonetheless, we recommend to include a systematic correction in the drift formula when striving for the ultimate precision goal.

Field Line Curvature

In Fig. 5.3, we have shown how the $R \times B$ drift is added up in increments along the $R \times B$ region's arc. The source of this is the behaviour of $\Delta\alpha$, the incremental curvature angle over the $R \times B$ region. This is shown in Fig. 5.11. It nicely illustrates the transition zones, where the curvature increases/decreases and a plateau with relatively constant behaviour. If a segment would have a different curvature center (concave versus convex), $\Delta\alpha$ would not show a different sign due to the calculation procedure. In Fig. 5.3 in the detection region, we observe a small contribution to the drift in the main direction x with opposite sign. Therefore, the last bump in Fig. 5.11 is a small contribution with opposite curvature center.

Investigations have shown that the specific form of $\Delta\alpha$ (related to $\vec{R}$) doesn't

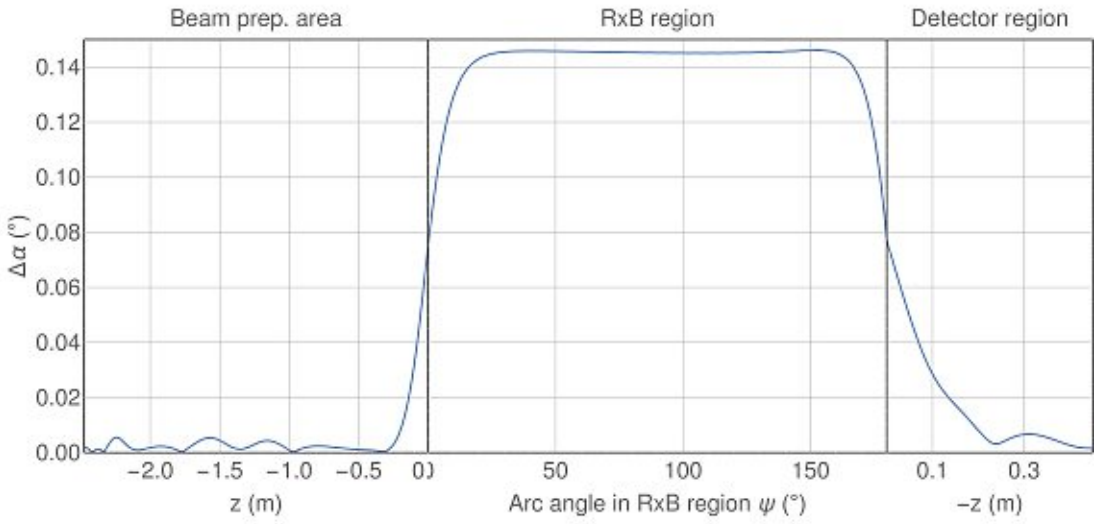

Figure 5.11.: The incremental curvature angle $\Delta\alpha$ along the path of a modified magnetic field line. There are transition zones bordering the $R \times B$ region with a plateau with constant curvature in the centre. In the beam preparation area, there are smaller bumps, that come from the filter, which curves the field lines. Furthermore, there is a small bump in the detection region due to the de-coupling from the $R \times B$ region. This curve can be summed over to determine the total curvature angle α.

change the total drift distance significantly. We constructed models with circle segments of different curvature and numerically integrated for the total drift. As long as the total curvature of the constructed circle segments equals α, no difference in the the drift was obtained. Nonetheless, for the ultimate precision goal, we recommend to further investigate different mathematical descriptions for the curvature to test possible corrections to α. For this work, we assume independence of the total curvature angle α on the incremental behaviour. Hence, considering the correct curvature direction, the total curvature angle is merely $\alpha = \sum_i \pm \mathrm{sgn}(\Delta D_{R\times B})\Delta\alpha_i$ (plus for protons, minus for electrons) with the sign function sgn(). For the normal conducting configuration, this results in $\alpha = 180.11°$. First tolerance tests indicate, that this parameter can be determined with an accuracy of 1×10^{-4}. To further consolidate the determination of this parameter, experimental tests can be conducted to further investigate it (see Sec. 5.5).

Central Magnetic Field Line Shifts in the Detection Region

In the detection region, we already expect a transitional effect comparable to the one in the beam preparation area. This is nicely illustrated in Fig. 5.12. Other than that, only a very minor effect towards the detector is observed, that tilts the field lines in $-y$ direction. This indicates the decrease in magnetic field leading to a spread of the field lines. Checking the central field line position at the detector, we get $x_{\mathrm{D,Shift}} = 0$ and $y_{\mathrm{D,Shift}} = 15.93$ mm.

5.2.2. With Systematic Particle Tracks

Tracking particles with specific settings helps us in multiple ways: it gives us a better insight into the particle behaviour in general or it can be used to cross check our previous investigations by comparing them with results from magnetic field lines. For this, we compare particles of different momenta with modified magnetic field lines or a particle with very low momentum with non-modified field lines. There is further insightful investigations, that will only be covered in the outlook regarding non-adiabatic effects and phase angle relations (see Subsec. 7.2.1 and 7.2.2).

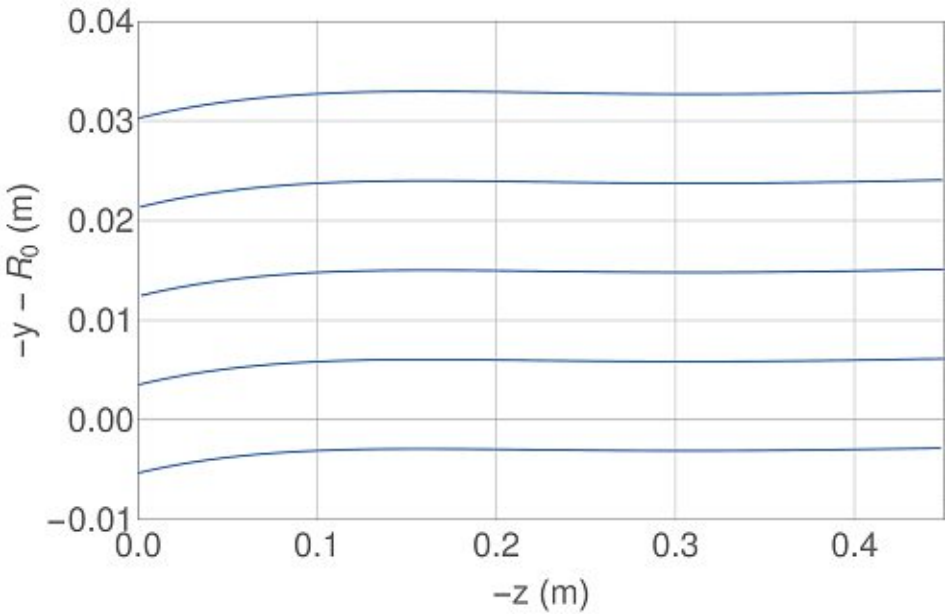

Figure 5.12.: Magnetic field lines in the detection region. We observe a shift of roughly $Y_{\mathrm{D,Shift}} = 1.5$ cm. There is also a small transitional effect at around $z = 0$.

Cross Checking the Shift in the Beam Preparation Area

For the central shift due to the movement of the central magnetic field line at the aperture, we obtain $y_{\mathrm{A,Shift,traj}} = 7.192$ mm from tracks with various momenta, a relative deviation from the value obtained by the magnetic field lines of $(y_{\mathrm{A,Shift}} - y_{\mathrm{A,Shift,traj}})/y_{\mathrm{A,Shift}} \approx 6 \times 10^{-4}$. There is no significant momentum dependence (maximum relative variation is below 6×10^{-5}). This shows the good quality of the magnetic field line estimations.

Cross Checking the Radial Coordinate in the $R \times B$ Region

The investigation procedure shown in Subsec. 5.2.1 illustrating the magnetic properties in the $R \times B$ region, can in principle also be conducted with particle tracks, with starting point guiding centers coinciding with the magnetic field lines' starting points. Nonetheless, there is an important caveat. We specifically used non-modified magnetic fields in the previous investigation, displaying the magnetic flux behaviour, not the particle's movement influenced by the $R \times B$ drift. Nonetheless, we don't expect significant drifts in the radial coordinate. In the following, we

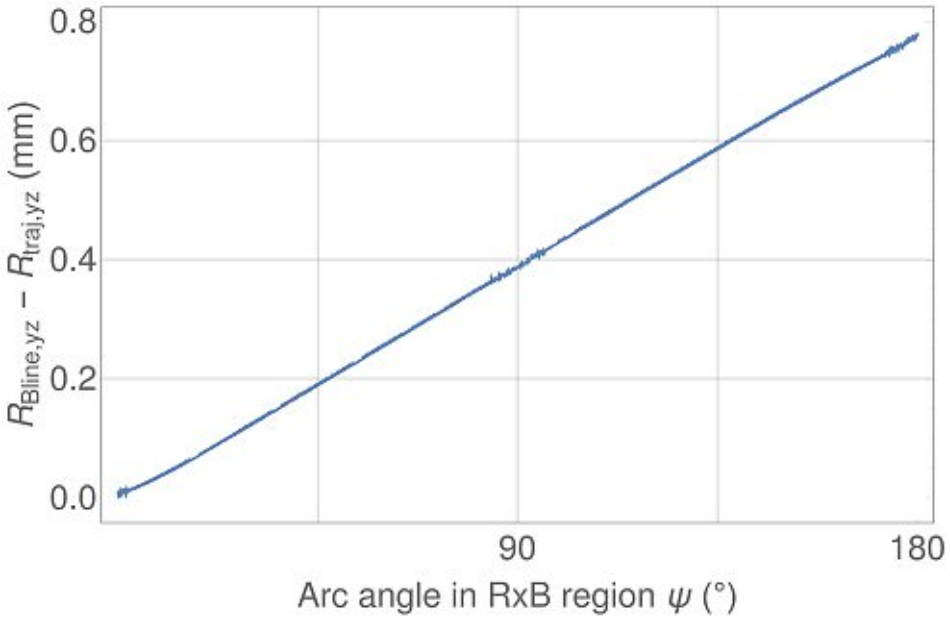

Figure 5.13.: The difference between the radial coordinate (in the yz-plane) of modified magnetic field lines and particle tracks for multiple momenta p through the $R \times B$ region. The lines for different momenta all overlap each other, therefore there is no momentum dependence. The maximum difference at the end of the $R \times B$ region is 0.778 mm. The minor jittering is due to interpolation artefacts.

compare particle tracks with modified magnetic field lines to test their overlapping features.

The cross check of the radial coordinate in the $R \times B$ region brings an interesting observation to light. In Fig. 5.13, we show the difference between the radial coordinate (in the yz-plane) of modified magnetic field lines and particle tracks for multiple momenta p through the $R \times B$ region. It is important to note, that in this figure, there is actually multiple lines representing different momenta, which all overlap each other. This means, that there is no momentum dependence in the difference. Nonetheless, we see a linearly increasing difference over the arc of the $R \times B$ region. The difference value at the end of the region is 0.778 mm, very similar to the difference between modified magnetic field lines and particle tracks at the detector shown before in Fig. 5.5.

A standard type of correctional drift in y due to more accurate assumptions about $\vec{R}$ and $\vec{B}$ usually leads to momentum dependence in the description. As the behaviour is more similar to a shift in the central magnetic field line, the effect can

be incorporated into a correction to them. As the deviation in the $R \times B$ region increases linearly, we apply a mean correction of $y'_{R\times B,\text{Shift}} = y_{R\times B,\text{Shift}} + 0.778/2$ mm and for the detector shift $y'_{\text{D,Shift}} = y_{\text{D,Shift}} + 0.779$ mm. For future investigations, we suggest further testing of modifications to the transfer as will be discussed in the Outlook, Sec. 7.1. At the detector position, Fig. 5.5 already summarizes the effect, with no significant variations through the detection region observed.

5.2.3. Full Monte Carlo Simulations

The advantage of Monte Carlo simulations is that we get a global picture of the particle behaviour with statistical significance. In the following, we analyse the parameters, mentioned in Subsec. 5.1.2. First, we look at the magnetic parameters of NoMoS and afterwards, we show detector related data, especially the spatial distribution of electrons on the detector. The decay volume is restricted in the perpendicular coordinates by the maximum area, for which electrons can pass the aperture and in the longitudinal coordinate by a length of 10 centimeter.

Determination of Magnetic Parameters

With Fig. 5.14 - 5.18, we summarize collected data from Monte Carlo simulations regarding the magnetic field properties in NoMoS (with $\approx 2.6 \times 10^6$ electrons at the detector). We look at the statistical distributions of the local magnetic fields (statistical errorbars not shown because they would be too small) as well as at possible kinetic energy dependencies (significant dependencies would have to be incorporated in a description of the transfer). In each figure, we determine important magnetic parameters, forming the average magnetic field strength and giving the absolute and relative standard deviation. Regarding possible energy dependencies, we give the relative maximum standard variation. Note, that we neglect statistical error bars in the default histograms because they would be too small in the figures.

We deduce various interesting results. The relative variation of the mean magnetic field strength in the respective zones is quite small ($\Delta B/B \leq 1.4 \times 10^{-4}$), with the only exception being the $R \times B$ region. Though, we clearly expect a significantly stronger variation than in the other regions of interest due to the radial field gradient. Interestingly, due to the near-linear behaviour of the gradient, the overall average magnetic field in the $R \times B$ region $B_{\text{R}\times\text{B}}$ varies only slightly from the value, determined from the central magnetic field line. The relative difference is

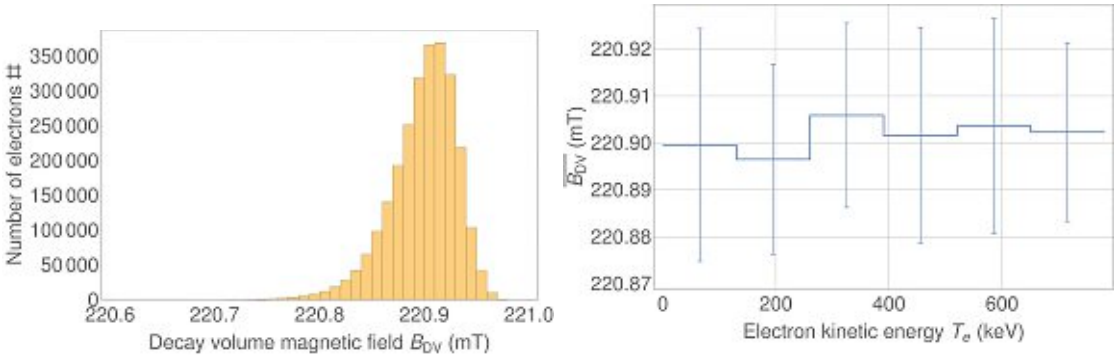

(a) A histogram of the absolute magnetic field strength in the decay volume per electron. The mean magnetic field is $\bar{B_{DV}} = 220.898$ mT, the standard deviation $\Delta B_{DV} = \pm 0.032$ mT or relatively, $\Delta B_{DV}/B_{DV} = \pm 1.4 \times 10^{-4}$.

(b) B_{DV} is binned in terms of energy to illustrate a possible kinetic energy dependence (error bars are standard variations for each bin). We observe no significant dependence with the maximum relative standard deviation $\Delta B_{DV,T}/B_{DV} = \pm 1.1 \times 10^{-4}$.

Figure 5.14.: Monte Carlo electron tracking results with $\approx 2.6 \times 10^6$ particles for the absolute magnetic field strength in the decay volume.

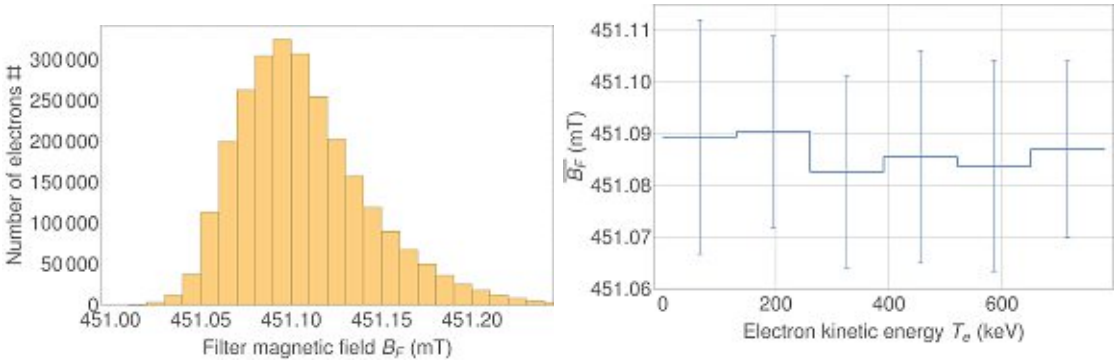

(a) A histogram of the absolute magnetic field strength at the filter per electron. The mean magnetic field is $\bar{B_F} = 451.106$ mT, the standard deviation $\Delta B_F = \pm 0.037$ mT or relatively, $\Delta B_F/B_F = \pm 8.1 \times 10^{-5}$.

(b) B_F is binned in terms of energy to illustrate a possible kinetic energy dependence (error bars are standard variations for each bin). We observe no significant dependence with the maximum relative standard deviation $\Delta B_{F,T}/B_F = \pm 5 \times 10^{-5}$.

Figure 5.15.: Monte Carlo electron tracking results with $\approx 2.6 \times 10^6$ particles for the absolute magnetic field strength at the filter position - the position at which the maximum magnetic field is reached.

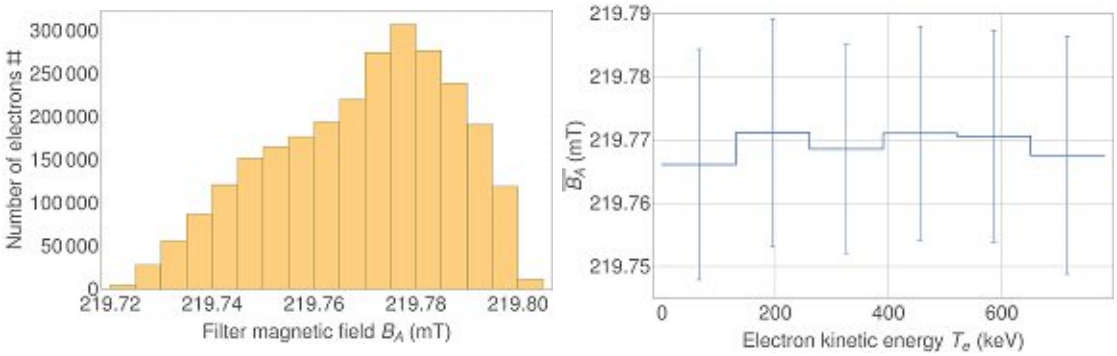

(a) A histogram of the absolute magnetic field strength at the aperture per electron. The mean magnetic field is $\bar{B_{\mathrm{A}}} = 219.769$ mT, the standard deviation $\Delta B_{\mathrm{A}} = \pm 0.018$ mT or relatively, $\Delta B_{\mathrm{A}}/B_{\mathrm{A}} = \pm 8 \times 10^{-5}$. No significant energy dependence present.

(b) B_{A} is binned in terms of energy to illustrate a possible kinetic energy dependence (error bars are standard variations for each bin). We observe no significant dependence with the maximum relative standard deviation $\Delta B_{\mathrm{A},T}/B_{\mathrm{A}} = \pm 8.7 \times 10^{-5}$.

Figure 5.16.: Monte Carlo electron tracking results with $\approx 2.6 \times 10^6$ particles for the absolute magnetic field strength at the aperture.

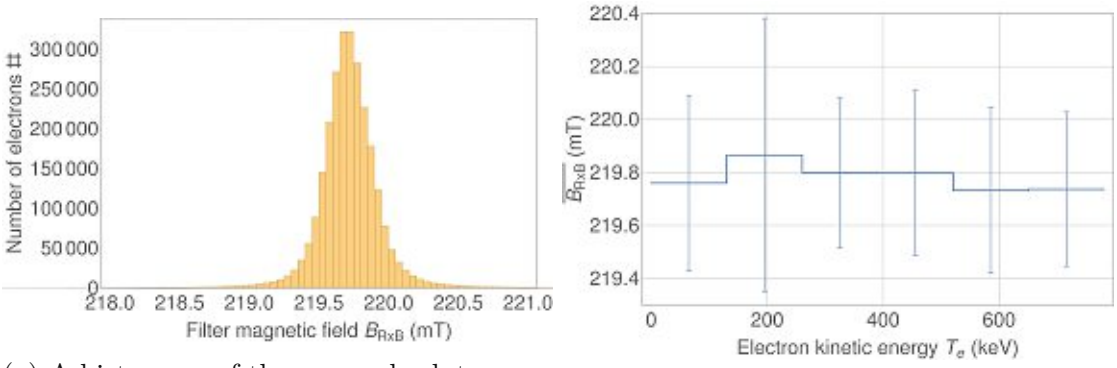

(a) A histogram of the mean absolute magnetic field strength in the $R \times B$ region per electron. The overall mean magnetic field is $\bar{B_{R\times B}} = 219.714$ mT, the standard deviation $\Delta B_{R\times B} = \pm 0.282$ mT or relatively, $\Delta B_{R\times B}/B_{R\times B} = \pm 1.29 \times 10^{-3}$.

(b) $B_{R\times B}$ is binned in terms of energy to illustrate a possible kinetic energy dependence (error bars are standard variations for each bin). We observe no significant dependence with the maximum relative standard deviation $\Delta B_{R\times B,T}/B_{R\times B} = \pm 2.3 \times 10^{-3}$.

Figure 5.17.: Monte Carlo electron tracking results with $\approx 2.6 \times 10^6$ particles for the absolute magnetic field strength in the $R \times B$ region.

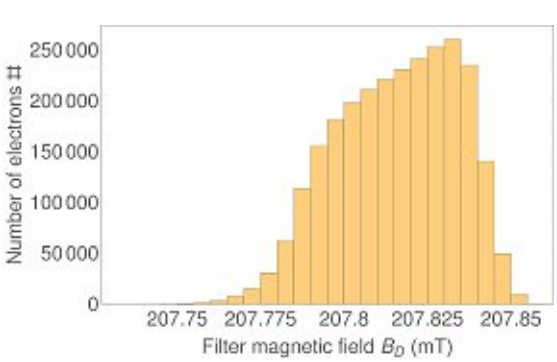

(a) A histogram of the absolute magnetic field strength at the detector per electron. The mean magnetic field is $\bar{B_{\mathrm{D}}} = 207.816$ mT, the standard deviation $\Delta B_{\mathrm{D}} = \pm 0.018$ mT or relatively, $\Delta B_{\mathrm{D}}/B_{\mathrm{D}} = \pm 8.7 \times 10^{-5}$.

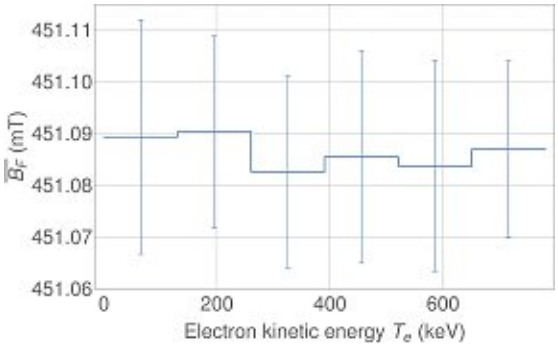

(b) B_{D} is binned in terms of energy to illustrate a possible kinetic energy dependence (error bars are standard variations for each bin). We observe no significant dependence with the maximum relative standard deviation $\Delta B_{\mathrm{D},T}/B_{\mathrm{D}} = \pm 8.5 \times 10^{-5}$.

Figure 5.18.: Monte Carlo electron tracking results with $\approx 2.6 \times 10^6$ particles for the absolute magnetic field strength at the detector.

$$\frac{B_{R\times B,\text{B-line}} - B_{R\times B,\text{MC}}}{B_{R\times B,\text{MC}}} = 1.6 \times 10^{-4} \tag{5.8}$$

Furthermore, there is no significant energy dependence in each region with variations being significantly lower than the respective standard deviation for each bin.

The magnetic parameters determined in the Monte Carlo simulations result in the following derived values for the systematic parameters in the normal conducting configuration:

$$r_{\mathrm{F}} = 2.0421,\ r_{\mathrm{A}} = 0.9949,\ r_{R\times B} = 0.9946,\ r_{\mathrm{D}} = 0.9408 \tag{5.9}$$

$$\frac{\Delta r_{\mathrm{F}}}{r_{\mathrm{F}}} = 1.62\times 10^{-4},\ \frac{\Delta r_{\mathrm{A}}}{r_{\mathrm{A}}} = 1.61\times 10^{-4},\ \frac{\Delta r_{R\times B}}{r_{R\times B}} = 1.29\times 10^{-3},\ \frac{\Delta r_{\mathrm{D}}}{r_{\mathrm{D}}} = 1.65\times 10^{-4} \tag{5.10}$$

Treatment of the Magnetic $R \times B$ Parameters

The relatively large variation of $r_{R\times B}$ (and $B_{R\times B}$) embodies the effect of the radial gradient. Due to simplicity, we haven't incorporated the radial gradient in the $r_{R\times B}$ parameter in our transfer description. The change in $R \times B$ drift due to the gradient's effect on the local pitch angle $\theta_{R\times B}$ (defined by $r_{R\times B}$) is at or below the 1×10^{-4} level (for angles up to $\theta_0 = 35°$, the effect is well below this level). This is a direct advantage of the relatively small θ-dependence of the $R \times B$ drift, discussed in Subsec. 3.1.1. Taking advantage of this, we define the ratio of magnetic fields $r_{R\times B}$ as well as the absolute magnetic field level $B_{R\times B}$ in the $R \times B$ region not by the Monte Carlo result and its standard deviation, but by the absolute magnetic field value from the magnetic field line investigation $B_{R\times B,\text{B-line}}$. Seeing the agreement between the Monte Carlo simulation and the field lines, we use the deviation between the two as a first estimate on the precision of the parameters (the error estimate of the absolute magnetic field level is not just given by the precision of the measurement probe - see discussion in Subsec. 5.2.1).

$$\frac{\Delta B_{R\times B}}{B_{R\times B}} = 1.6 \times 10^{-4}, \quad r_{R\times B} = 0.9946, \quad \frac{\Delta r_{R\times B}}{r_{R\times B}} = 2.13 \times 10^{-4} \tag{5.11}$$

Point of Reflection at Filter

As the maximum magnetic field at the filter location is not homogeneous, the specific point of maximum field can vary for each particle in all three coordinates. The distribution along z is normally distributed with a mean value of $\bar{z}_\text{F} = -1.356$ m with a standard deviation of $\sigma_{z_\text{F}} = 3.6$ mm.

Spatial Distribution at the Detector

One of the most important Monte Carlo simulation results is the particle distribution at the detector. The distribution in x is shown in Fig. 5.19. It also indicates the aperture opening with vertical red lines to illustrate the aperture being offset from the origin with $y_{\text{A,Offset}} = 0.03$ m (the adiabatically projected aperture opening at the detector only differs slightly).

Other perspectives, namely the histogram in y and the 2D histogram in x and y are shown in Fig. 5.20 and 5.21, respectively. The latter shows that for higher

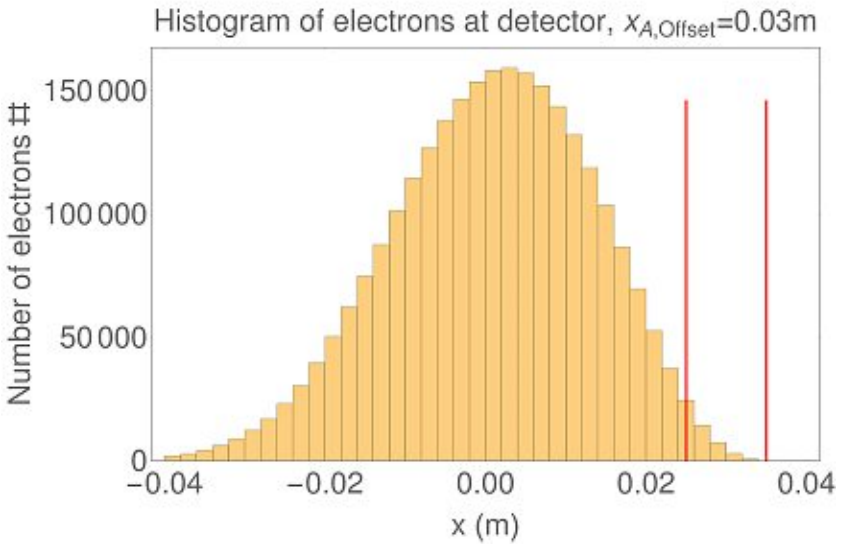

Figure 5.19.: A histogram of electrons hitting the detector binned in x. Electrons drift in negative direction. The approximate aperture opening in x is indicated with vertical red lines.

momenta (more negative x values), there is more spread in y due to larger gyration radii.

Pitch Angle at the Detector

We expect the pitch angle at the detector θ_D (or impact angle) to be smaller than the incident one, due to the fact that we obtained r_F to be smaller than 1. Furthermore, the detector plane in general is not perfectly perpendicular to the magnetic field direction, which is why there is a rotation involved. Figure 5.22 shows the difference between the incident pitch angle θ_0 and the impact angle. It shows an average difference of roughly 1°.

One can further investigate, what the residual difference in the pitch angle is, if the adiabatic change in pitch angle is considered. Figure 5.23 shows a 2D histogram with the following axes: First, we have the impact angle θ_D to show possible angle dependence. The second axis is the incident pitch angle, adiabatically transformed to the expected value at the detector $\theta_{D,Adia}$ minus the impact angle θ_D. The observed effect increases with the pitch angle and has two symmetric maxima in the difference. One might deduce, that this shows a non-adiabatic effect of the

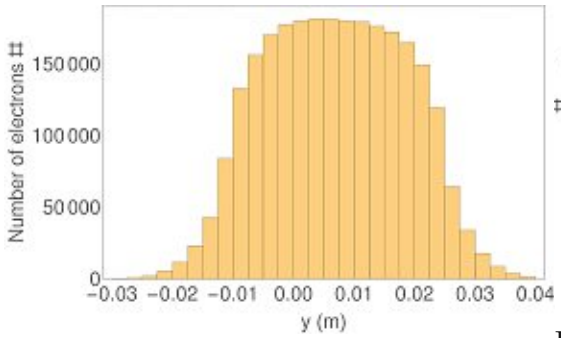

Figure 5.20.: A histogram of electrons hitting the detector binned in y. The mean of the histogram is $\bar{y}_{\mathrm{D}} = 0.007$ m.

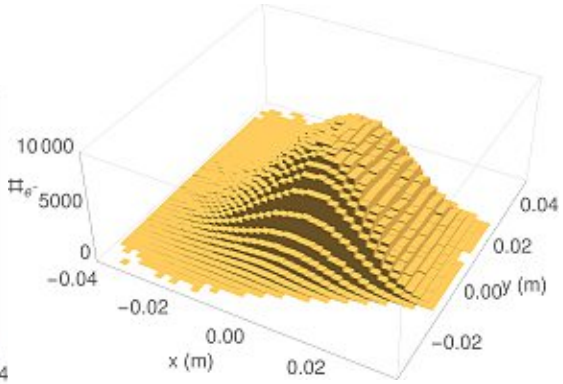

Figure 5.21.: A 2D histogram of electrons hitting the detector in x and y. For higher momenta (negative x), higher gyration radii are possible, which is why more spread in y is observed.

pitch angle, but we will show in the outlook (see Sec. 7.2.1) that this is not the case. Therefore, the residual behaviour we observe comes from the rotational transformation of the pitch angle.

5.2.4. Measurements during Experimental Runs

Some of the systematic effects can only be partly investigated by Monte Carlo simulations of the decay products' path through NoMoS. However, additional characterization measurements of the experimental set-up during experimental runs will be able to elucidate some of the systematic effects. Some of them are shortly discussed here.

Neutron Beam Profile

The neutron beam profile entering the experiment has to be both measured and simulated with neutron Monte Carlo simulations. Measurements of the beam profile are usually done with copper foils at multiple positions in the beam. The foils gets activated by the beam, which can subsequently be scanned for a 2D resolved beam profile. This can then be used as a fitting input for a Monte Carlo simulation

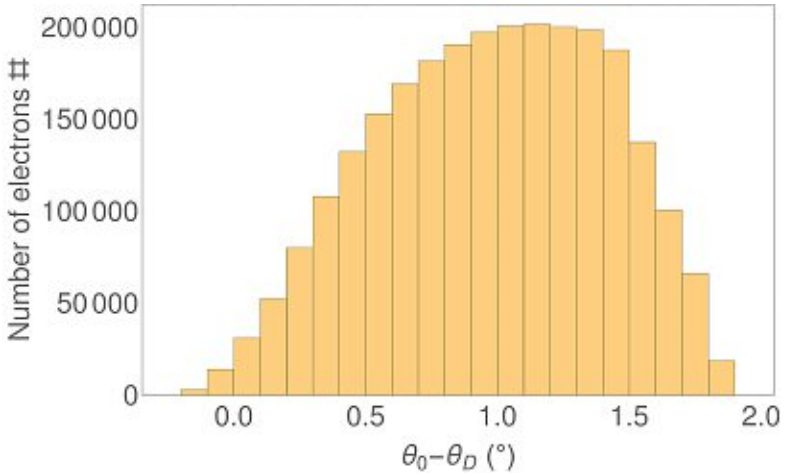

Figure 5.22.: A histogram of the difference between the incident pitch angle θ_0 and the impact angle θ_D. The mean deviation is roughly 1°.

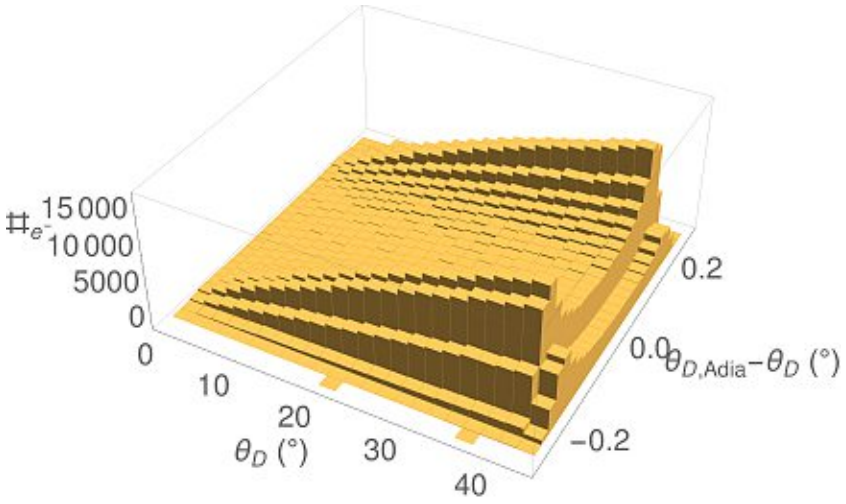

Figure 5.23.: A 2D histogram with the impact angle θ_D to show possible angle dependence and the incident pitch angle, adiabatically transformed to the expected value at the detector $\theta_{\mathrm{D,Adia}}$ minus the impact angle θ_D. We observe symmetric peaks at roughly ±0.2°.

of the neutron beam with all components of the neutron optics implemented.

For an estimation of our model neutron beam profile's (see Subsec. 4.1.2) parameter precision, we conducted a statistical analysis (for one dimension of the profile). Assuming a relative statistical error of 1% for each positional bin (2 mm binning chosen), we diced evaluated bin entries according to an appropriate normal distribution and refitted the profile. The statistical error of the fit parameters are given below:

$$\frac{\Delta w_{\mathrm{n}}}{w_{\mathrm{n}}} = 7.5 \times 10^{-4}, \quad \frac{\Delta p_{\mathrm{n}}}{p_{\mathrm{n}}} = 2.6 \times 10^{-3}, \quad \frac{\Delta k_1}{k_1} = 6 \times 10^{-3}, \quad \Delta k_2 = 1 \times 10^{-3} \tag{5.12}$$

Aperture Dimensions

In this work, we assume the aperture to be a 2D object. However, the following discussion holds also for a 3D aperture. The aperture's dimensions have to measured accurately before it is placed inside the experiment, with the most significant quantities being the respective lengths of the opening. After installation, the position relative to the central magnetic field line has to be determined using geometric reference points in the system and the measured magnetic field map. For the measurement of x_{AA},y_{AA},$x_{\mathrm{A,Offset}}$ and $y_{\mathrm{A,Offset}}$, we assume a precision of 0.2 mm, manageable with a caliper.

5.3. Interconnecting the Transfer Function with Monte Carlo Data

In this section, we compare the normed drift distance spectrum gained from Monte Carlo simulations ($\hat{\#}(x, y)$) with a calculated one from the transfer procedure ($\hat{G}(x, y)$) to investigate the quality of the latter. Figure 5.24 shows both kind of spectra with linear interpolation between bin points in separated plots (note, that we turned off the neutron beam in the transfer calculation to compare it to the Monte Carlo simulation in which no neutron beam profile was incorporated).

A more detailed perspective is given by plotting the difference of the two spectra, $\hat{\#}(x, y) - \hat{G}(x, y)$. This is shown in Fig. 5.25. There are two clearly distinct

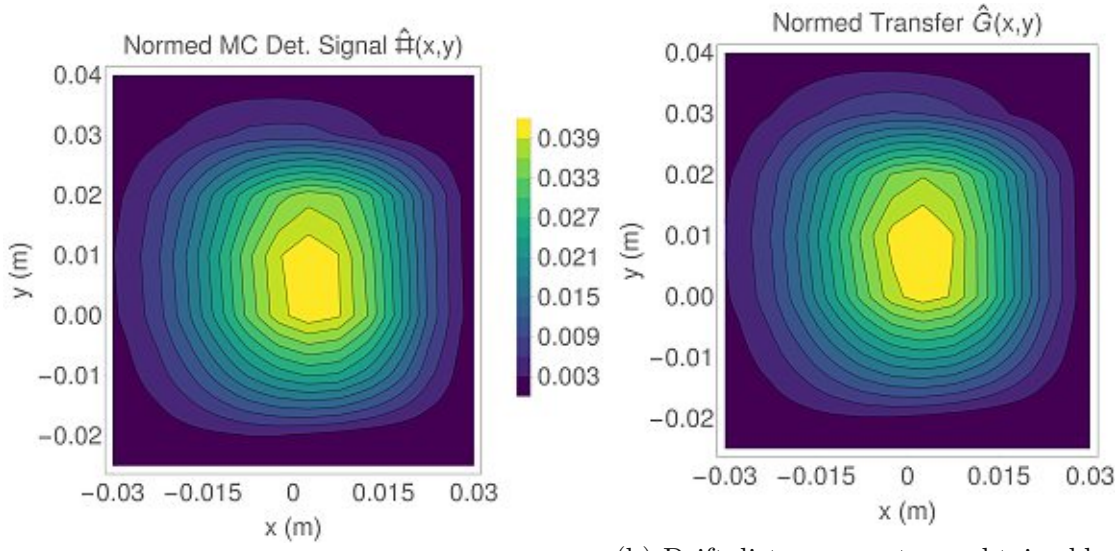

(a) Drift distance spectrum obtained by Monte Carlo simulations.

(b) Drift distance spectrum obtained by the transfer function calculation.

Figure 5.24.: Drift distance spectra obtained from (a) Monte Carlo simulations and (b) the transfer function calculation for the normal conducting configuration. Both spectra are normed to the sum of all entries. The bin points are linearly interpolated. The maximum entry value is ≈ 0.042. Both plots share the same color legend.

extrema facing each other with a more dominant asymmetry along the y axis. The maximum absolute variation is $\binom{+0.0028}{-0.0018}$ ($\binom{+6.6}{-4.3}$% relative to the drift distance spectrum's maximum).

This difference is clearly significant. To investigate, how well this discrepancy can be suppressed by a simple x and y shift, we minimize the deviation by shifting the transfer spectrum. We find, that a shift of $x_C = -0.5$ mm and $y_C = 0.65$ mm reduces the overall deviation significantly to $\binom{+0.0013}{-0.0012}$ ($\pm 3\%$ relative to the drift distance spectrum maximum), shown in Fig. 5.26.

This remaining deviation may seem a lot, but if we have a closer look at the comparison from a 1D perspective, we see that along the approximate central line ($y = 0$) - the statistically most significant region - promising agreement is observed. This is illustrated in Fig. 5.27.

A preliminary fit of the Fierz term to the Monte Carlo data using the transfer spectrum is in agreement with $b = 0$ within the statistical uncertainty of $\approx 5 \times 10^{-3}$.

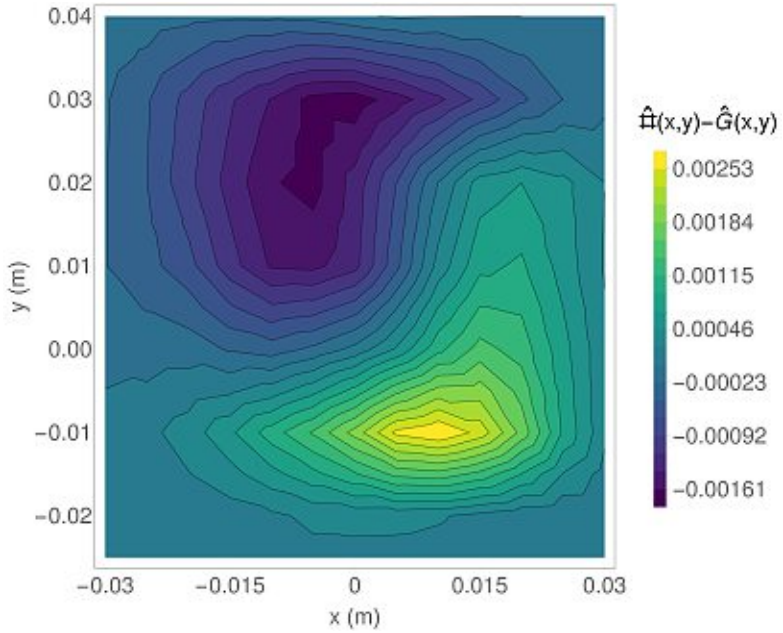

Figure 5.25.: The difference between the drift distance spectrum obtained by Monte Carlo simulations and the one by the transfer procedure, $\hat{\#}(x,y) - \hat{G}(x,y)$ using linear interpolation. The extremal variation is $\binom{+0.0028}{-0.0018}$.

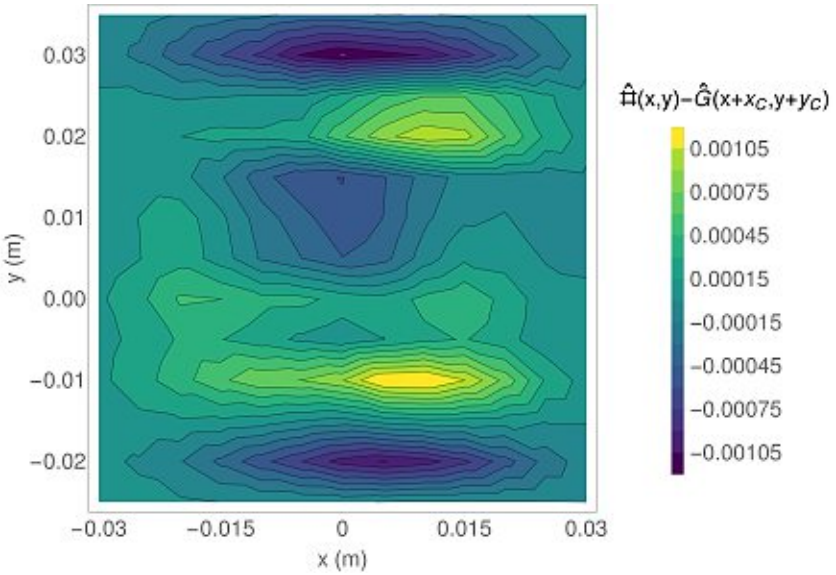

Figure 5.26.: The difference between the drift distance spectrum obtained by Monte Carlo simulations and the one by the transfer procedure, $\hat{\#}(x,y) - \hat{G}(x + x_C, y + y_C)$ with a shift of $x_C = -0.5$ mm and $y_C = 0.65$ mm. The extremal variation is $\binom{+0.0013}{-0.0012}$.

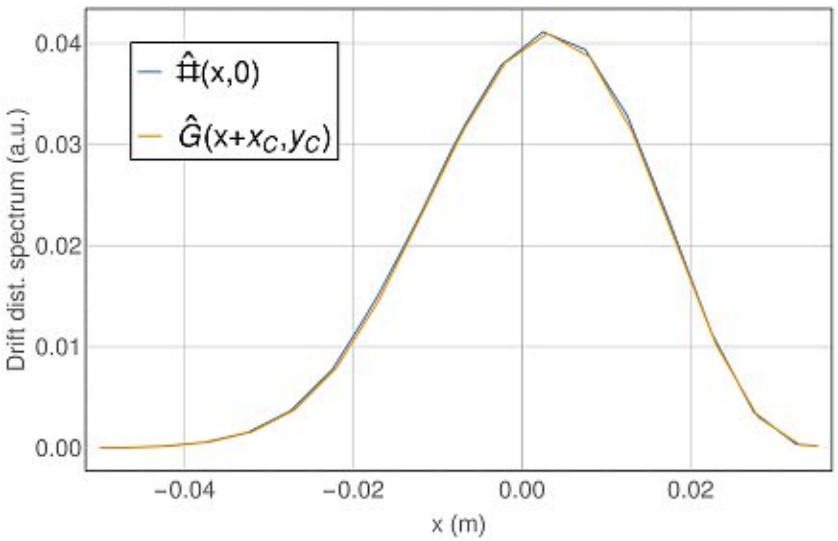

Figure 5.27.: The drift distance spectra obtained by Monte Carlo simulations $\hat{\#}(x,0)$ and the transfer calculation $\hat{G}(x, y_C)$ along x for $y = 0$. The spectra are linearly interpolated between bin center points.

Even though at the center of the drift distance spectrum in x and y, the relative statistical error for single bins is comparatively small ($\sqrt{\#_{\text{bin}}}/\#_{\text{bin}} = 0.2\%$), it goes up to 12% at the periphery of the spectrum (most outer non-zero bins). This result confirms that using the transfer procedure is a valid method of analysing data from the NoMoS experiment. Of course, further improvements (more precise transport and consideration of further minor systematic effects, especially in the periphery of the drift distance spectrum) are necessary to achieve ultimate precision in the data analysis. In future investigations, we also recommend to choose finer binning and higher statistics in the Monte Carlo simulations as well as to conduct further optimization of the transfer's numerical integration.

5.4. Systematic Parameter Sensitivities with the Transfer Function

This section is one of the most important ones in this work, as it summarizes the Fierz term's sensitivity on systematic effects' uncertainties. Assuming estimated uncertainties of the systematic parameters, systematic errors in b are given, using the sensitivity tests with the transfer function as a basis. This leads to an estimation on the total systematic uncertainty in NoMoS for measurements with electrons. This is discussed in Subsec. 5.4.1. Subsection 5.4.2 will shortly touch on the plethora of possible further investigations of changing sensitivities by varying systematic parameter values.

5.4.1. Collection of Systematic Effect Sensitivities

In this subsection, we present the resulting numbers from our systematic sensitivity investigations. We used the method, mentioned in Subsec. 5.1.3 to extract observable sensitivities on uncertainties in systematic parameters. In the following, we give the assumed relative uncertainty, the systematic scaling factor, and the derived systematic uncertainty in b for the respective parameter. We show the squared and linear sum for a lower and upper bound estimation, respectively. Nonetheless, the results are conservative as there is room for improvement, as shown in Subsec. 5.4.3. Sometimes, parameter uncertainties are given as absolute values, marked with * (for these, we define the systematic scaling factor as $\Delta b = k\Delta p$).

The numbers for the normal conducting standalone configuration of NoMoS are

given in Tab. 5.1, whereas the super-conducting ones are given in Tab. 5.2. Due to time restrictions, most sensitivity numbers for the super-conducting system (and some of the numbers for the normal-conducting one), are only rough estimates using simplified transfer algorithms or assuming numbers from the normal conducting sensitivity data (they are marked with †). We will show in Subsec. 5.4.2, that these estimates are valid to the extend of giving a first glimpse at the super-conducting systematic sensitivities.

Table 5.1.: Budget of the Fierz term uncertainty from systematic effect uncertainties for the NC configuration. For selected systematic effects, the absolute uncertainty is given - marked by *. Numbers marked with † use an approximate transfer.

Systematic effect	**Parameter**	**Rel. Inaccuracy ($\times 10^{-3}$)**	**Sensitivity (|k|)**	**Δb ($\times 10^{-3}$)**
Magnetic field				
Filter magnetic field ratio	r_{F}	0.162	0.979	0.16
Aperture magnetic field ratio	r_{A}	0.161	6.930	1.12
$R \times B$ magnetic field ratio	$r_{\mathrm{R\times B}}$	0.213	9.060	1.93
Magnetic field in $R \times B$ region	$B_{\mathrm{R\times B}}$	0.160	15.130	2.42
Radial gradient coefficients	G_1	2.000	0.863	1.73
	G_2	2.000	0.950	1.90
Curvature angle	α	0.100	18.840	1.88
Detector magnetic field ratio	r_{D}	0.165	2.130	0.35
Central field line movement	$x_{\mathrm{A,Shift}}$	0.100 mm*	12.975	1.30
	$y_{\mathrm{A,Shift}}$	0.100 mm*	0.016	1.60
	$y_{R\times B,\mathrm{Shift}}$	0.100 mm*	0.0004	0.04
	$x_{\mathrm{D,Shift}}$	0.100 mm*	0.009†	0.90
	$y_{\mathrm{D,Shift}}$	0.100 mm*	0.007†	0.70
Other				
Aperture dimensions	x_{AA}	0.200 mm*	1.600†	0.32
	y_{AA}	0.200 mm*	0.002†	0.40
	$x_{\mathrm{A,Offset}}$	0.200 mm*	11.400	2.28
	$y_{\mathrm{A,Offset}}$	0.200 mm*	0.002†	0.40
Neutron beam	$w_{n,x}$, $w_{n,y}$	0.750	0.100†	0.08
	$p_{n,x}$, $p_{n,y}$	2.600	0.200†	0.52
	$k_{x,1}$, $k_{y,1}$	6.000	0.100†	0.60
	$k_{x,2}$, $k_{y,2}$	1.000 *	0.975	0.98
Linear Sum				**21.61**
Squared Sum				**5.82**

Table 5.2.: Budget of the Fierz term uncertainty from systematic effect uncertainties for the SC configuration. For selected systematic effects, the absolute uncertainty is given - marked by *. Numbers marked with † use NC sensitivity numbers.

Systematic effect	**Parameter**	**Rel. Inaccuracy ($\times 10^{-3}$)**	**Sensitivity ($\lvert k \rvert$)**	**Δb ($\times 10^{-3}$)**
Magnetic field				
Filter magnetic field ratio	r_{F}	0.157	0.979†	0.15
Aperture magnetic field ratio	r_{A}	0.106	6.930†	0.74
$R \times B$ magnetic field ratio	$r_{\mathrm{R\times B}}$	0.150	9.060†	1.36
Magnetic field in $R \times B$ region	$B_{\mathrm{R\times B}}$	0.150	17.740	2.66
Radial gradient coefficients	G_1	2.000	0.863†	1.73
	G_2	2.000	0.950†	1.90
Curvature angle	α	0.100	18.840†	1.88
Detector magnetic field ratio	r_{D}	0.047	2.130†	0.10
Central field line movement	$x_{\mathrm{A,Shift}}$	0.100 mm*	12.975	1.30
	$y_{\mathrm{A,Shift}}$	0.100 mm*	0.016†	1.60
	$y_{R\times B,\mathrm{Shift}}$	0.100 mm*	0.0004†	0.04
	$x_{\mathrm{D,Shift}}$	0.100 mm*	0.009†	0.90
	$y_{\mathrm{D,Shift}}$	0.100 mm*	0.007†	0.70
Other				
Aperture dimensions	x_{AA}	0.200 mm*	1.600†	0.32
	y_{AA}	0.200 mm*	0.002†	0.40
	$x_{\mathrm{A,Offset}}$	0.200 mm*	11.400	2.28
	$y_{\mathrm{A,Offset}}$	0.200 mm*	0.002†	0.40
Neutron beam	$w_{n,x}$, $w_{n,y}$	0.750	0.100†	0.08
	$p_{n,x}$, $p_{n,y}$	2.600	0.200†	0.52
	$k_{x,1}$, $k_{y,1}$	6.000	0.100†	0.60
	$k_{x,2}$, $k_{y,2}$	1.000 *	0.975	0.98
Linear Sum				**20.64**
Squared Sum				**5.69**

5.4.2. Dependence of Sensitivities on Second Parameters

In general, the sensitivity of an observable on systematic parameters' uncertainties is dependent on the systematic parameters themselves. Each parameter co-defines the form of the drift distance spectrum, influencing the sensitivities. Due to limited computing power and time, investigations in this regard have been tightly restricted. We merely show a glance at the overabundance of possible tests. Figure 5.28 shows how the Fierz term sensitivity on the magnetic field in the $R \times B$ region $B_{\mathrm{R\times B}}$ is influenced by the value of $B_{\mathrm{R\times B}}$ itself.

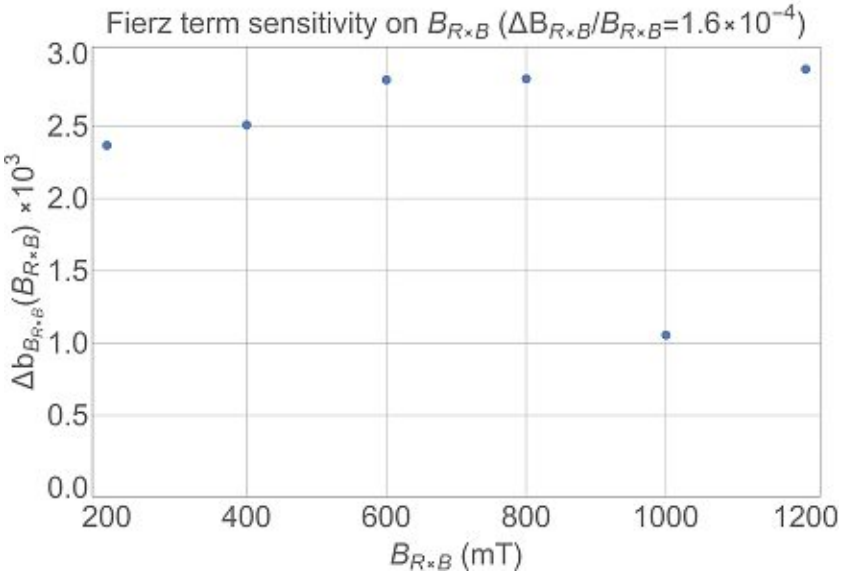

Figure 5.28.: The Fierz term's sensitivity due to uncertainties in the magnetic field in the $R\times B$ region, $B_{\mathrm{R\times B}}$ dependent on the value of $B_{\mathrm{R\times B}}$ itself. An approximate transfer was used for this investigation. The number of points is tightly restricted due to computation time. We assume an uncertainty of $\Delta B_{R\times B}/B_{R\times B} = 1.6 \times 10^{-4}$.

Figure 5.28 shows a significantly reduced sensitivity for a value of $B_{R\times B} = 1$ T (note, that an approximation of the transfer with more simplistic formulas and less accurate integration methods was used due to time restrictions). Keep in mind, that this plot might change significantly again, if other systematic parameters are changed as well.

The curvature angle α is the second most significant parameter in the error budget. It goes linearly into the $R \times B$ drift and can strongly change the drift distance

and therefore the form of the drift distance spectrum. For more details on this, see [M+20].

When NoMoS is not used as a standalone instrument, but toegether with a secondary facility like PERC, many of the magnetic parameters (and their respective uncertainties) change significantly, leading to different systematic sensitivities. Even though first estimations indicate a reduction of the magnetic parameters' sensitivities, others are increased. To give accurate numbers, more transfer spectra have to be calculated.

5.4.3. Additional Fit Parameters

The sensitivity results shown in Subsec. 5.4.1 assume the Fierz term b as the sole fit parameter for the minimization procedure. Nonetheless, we are capable of additionally fitting selected systematic parameters, reducing the overall systematic uncertainty of b. This method is only constrained by the numerical minimization procedure, computation time as well as potential correlation between fit parameters. Consequently, the uncertainty budget can not only be reduced by increasing the precision of the systematic parameters, but also by fitting them. Note, that this also implies a data point in the fit data representing the systematic parameter's determined value and error. This reduces the probability of correlated errors done in the procedure. Previous investigations with earlier versions of the transfer for the NC system indicate, that e.g. the uncertainty in b due to a deviation in $B_{\mathrm{R\times B}}$ can at least be reduced by a factor of 10, if $B_{\mathrm{R\times B}}$ is fitted in addition (confirmation runs with the latest transfer version couldn't be executed due to time constraints). This method can substantially improve the systematic budget.

5.5. Ideas for Testing Systematic Effects in the Experiment

In this section, we discuss the possibility of changing systematic parameters to test Monte Carlo simulations as well as the drift distance spectra obtained by the transfer function. This is a powerful tool to test the significance of the aforementioned methods as well as to improve systematic parameter determinations. Note, that every experimental change in the magnetic set-up requires a new magnetic field map for the determination of the magnetic parameters of the system.

5.5.1. Curvature Angle α

A parameter that has to be understood accurately is the curvature angle α. It is strongly connected to the way the magnetic field couples into the $R \times B$ region' curved geometry and subsequently out of it again. With the correction coils installed at the entrance and exit of this region and the coils in the detection region, the curvature angle can be modified and therefore be tested in the transfer function and Monte Carlo simulations. Special care has to be given to decoupling this change from effects on the central magnetic field line shifts.

5.5.2. Modifying Magnetic Field Ratios

Changing the magnetic field in the different regions influences the respective magnetic field ratios, which have significant effects on the transfer. For example, increasing the filter ratio reduces the amount of smearing effects due to gyration because the maximum gyration radius is smaller. The modifications can be applied by varying the power supply's current of selected coil blocks.

5.5.3. Changing the Aperture Opening

A modular design of the aperture is very attractive but complicated. It enables changing the beam opening on the fly, without the need of ventilating the system to exchange the aperture for another. Nevertheless, changing the aperture is a straight forward way to analyze and investigate its systematic effect of a measurement. One just needs to be careful to not lose too much signal while reducing the opening size.

6. Summary

The goal of this work was to present the NoMoS experiment. It utilizes a novel momentum spectrometer, called $R \times B$ spectrometer, which disperses particles according to their momentum. There is a plethora of motivations for such an experiment in neutron beta decay, discussed in Sec. 2.1. We can obtain the electron-anti-neutrino asymmetry parameter a or directly the ratio of vector and axial-vector couplings λ from the shape of the proton drift distance spectrum at our detector. With this, we can test the unitarity of the CKM matrix. Due to current tension in this regard (CKM unitarity, neutron lifetime etc.), more tests from different weak decays and systematically independent experiments have to be conducted. Moreover, analyzing the electron drift distance spectrum, we are capable of obtaining the Fierz interference term b, a non SM parameter, indicating additional couplings like scalar and tensor couplings, in the weak interaction (which was the focus of this work).

We thoroughly presented the measurement principle behind NoMoS, the $R \times B$ spectroscopy in Ch. 3, highlighting the advantages over conventional magnetic spectroscopy. We delved into a variety of design considerations defining the presented coil system. As NoMoS is feasible as a normal- and super-conducting version, we included explicit configurations for both conductor technologies.

Furthermore, we displayed a powerful tool for the systematic investigation of the NoMoS experiment, the transfer function, in Sec. 3.6. This mechanism incorporates an analytic description of the particle transfer through the system using adiabatic definitions as well as the $R \times B$ drift and numerically integrates over the available phase space. It can be utilized to estimate systematic uncertainties of the observables due to uncertainties in systematic parameters, which are the inputs for the transfer. Also, it can be used as a fit function to fit the observables to experimental or Monte Carlo data. We discussed the different ingredients of the transfer procedure like the edge effect of the aperture, the adiabatic particle movement or the $R \times B$ drift itself in Ch. 4.

The systematic parameters defining the analytic transfer in the transfer function have to be determined using several methods, shown in Sec. 5.1. We showcase

the underestimated power of magnetic field lines. They can be modified to bear an approximate $R \times B$ drift within them, which shows exceptional agreement with comparable particle tracks. Moreover, results from Monte Carlo data were presented, giving a more global insight into the collective particle behavior and determining many systematic parameters related to the magnetic field (see Sec. 5.2). As a quality check, we compared a drift distance spectrum obtained by Monte Carlo simulations with one calculated by the transfer procedure, which shows good agreement within statistical significance, presented in Sec. 5.3. Finally, we gave a systematic uncertainty budget for the Fierz term in Sec. 5.4, resulting in the following squared error sums for the NC and SC NoMoS configuration, respectively:

$$\Delta b_{\mathrm{NC,tot}} = 5.82 \times 10^{-3} \quad \Delta b_{\mathrm{SC,tot}} = 5.69 \times 10^{-3} \tag{6.1}$$

There is not a clearly better configuration in terms of the systematic uncertainty, especially because the SC configuration can reach the same magnetic fields as the NC one. Therefore, if long term usage is planned, we recommend the SC version due to the lower operation cost. Both presented uncertainty values are fully compatible with the first goal mentioned in the introduction of $\Delta b \lesssim 6 \times 10^{-3}$. To reach the ultimate goal stated as $\Delta b < 10^{-3}$, we suggest further investigations into additional fit parameters in the systematic sensitivity test (discussed in Subsec. 5.4.3 - this has the potential to significantly reduce single systematic effect uncertainties by at least a factor of 10), precision improvements in the determination of the systematic parameters as well as further analysis of corrections to the transfer description (examples are shown in the outlook, Ch. 7).

This work focussed on electrons, whereas protons will be discussed in later works (in progress [Kha21]). Protons have their own intricacies and special care has to be given to the fact that their low energy makes them predominantly sensitive to electric potentials (e.g. work function differences on the inner surface of the vacuum tube etc.). Also, they require post-acceleration to detectable energies, which usually introduces $E \times B$ effects, disturbing the drift distance spectra.

We gave a detailed and in-depth insight into the characterization of the magnet system of NoMoS. We realize that there are more pressing questions regarding this experiment that need answers (and hopefully they will be answered in the future). Nonetheless, we were able to shed light on many features and intricacies of this interesting experiment.

7. Outlook into Further Investigations

In this final chapter, we give an outlook into further investigations, suited for an even deeper look into the nature of the NoMoS experiment. First, we present modifications to the transfer from different effects in Sec. 7.1. Finally, we show interesting investigations done with particle tracking in Sec. 7.2.

7.1. Modifications to the Transfer

This section treats minor systematic effects, that influence the transfer only slightly and do not need to be considered for a first measurement, but might become important when reaching for ultimate precision with NoMoS.

7.1.1. Angular B-Field Gradient in the $R \times B$ Region

The magnetic field along the curvature of the $R \times B$ region should have a small decreasing gradient to prevent magnetic traps (see Fig. 3.3). Assuming a linear gradient and no change in the directional behaviour, a simple model can be constructed.

$$B_{R\times B} = B_{R\times B,0}\left(1 + B_1 - \frac{2B_1 t}{T}\right) \tag{7.1}$$

with the modified magnetic field strength behaviour in the $R \times B$ region $B_{R\times B}$, the reference field strength $B_{R\times B,0}$ and a correction factor B_1. The function is linearly dependent on t over the period T. This description is illustrated in Fig. 7.1. It shows the relative variation of the magnetic field strength in the $R \times B$ region over the relative time, indicating the functionality of B_1.

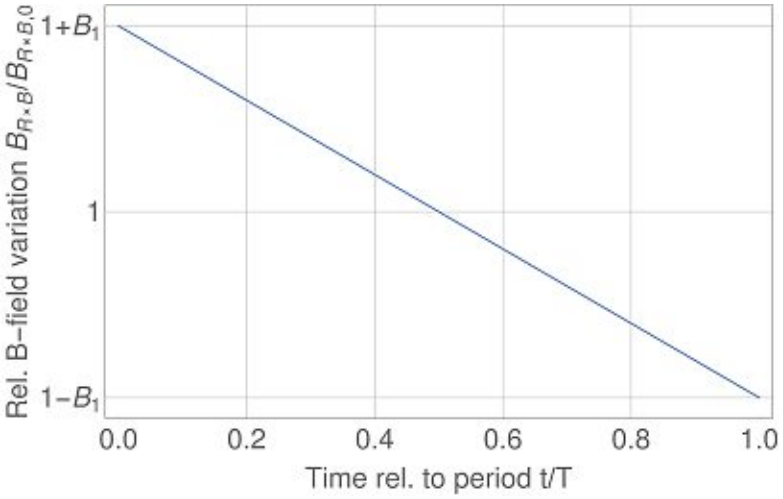

Figure 7.1.: A relative magnetic field gradient along the arc of the $R \times B$ region according to Equ. 7.1.

Proceeding with the calculation, we have to form the cross product, which only returns a non-zero component in x, shown in Equ. 7.2. The only time dependence comes from the B^2-term in the denominator.

$$\frac{\left(\vec{R} \times \vec{B}\right)_x}{R^2 B^2} = \frac{1}{B_0 R_0 \left(1 + B_1 - \frac{2B_1 t}{T}\right)} \tag{7.2}$$

Integrating over time yields a corrected drift

$$D^{\mathrm{1st}}_{x,\nabla_\phi} = D_0 \frac{\ln\left(\frac{1+B_1}{1-B_1}\right)}{2B_1} \tag{7.3}$$

For a 2% gradient along the $R \times B$ region, $B_1 = 0.01$ and therefore $\Delta D/D_0 = 3 \times 10^{-5}$. This scaling correction leads to an additional drift on the micrometer scale and is therefore omitted in our investigations.

7.1.2. Considering the first order drift movement in the curvature vector $\vec{R}$

A step towards a more realistic drift description is the consideration of a general first order $R \times B$ drift (here, depicted with D_0) as a change in the curvature vector

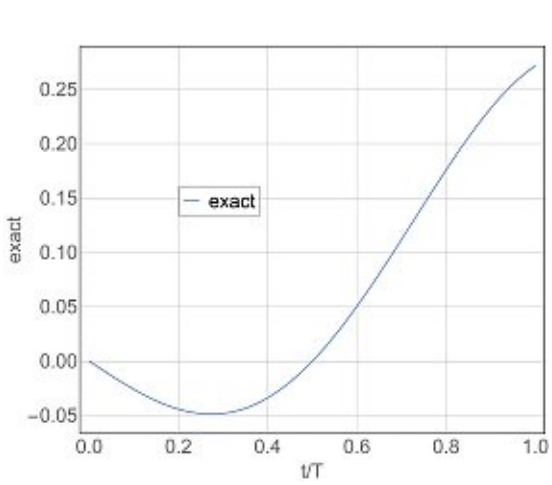

(a) The exact integrand of Equ. 7.5 (here called *exact*) dependent on t/T.

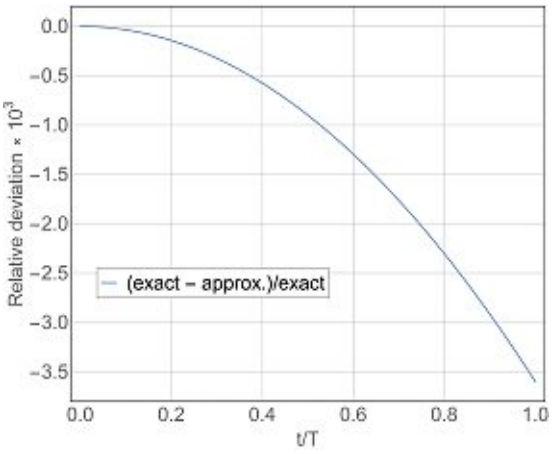

(b) The relative deviation between the exact integrand in Equ. 7.5 versus an approximation, omitting the t dependent denominator.

Figure 7.2.: Illustration of the integrand in Equ. 7.5 and a comparison with an approximation.

$\vec{R}$. For this, we construct a modified vector with an x-component, shown below

$$\vec{R} = \begin{pmatrix} \frac{D_0 t}{T R_0} \\ \cos(t\pi/T) \\ \sin(t\pi/T) \end{pmatrix} R_0 \tag{7.4}$$

The contribution in x describes a linear drift along the $R \times B$ arc dependent on t with the final value being $\vec{R}_x(t = T) = D_0$. With this adapted curvature vector, we expect contributions to the other axes in the drift vector. With $\vec{B}$ from Equ. 2.30, we inter alia get

$$\frac{\left(\vec{R} \times \vec{B}\right)_y}{R^2 B^2} = -\frac{\cos(t\pi/T) D_0 t}{B_0 T \left(R_0^2 + \frac{D_0^2 t^2}{T^2}\right)} \tag{7.5}$$

Unfortunately, this can't be integrated over time $t \in [0, T]$ symbolically. There are multiple possible approximations but the most promising one is illustrated in Fig. 7.2. It shows the exact integrand of Equ. 7.5 in comparison with an approximation, which neglects the t-dependent denominator term, enabling an exact symbolic integration.

Symbolically integrating the approximation, the drift in y forms to

$$D_y^{\mathrm{1st}} = 2\frac{D_0^2}{R_0^2\pi^2} \tag{7.6}$$

Here, we intentionally do not use D_0 according to Equ. 4.10 ($D_{x,\nabla}^{\mathrm{1st}}$) but the simpler version in Equ. 2.32 (D_x^{1st}). This is due to the fact that the drift formula with the radial B-field gradient depends on $y_{R\times B,\mathrm{GC}}$, which would lead to a recursive coupling in the δ_y-function of the transfer function. We have not found any solution resolving the transfer equations using the more complex drift formula. Inserting examplatory numbers, $D_0 = 0.06$ m and $R_0 = 1$ m, we obtain

$$D_y^{\mathrm{1st}} = 0.7 \text{ mm}, \quad \frac{D_y^{\mathrm{1st}}}{D_0} = 1.2\,\% \tag{7.7}$$

This entices to be interpreted as the explanation for the effect observed in our investigations of the magnetic field lines and particle tracks for the central magnetic field line shifts (Subsec. 5.2.1). Unfortunately, the presented result is quadratically momentum dependent ($D_0 = D_0(p)$). For only the largest momenta will this effect be somewhat significant (sub-millimeter). We decided against using this description in our transfer also because it strongly couples the two transfer coordinates, leading to unreasonably increased computation times (solved equations in the integrand get significantly more complex).

7.1.3. Earth Magnetic Field

The earth magnetic field or a general background field might influence the simulated behaviour of the magnetic field. Furthermore, it would be included in the measured magnetic field map. A general low magnetic field background can be incorporated in a modified $R \times B$ drift.

A general offset in the magnetic field is described as

$$\vec{B}_{\mathrm{wE}} = \vec{B}_0 + \vec{B}_{\mathrm{E}} = \begin{pmatrix} B_{\mathrm{E},x} \\ -B_0 \sin(t\pi/T) + B_{\mathrm{E},y} \\ B_0 \cos(t\pi/T) + B_{\mathrm{E},z} \end{pmatrix} \tag{7.8}$$

showing the modified magnetic field vector $\vec{B}_{\mathrm{wE}}$ and its three components. Constructing the cross product, we obtain contributions in all three coordinates. In the following, we focus on the corrective effect in the drift in x.

$$\frac{\left(\vec{R}\times\vec{B}_{\mathrm{wE}}\right)_x}{R_0^2B_0^2}=\frac{B_0+B_{\mathrm{E},z}\cos(t\pi/T)-B_{\mathrm{E},y}\sin(t\pi/T)}{R_0B_0^2} \tag{7.9}$$

Again, to produce an integrand that can be integrated symbolically, we omitted the effect on the norm B^2 in the denominator. We therefore assumed that $\vec{B}^2_{\mathrm{wE}}\approx\vec{B}^2_0$ (well-founded if background field is a factor 10^{-4} lower than the main field), which leaves us with

$$D_{\mathrm{E},x}=D_0\left(1-\frac{2B_{\mathrm{E},y}}{B_0\pi}\right) \tag{7.10}$$

or relative to the reference $R\times B$ drift in x

$$\frac{\Delta D}{D}=-\frac{2B_{\mathrm{E},y}}{B_0\pi} \tag{7.11}$$

Putting in examplatory numbers ($B_{\mathrm{E},y}=10^{-5}$ T, $B_0=0.22$ T), we obtain an effect on the 10^{-5} level relative to the reference drift, which is way below resolvable differences. Interestingly, this correction functions as a constant offset in contrast to other corrections calculated so far. For the other components, the results are similar. Below, we show the y component of the drift

$$D_{\mathrm{E},y}=D_0\frac{2B_{\mathrm{E},x}}{B_0\pi} \tag{7.12}$$

This is a scaling effect on the reference drift with roughly the same insignificant effect as the correction in x.

The effect of a general background field can be tested rigorously. By flipping the direction of the magnetic field created by the coils, the default drift is in opposite direction. Nonetheless, the background magnetic field stays the same, which can be used to separate the drift effects. Furthermore, positrons from a source can be used to flip the drift utilizing the opposite charge compared to electrons.

7.1.4. Magnetic Field Inhomogeneities

Even though the sensitivity of the Fierz term on the uncertainty in the magnetic field ratios is not the most dominant, to achieve higher accuracy, the variation of the magnetic field across the beam cross section in the different regions of interest could be considered. An examplatory modification to the transfer might look like the following:

$$r_{\mathrm{F},\nabla}=r_{\mathrm{F},0}(1+s_1x^2_{\mathrm{F,GC}}+s_2y^2_{\mathrm{F,GC}}) \tag{7.13}$$

with the modified magnetic field ratio at the filter $r_{\mathrm{F},\nabla}$, the reference value at the central position $r_{\mathrm{F},0}$, two systematic coefficients s_1 and s_2, as well as the particle guiding center position $(x_{\mathrm{F,GC}},y_{\mathrm{F,GC}})$. This highlights an additional coupling between the two coordinates in the transfer function. Special care has to be paid to succeed in solving the transfer function with strongly coupled equations.

Preliminary tests show relatively insignificant sensitivity of b on gradient scaling factors ($\Delta b \lesssim 1\times10^{-4}$). Note, that introducing further systematic parameters also has downsides due to the uncertainty in the parameter determination method.

7.2. Investigations with Particle Tracking

In this section, we show some interesting investigations with particle tracking, that have not been incorporated in our transfer but that may play a role in future analysis, especially when ultimate precision is sought.

7.2.1. Non-Adiabatic Pitch Angle Increase in the $R \times B$ Region

In the adiabatic motion of an electron, the local pitch angle behaves according to Equ. 2.20. To check this relation, a simulated particle track can be investigated. The exact local pitch angle of a particle is given by

$$\cos\theta_{\mathrm{traj}} = \frac{\vec{v}\vec{B}}{|\vec{v}||\vec{B}|} \tag{7.14}$$

With this, local non-adiabatic behaviour can be discovered by the difference

$$\Delta\theta = \theta_{\mathrm{traj}} - \theta_{\mathrm{adiab}} \tag{7.15}$$

Figure 7.3 shows $\Delta\theta$ through a normal-conducting NoMoS set-up for different electron trajectory starting points. The figure clearly indicates a local non-adiabatic effect in θ in the $R\times B$ region of roughly up to $\pm1°$ ($p = p_{\mathrm{max}}$, $\theta_0 = 40°$, $\phi_0 = 0°$). There is an oscillatory effect with an increasing envelope at the entrance of the $R\times B$ region, a somewhat constant envelope in the region itself and then a decreasing one at the exit.

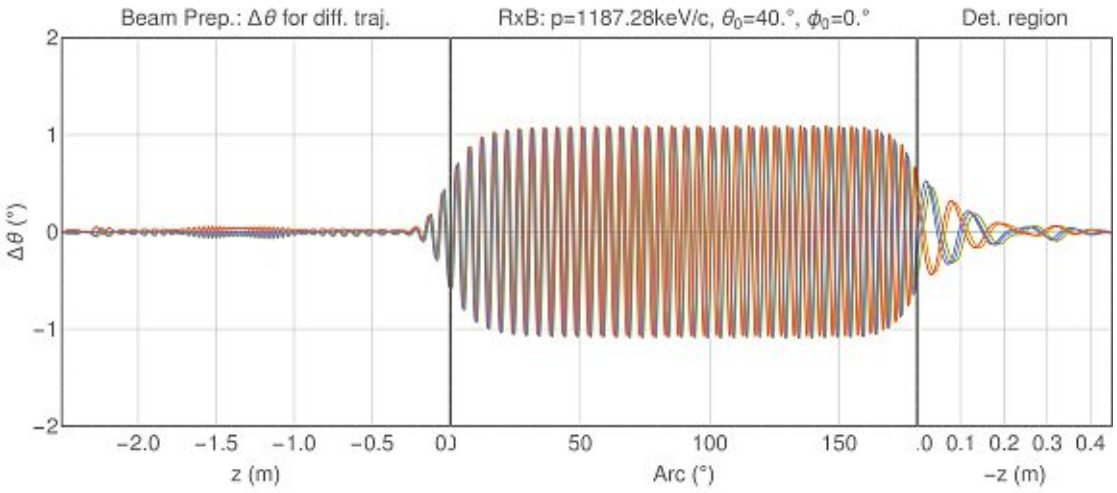

Figure 7.3.: The non-adiabatic quantity $\Delta\theta$ plotted for particle tracks of different starting points (different colors) with $p = p_{\max}$ and $\theta_0 = 40°$ through NoMoS in the single regions. There is an oscillatory effect in the $R \times B$ region.

The height of the envelope's plateau depends on the particle's momentum, as shown in Fig. 7.4. The dependency appears to be linear. There is no significant position, θ or ϕ dependence. The only intricacy we find is the change in behaviour for incident angles $\theta_0 < \Delta\theta_{\max}(p)$, when the incident pitch angle is smaller than the expected oscillation maximum from the linear model. In this case, $\Delta\theta$ follows the envelope without oscillation. An example is shown in Fig. 7.5.

The oscillatory behaviour in Fig. 7.3 and 7.5 is correlated with the gyration of the particle. This can be highlighted showing $\Delta\theta$ dependent on the local radial coordinate in the $R \times B$ region, illustrated in Fig. 7.6. Figure 7.6 nicely highlights that the maximum of non-adiabatic $\Delta\theta$ is always on the inner side of the gyration through the $R \times B$ arc whereas the minimum is on the outside.

This correlation hints towards a possible explanation for the non-adiabatic effect. During the gyration of a particle through the $R \times B$ region, the radial gradient varies the experienced local magnetic field by up to $\approx 3\%$. With this, the adiabatic condition $\Delta B/B << 1$ is not sufficiently met anymore. Interestingly, we can link this effect to the curvature of the magnetic field. $\Delta\alpha$, introduced in Subsec. 5.2.1, is a direct indicator for the curvature and the amount of curvature defines the size of the radial gradient. The form of the curve shown in Fig. 5.11 resembles the envelope of the non-adiabatic behaviour. As a matter of fact, a scaled $\Delta\alpha$ plot can

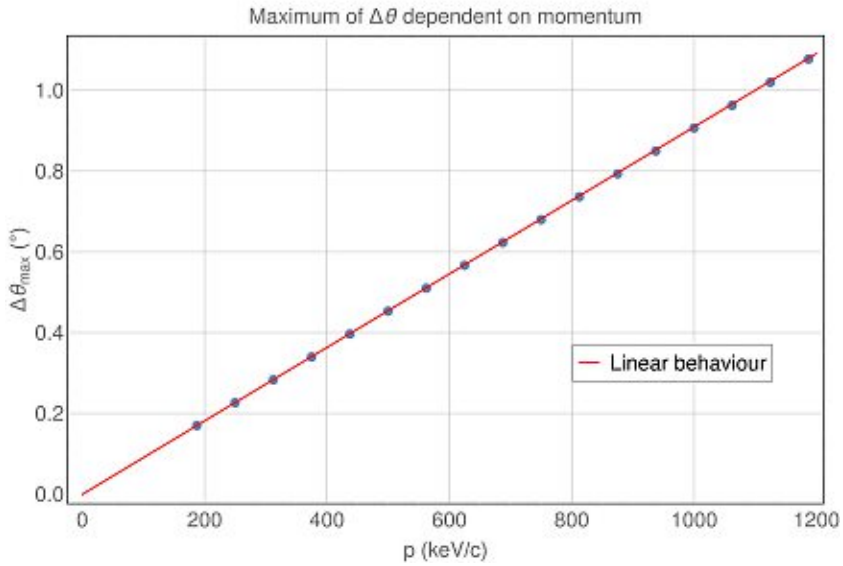

Figure 7.4.: The maximum of the non-adiabatic deviation $\Delta\theta$ dependent on momentum p (blue). A line is fitted to the data points to illustrate the linear dependency (red).

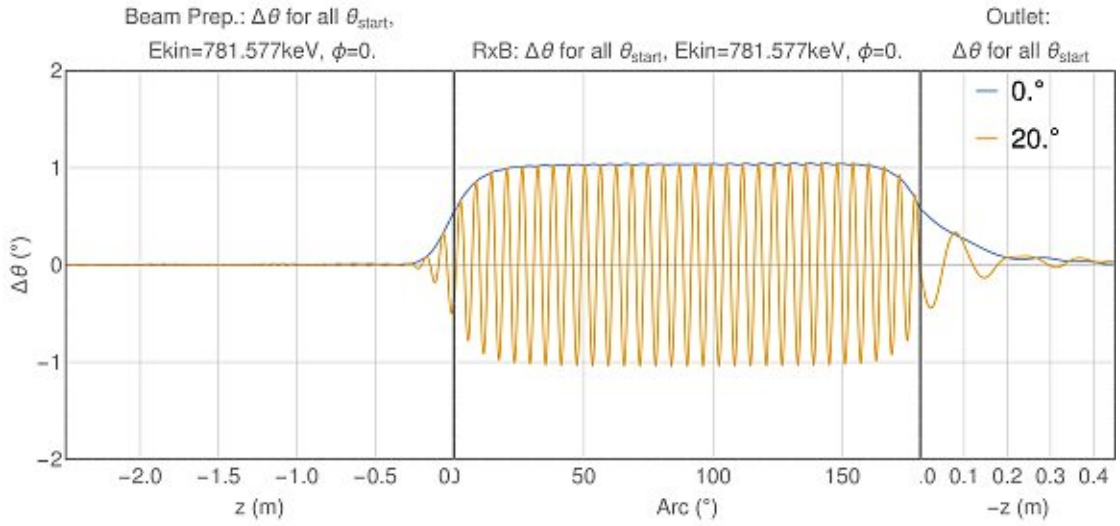

Figure 7.5.: The non-adiabatic quantity $\Delta\theta$ plotted for particle tracks with varying θ_0 through NoMoS in the single regions.

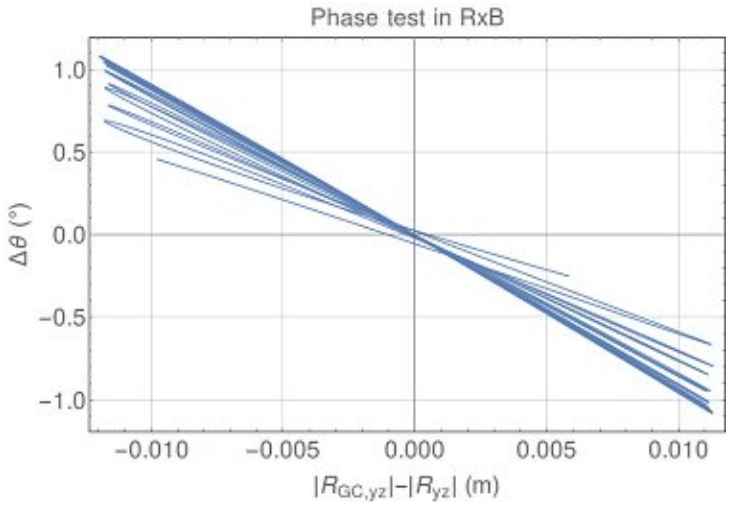

Figure 7.6.: The non-adiabatic quantity $\Delta\theta$ of a particle gyrating in the $R \times B$ region dependent on the local radial position R_{yz} relative to the guiding center's radial position $R_{\mathrm{GC},yz}$.

be compared to a $\Delta\theta$ plot to show magnificent agreement, indicated in Fig. 7.7.

We modeled the oscillatory behavior mathematically (even the non-full periods of oscillation, because they contribute most to the asymmetry) to calculate the average effect on the pitch angle dependent factor $f(\theta_{R\times B})$ (see Equ. 2.29). The averaging over the $R \times B$ arc is described as

$$\bar{f}(\theta_{R\times B}, p) = \frac{1}{\psi}\int_0^{\psi} f(\theta_{R\times B} + \Delta\theta(p,\psi))d\psi \tag{7.16}$$

The relative effect can be up to $\bar{f}/f - 1 \leq 3 \times 10^{-4}$ (only for largest θ_0 and p). Setting up a model for the correction to f in the transfer's $R \times B$ drift, we can estimate the effect (check Δb introduced by not considering this correction at all compared to the fitted data). We obtain a mimicked effect on b by omitting the correction of $\Delta b = 4 \times 10^{-4}$. Due to the significantly increased computation time and the only minor systematic effect, we decided against including it in our investigations.

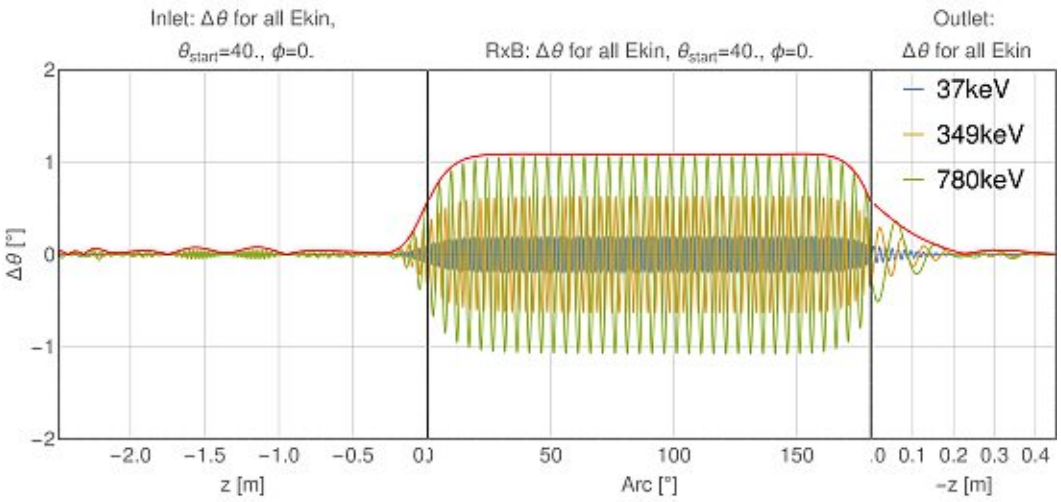

Figure 7.7.: The non-adiabatic quantity $\Delta\theta$ of a particle gyrating in the $R \times B$ region dependent on the kinetic energy. The behavior of $\Delta\alpha$ is scaled and overlayed onto the plot (red curve) to illustrate the strong correlation between this non-adiabatic effect and the measure of curvature.

7.2.2. Phase Angle Relations

In the transfer implemented in Ch. 4, we assumed fully uncorrelated phase angles at the relevant regions of interest, namely ϕ_{DV}, ϕ_{A} and ϕ_{D}. This is only exact for an infinitely long decay volume, which would allow for any ϕ_{A} for a specific ϕ_{DV}, momentum p and incident angle θ_0. Nonetheless, investigations have shown that there is no clear relation between the phase angles, that can be established. Such relations would significantly simplify the transfer procedure as it reduces the number of integration dimensions.

Phase Angle of Particle Trajectories

One way to investigate possible relations between the phase angles in the different regions is to simulate particle trajectories with the same guiding center starting point and varying the other starting parameters systematically. Comparing the phase angle ϕ_{A} and ϕ_{D} with the incident phase angle ϕ_{DV}, dependent on energy and incident pitch angle θ_0 can give insight into possible correlations. In Fig. 7.8, we compare a chosen incident phase angle ϕ_{DV} with the phase angle at the aperture and the detector, respectively, with the quantities $\phi_{\mathrm{A}} - \phi_{\mathrm{DV}}$ and $\phi_{\mathrm{D}} - \phi_{\mathrm{DV}}$ dependent on the kinetic energy T_{e} and the incident pitch angle θ_0.

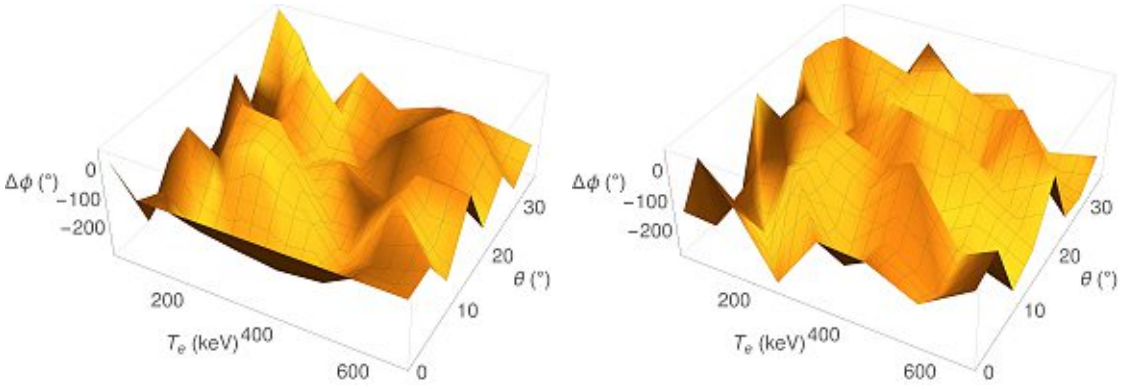

(a) (b)

Figure 7.8.: Linearly interpolated plots of the phase angle differences dependent on kinetic energy T_e and incident pitch angle θ_0 for (a) the aperture and (b) the detector.

Even by investigating 1D cuts and finer data points, we are not able to find any fundamentally describable periodic structure. The figures look completely analogous for different starting phase angles ϕ_{DV}. We conclude that no easy to implement way for correlating the phase angles is possible.

Point Source Investigations - the Point Spread Function

Another perspective is given by the so called magnetic point spread function (PSF), discussed in [DRM+14, Dub15, SBM+15]. In general, this function describes, how particles from a point source are distributed on a detector, that is connected to the source with a homogeneous magnetic field. We conducted point source Monte Carlo simulations, defining a source point and dicing the starting phase angle ϕ_{DV} while holding the momentum p and the incident pitch angle θ_0 constant. Figure 7.9 shows histograms of the point source particles at the aperture and the detector for the NC NoMoS configuration.

We observe a sharp peak in the center, as this is where all possible gyration circles overlap and the boundary limited to a radius of $2r_G$. If we sum up this histogram over the phase angle relative to the center, we obtain Fig. 7.10.

In the classical understanding, if all local phase angles ϕ are equally possible at the aperture and detector, respectively, the observed distributions should be flat plateaus. Nonetheless, at least at the aperture (Fig 7.10a), significant peaks are

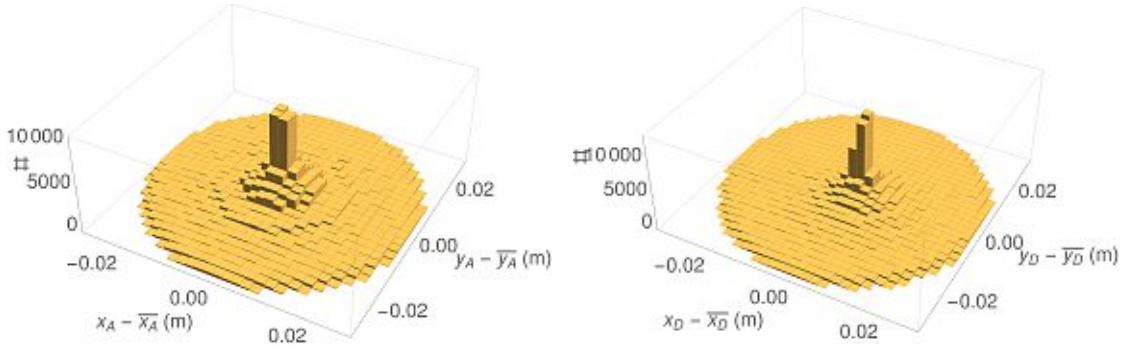

(a) (b)

Figure 7.9.: Histograms of particles tracked through NoMoS from a point source binned in the perpendicular coordinates relative to the mean central coordinate at (a) the aperture and (b) at the detector.

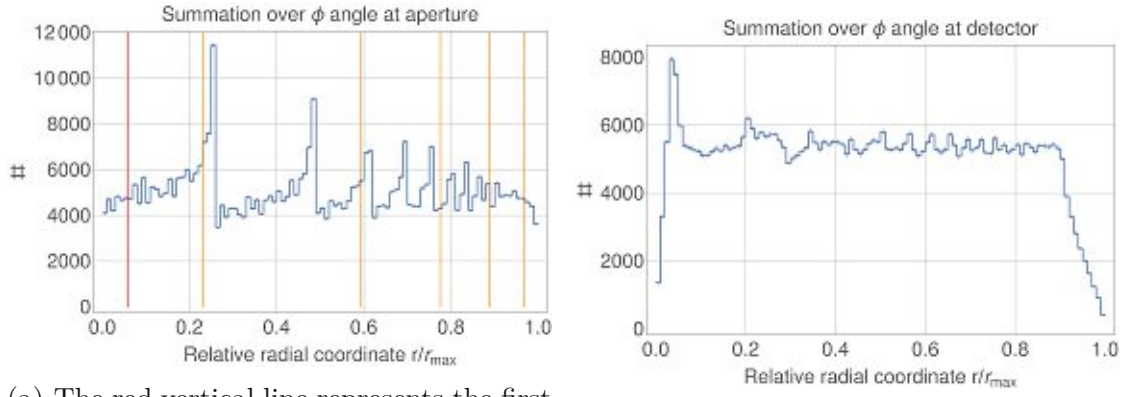

(a) The red vertical line represents the first peak position according to Dubber's PSF [Dub15] for a non-uniform magnetic field (further solutions are not within the plot range), whereas the orange lines are the PSF's peaks assuming a uniform field.

(b) Summed histogram over the angular coordinate at the detector. No significant peaks compared to the aperture are present. The first peak is probably due to the inaccurate central position, which is the center point for this plot.

Figure 7.10.: Histograms of particles tracked through NoMoS from a point source summed over the angular coordinate of Fig. 7.9 dependent on the relative radial coordinate to the maximum radial value at (a) the aperture and (b) the detector.

present. These peaks indicate that some phase angles are more probable than others (some angles might not be possible at all). There are no comparable peaks at the detector histogram present.

Figure 7.10a additionally shows expected peak positions for this distribution according to Dubber's PSF [Dub15]. Unfortunately, they can not reproduce the observed peaks. There is multiple reasons for this: First, the magnetic field develops highly non-uniformly with the filter peak present. Also, the filter magnetic field maximum changes the path of the particle's guiding center (we have seen that this is even true for a particle along the central magnetic field line). Therefore the path length can not be adequately calculated. Furthermore, very slight non-adiabatic effects can further distort the result.

In summary, we observe some structure at the aperture, but we can not reproduce it with the PSF. At the detector, no structure from a point source is present anymore in regards to possible phase angle dependencies. This in combination with the previous discussion with systematic particle tracks and a decay volume length in z of 10 centimeter leads to the conclusion that uncorrelated phase angles at the different regions of interest are a valid first assumption for the transfer.

The purpose of this outlook chapter was to give insight into possible further investigations in the approach of ultimate precision with the NoMoS experiment. On the one hand, we showed possible ways of improving the transfer description by modifying the drift or other effects in it. On the other hand, we showcased some examples of examining further systematic effects with particle tracking.

A. Coil Set-Up Data

Here, we list the coil data used for our simulations, showing the normal-conducting configuration in Tab. A.1 and the super-conducting version in Tab. A.2. Both set-ups were optimized by us to meet many different demands.

Table A.1.: The coil data for the normal-conducting configuration. The columns are: a number, the region of the coil, the z and y coordinate of the coil's center, the inner and outer radius r_{inner} and r_{outer}, the width w, the tilt angle α and the current density j. All lengths are in millimetre.

#	Region	z	y	r_{inner}	r_{outer}	w	α (°)	j (A/mm²)
1	RxB	0.	999.	220.	291.	62.	0.	2.89
2	RxB	104.42	993.53	220.	291.	62.	6.	4.13
3	RxB	207.70	977.17	220.	291.	62.	12.	4.13
4	RxB	308.71	950.11	220.	291.	62.	18.	4.13
5	RxB	406.33	912.63	220.	291.	62.	24.	4.13
6	RxB	499.5	865.16	220.	291.	62.	30.	4.13
7	RxB	587.2	808.21	220.	291.	62.	36.	4.13
8	RxB	668.46	742.4	220.	291.	62.	42.	4.13
9	RxB	742.4	668.46	220.	291.	62.	48.	4.13
10	RxB	808.21	587.2	220.	291.	62.	54.	4.13
11	RxB	865.16	499.5	220.	291.	62.	60.	4.13
12	RxB	912.63	406.33	220.	291.	62.	66.	4.13
13	RxB	950.11	308.71	220.	291.	62.	72.	4.13
14	RxB	977.17	207.70	220.	291.	62.	78.	4.13
15	RxB	993.53	104.42	220.	291.	62.	84.	4.13
16	RxB	999.	0.	220.	291.	62.	90.	4.13
17	RxB	993.53	-104.42	220.	291.	62.	96.	4.13
18	RxB	977.17	-207.70	220.	291.	62.	102.	4.13
19	RxB	950.11	-308.71	220.	291.	62.	108.	4.13
20	RxB	912.63	-406.33	220.	291.	62.	114.	4.13
21	RxB	865.16	-499.5	220.	291.	62.	120.	4.13
22	RxB	808.21	-587.2	220.	291.	62.	126.	4.13
23	RxB	742.4	-668.46	220.	291.	62.	132.	4.13

#	Region	z	y	r_{inner}	r_{outer}	w	α (°)	j (A/mm^2)
24	RxB	668.46	-742.4	220.	291.	62.	138.	4.13
25	RxB	587.2	-808.21	220.	291.	62.	144.	4.13
26	RxB	499.5	-865.16	220.	291.	62.	150.	4.13
27	RxB	406.33	-912.63	220.	291.	62.	156.	4.13
28	RxB	308.71	-950.11	220.	291.	62.	162.	4.13
29	RxB	207.70	-977.17	220.	291.	62.	168.	4.13
30	RxB	104.42	-993.53	220.	291.	62.	174.	4.13
31	RxB	0.	-999.	220.	291.	62.	180.	3.1
32	Outlet	-101.5	-974.	250.	321.	53.	180.	3.32
33	Outlet	-234.5	-974.	250.	321.	53.	180.	3.73
34	Outlet	-331.5	-974.	250.	321.	53.	180.	3.73
35	Outlet	-428.5	-974.	250.	321.	53.	180.	3.73
36	Outlet	-525.5	-974.	250.	321.	53.	180.	3.73
37	Outlet	-622.5	-974.	250.	321.	53.	180.	3.73
38	Outlet	-719.5	-974.	250.	321.	53.	180.	3.73
39	Outlet	-816.5	-974.	250.	321.	53.	180.	3.73
40	Outlet	-913.5	-974.	250.	321.	53.	180.	3.73
41	Outlet	-1010.5	-974.	250.	321.	53.	180.	3.73
42	Outlet	-1107.5	-974.	250.	321.	53.	180.	3.73
43	OutletCorr	-261.5	-974.	346.	417.	53.	180.	3.32
44	OutletCorr	-684.5	-974.	346.	417.	53.	180.	3.32
45	OutletCorr	-1107.5	-974.	346.	417.	53.	180.	3.32
46	Inlet	-95.	999.	220.	291.	44.	0.	3.16
47	Inlet	-181.	999.	220.	291.	44.	0.	4.16
48	Inlet	-273.	999.	220.	291.	44.	0.	4.16
49	Inlet	-359.	999.	220.	291.	44.	0.	4.16
50	Inlet	-445.	999.	220.	291.	44.	0.	4.16
51	Inlet	-531.	999.	220.	291.	44.	0.	4.16
52	Inlet	-617.	999.	220.	291.	44.	0.	4.16
53	Inlet	-703.	999.	220.	291.	44.	0.	4.16
54	Inlet	-789.	999.	220.	291.	44.	0.	4.16
55	Inlet	-875.	999.	220.	291.	44.	0.	4.16
56	Inlet	-961.	999.	220.	291.	44.	0.	4.16
57	Inlet	-1047.	999.	220.	291.	44.	0.	4.16
58	Inlet	-1133.	999.	220.	291.	44.	0.	4.16
59	Inlet	-1219.	999.	220.	291.	44.	0.	4.16
60	Inlet	-1305.	999.	220.	291.	44.	0.	4.16
61	Inlet	-1391.	999.	220.	291.	44.	0.	4.16
62	Inlet	-1477.	999.	220.	291.	44.	0.	4.16

#	Region	z	y	r_{inner}	r_{outer}	w	α (°)	j (A/mm²)
63	Inlet	-1564.	999.	220.	291.	44.	0.	4.16
64	Inlet	-1651.	999.	220.	291.	44.	0.	4.16
65	Inlet	-1738.	999.	220.	291.	44.	0.	4.16
66	Inlet	-1825.	999.	220.	291.	44.	0.	4.16
67	Inlet	-1912.	999.	220.	291.	44.	0.	4.16
68	Inlet	-1999.	999.	220.	291.	44.	0.	4.16
69	Inlet	-2086.	999.	220.	291.	44.	0.	4.16
70	Inlet	-2173.	999.	220.	291.	44.	0.	4.16
71	Inlet	-2260.	999.	220.	291.	44.	0.	0.21
72	Helmholtz	-2364.	999.	220.	489.	44.	0.	4.04
73	Helmholtz	-2588.	999.	220.	489.	44.	0.	4.33
74	Filter	-1527.	999.	311.	454.	143.	0.	5.09
75	Filter	-1184.	999.	311.	454.	143.	0.	5.09
76	Connector	-2742.	999.	220.	291.	44.	0.	3.84
77	Connector	-2848.5	999.	220.	291.	89.	0.	3.80
78	Connector	-2977.5	999.	220.	291.	89.	0.	3.80
79	EnterCorr	-81.	999.	340.	411.	53.	-5.	4.56
80	ExitCorr	-81.46	-972.62	340.	411.	53.	-177.	3.32

Table A.2.: The coil data for the super-conducting configuration. The columns are: a number, the region of the coil, the z and y coordinate of the coil's center, the inner and outer radius r_{inner} and r_{outer}, the width w, the tilt angle α and the current density j. All lengths are in millimetre.

#	Region	z	y	r_{inner}	r_{outer}	w	α (°)	j (A/mm²)
1	RxB	0.	757.12	140.	159.5	44.2	0.	43.95
2	RxB	69.86	753.89	140.	159.5	44.2	5.29	62.79
3	RxB	139.12	744.22	140.	159.5	44.2	10.59	62.79
4	RxB	207.19	728.21	140.	159.5	44.2	15.88	62.79
5	RxB	273.5	705.99	140.	159.5	44.2	21.18	62.79
6	RxB	337.48	677.74	140.	159.5	44.2	26.47	62.79
7	RxB	398.57	643.71	140.	159.5	44.2	31.76	62.79
8	RxB	456.26	604.19	140.	159.5	44.2	37.06	62.79
9	RxB	510.07	559.52	140.	159.5	44.2	42.35	62.79
10	RxB	559.52	510.07	140.	159.5	44.2	47.65	62.79
11	RxB	604.19	456.26	140.	159.5	44.2	52.94	62.79
12	RxB	643.71	398.57	140.	159.5	44.2	58.24	62.79
13	RxB	677.74	337.48	140.	159.5	44.2	63.53	62.79
14	RxB	705.99	273.5	140.	159.5	44.2	68.82	62.79
15	RxB	728.21	207.19	140.	159.5	44.2	74.12	62.79

#	Region	z	y	r_{inner}	r_{outer}	w	α (°)	j (A/mm^2)
16	RxB	744.22	139.12	140.	159.5	44.2	79.41	62.79
17	RxB	753.89	69.86	140.	159.5	44.2	84.71	62.79
18	RxB	757.12	0.	140.	159.5	44.2	90.	62.79
19	RxB	753.89	-69.86	140.	159.5	44.2	95.29	62.79
20	RxB	744.22	-139.12	140.	159.5	44.2	100.59	62.79
21	RxB	728.21	-207.19	140.	159.5	44.2	105.88	62.79
22	RxB	705.99	-273.5	140.	159.5	44.2	111.18	62.79
23	RxB	677.74	-337.48	140.	159.5	44.2	116.47	62.79
24	RxB	643.71	-398.57	140.	159.5	44.2	121.76	62.79
25	RxB	604.19	-456.26	140.	159.5	44.2	127.06	62.79
26	RxB	559.52	-510.07	140.	159.5	44.2	132.35	62.79
27	RxB	510.07	-559.52	140.	159.5	44.2	137.65	62.79
28	RxB	456.26	-604.19	140.	159.5	44.2	142.94	62.79
29	RxB	398.57	-643.71	140.	159.5	44.2	148.24	62.79
30	RxB	337.48	-677.74	140.	159.5	44.2	153.53	62.79
31	RxB	273.5	-705.99	140.	159.5	44.2	158.82	62.79
32	RxB	207.19	-728.21	140.	159.5	44.2	164.12	62.79
33	RxB	139.12	-744.22	140.	159.5	44.2	169.41	62.79
34	RxB	69.86	-753.89	140.	159.5	44.2	174.71	62.79
35	RxB	0.	-757.12	140.	159.5	44.2	180.	31.40
36	Outlet	-60.8	-747.12	160.	173.8	74.6	180.	54.16
37	Outlet	-136.8	-747.12	160.	173.8	74.6	180.	54.16
38	Outlet	-212.8	-747.12	160.	173.8	74.6	180.	54.16
39	Outlet	-288.8	-747.12	160.	173.8	74.6	180.	54.16
40	Outlet	-364.8	-747.12	160.	173.8	74.6	180.	54.16
41	Outlet	-440.8	-747.12	160.	173.8	74.6	180.	54.16
42	Outlet	-516.8	-747.12	160.	173.8	74.6	180.	54.16
43	Outlet	-592.80	-747.12	160.	173.8	74.6	180.	54.16
44	Outlet	-668.80	-747.12	160.	173.8	74.6	180.	54.16
45	Outlet	-744.80	-747.12	160.	173.8	74.6	180.	54.16
46	Outlet	-820.80	-747.12	160.	173.8	74.6	180.	54.16
47	Outlet	-896.80	-747.12	160.	173.8	74.6	180.	54.16
48	Outlet	-972.80	-747.12	160.	173.8	74.6	180.	54.16
49	Outlet	-1048.8	-747.12	160.	173.8	74.6	180.	54.16
50	OutletCorr	-276.4	-747.12	183.8	188.1	13.8	180.	82.91
51	OutletCorr	-410.2	-747.12	183.8	188.1	13.8	180.	82.91
52	OutletCorr	-544.	-747.12	183.8	188.1	13.8	180.	82.91
53	OutletCorr	-677.80	-747.12	183.8	188.1	13.8	180.	82.91
54	OutletCorr	-811.6	-747.12	183.8	188.1	13.8	180.	82.91

#	Region	z	y	r_{inner}	r_{outer}	w	α (°)	j (A/mm²)
55	OutletCorr	-945.4	-747.12	183.8	188.1	13.8	180.	82.91
56	OutletCorr	-1079.2	-747.12	183.8	188.1	13.8	180.	82.91
57	Inlet	-51.3	757.12	140.	151.9	55.6	0.	55.31
58	Inlet	-108.3	757.12	140.	151.9	55.6	0.	65.07
59	Inlet	-165.3	757.12	140.	151.9	55.6	0.	65.07
60	Inlet	-222.3	757.12	140.	151.9	55.6	0.	65.07
61	Inlet	-279.3	757.12	140.	151.9	55.6	0.	65.07
62	Inlet	-336.3	757.12	140.	151.9	55.6	0.	65.07
63	Inlet	-393.3	757.12	140.	151.9	55.6	0.	65.07
64	Inlet	-450.3	757.12	140.	151.9	55.6	0.	65.07
65	Inlet	-507.3	757.12	140.	151.9	55.6	0.	65.07
66	Inlet	-564.30	757.12	140.	151.9	55.6	0.	65.07
67	Inlet	-621.30	757.12	140.	151.9	55.6	0.	65.07
68	Inlet	-678.30	757.12	140.	151.9	55.6	0.	65.07
69	Inlet	-735.30	757.12	140.	151.9	55.6	0.	65.07
70	Inlet	-792.30	757.12	140.	151.9	55.6	0.	65.07
71	Inlet	-849.30	757.12	140.	151.9	55.6	0.	65.07
72	Inlet	-906.30	757.12	140.	151.9	55.6	0.	65.07
73	Inlet	-963.30	757.12	140.	151.9	55.6	0.	65.07
74	Inlet	-1020.30	757.12	140.	151.9	55.6	0.	65.07
75	Inlet	-1077.3	757.12	140.	151.9	55.6	0.	65.07
76	Inlet	-1134.3	757.12	140.	151.9	55.6	0.	65.07
77	Inlet	-1191.3	757.12	140.	151.9	55.6	0.	65.07
78	Inlet	-1248.3	757.12	140.	151.9	55.6	0.	65.07
79	Inlet	-1305.3	757.12	140.	151.9	55.6	0.	65.07
80	Inlet	-1362.3	757.12	140.	151.9	55.6	0.	65.07
81	Inlet	-1419.3	757.12	140.	151.9	55.6	0.	65.07
82	Inlet	-1476.3	757.12	140.	151.9	55.6	0.	65.07
83	Inlet	-1533.3	757.12	140.	151.9	55.6	0.	35.79
84	Inlet	-1590.3	757.12	140.	151.9	55.6	0.	35.79
85	Inlet	-1647.3	757.12	140.	151.9	55.6	0.	35.79
86	Helmholtz	-1755.8	757.12	250.	410.1	21.4	0.	87.88
87	Helmholtz	-1897.2	757.12	250.	410.1	21.4	0.	45.25
88	Filter	-1077.3	757.12	161.9	236.5	44.2	0.	80.57
89	Filter	-883.1	757.12	161.9	236.5	44.2	0.	80.57
90	Connector	-1966.7	757.12	140.	195.6	17.6	0.	40.77
91	Connector	-2014.3	757.12	140.	195.6	17.6	0.	58.25
92	Connector	-2181.9	757.12	140.	195.6	17.6	0.	58.25
93	EnterCorr	-42.1	757.12	210.	235.2	17.6	-5.	51.77

#	Region	z	y	r_{inner}	r_{outer}	w	α (°)	j (A/mm^2)
94	ExitCorr	-42.29	-746.66	210.	235.2	17.6	-177.	64.71

B. Systematic Parameters of the Super-conducting System

This appendix chapter lists the systematic parameters obtained from the super-conducting NoMoS set-up along with the respective uncertainties. Compared to the normal-conducting version, some of the uncertainties are significantly smaller, e.g. the magnetic field ratio ones. The full list is given in Tab. B.1.

Table B.1.: Determined systematic parameters of the super-conducting NoMoS standalone set-up with respective uncertainties. The asterisk * marks if the uncertainty is given in absolute values.

Systematic Effect	**Parameter**	**Value**	**Rel. uncertainty** ($\times 10^{-3}$)
Magnetic field			
Filter magnetic field ratio	r_{F}	2.036	0.157
Aperture magnetic field ratio	r_{A}	0.937	0.106
$R \times B$ magnetic field ratio	$r_{\mathrm{R\times B}}$	0.902	0.150
Magnetic field in $R \times B$ region	$B_{\mathrm{R\times B}}$	0.976 T	0.150
Radial gradient coefficients	G_1	1.290	2.000
	G_2	1.792	2.000
Curvature angle	α	180.030 °	0.100
Detector magnetic field ratio	r_{D}	0.880	0.047
Central field line movement	$x_{\mathrm{A,Shift}}$	0.000 mm	0.100 mm*
	$y_{\mathrm{A,Shift}}$	2.873 mm	0.100 mm*
	$y_{R\times B,\mathrm{Shift}}$	1.518 mm	0.100 mm*
	$x_{\mathrm{D,Shift}}$	0.000 mm	0.100 mm*
	$y_{\mathrm{D,Shift}}$	6.234 mm	0.100 mm*
Other			
Aperture dimensions	x_{AA}	10.000 mm	0.200 mm*
	y_{AA}	35.000 mm	0.200 mm*
	$x_{\mathrm{A,Offset}}$	30.000 mm	0.200 mm*
	$y_{\mathrm{A,Offset}}$	0.000 mm	0.200 mm*
Neutron beam	$w_{n,x}$, $w_{n,y}$	10, 6 cm	0.750
	$p_{n,x}$, $p_{n,y}$	9, 5 cm	2.600
	$k_{x,1}$, $k_{y,1}$	0.9	6.000
	$k_{x,2}$, $k_{y,2}$	0	1.000*
	$k_{x,3}$, $k_{y,3}$	-0.9	1.000

C. Thoughts on Magnetic Field Measurement in NoMoS

NoMoS has an intricate magnetic design and systematic effects that require precise understand of the magnetic field. Therefore, special thought has to be given to measuring the field profile accurately. The overall accuracy is given by the magnetic field probe's as well as the positional (3D) accuracy.

C.1. Magnetic Sield Sensors

At least in the $R \times B$ region, a high accuracy of $\Delta B/B = 1 \times 10^{-4}$ is required. This is not easily achieved, especially for conventional Hall probes (they usually reach the 10^{-3} precision level). NMR probes in general offer higher accuracy but have some caveats. They do no work well in significant field gradients (as is the case in the $R \times B$ region) and don't offer 3D field component information.

This is why we plan on a combination of the two technologies. We use a three-component hall probe to scan the $R \times B$ region (as well as the beam preparation area and detection region) and a NMR probe as a reference measurement outside of the field gradient for intermediate gauging of the hall probe.

C.2. Positioning of the Sensors

Of course, high positional accuracy has to be achieved as well. We suggest a rail system, that is permanently installed in the vacuum system. Danfysik designed such a rail system within a design study, shown in Fig. C.1. It allows movement of a cart on the rails through the whole system.

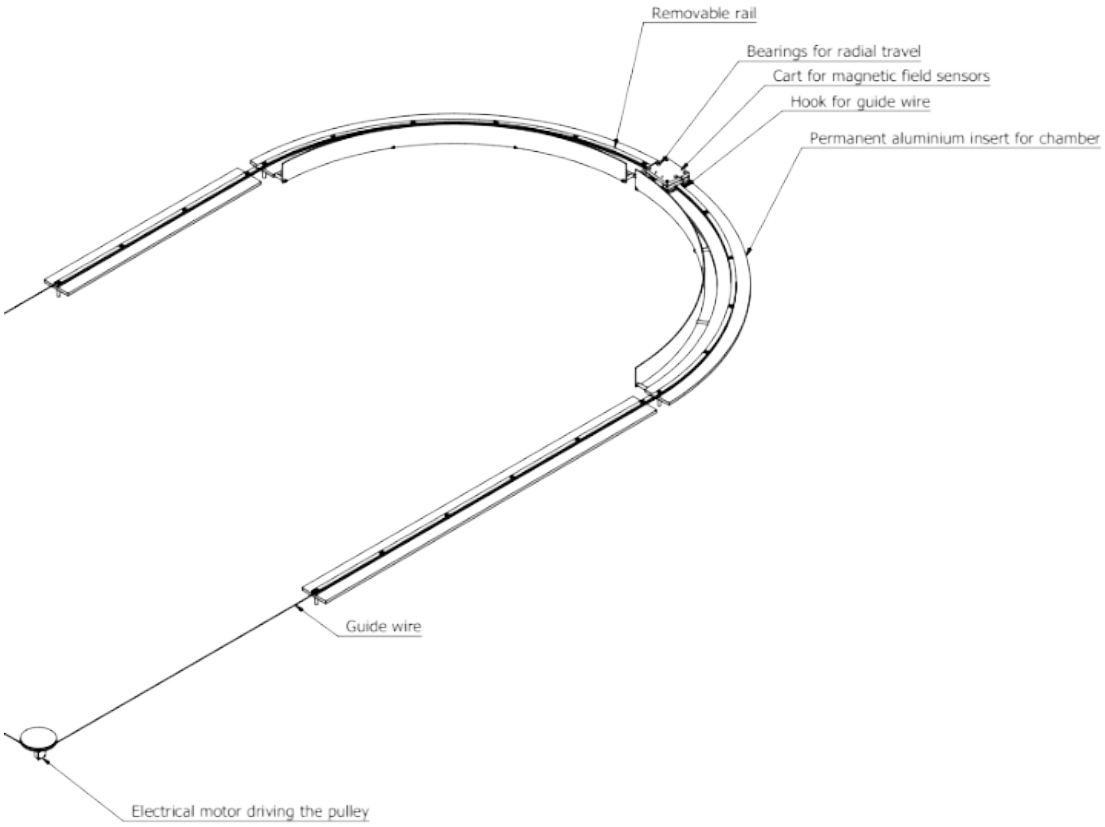

Figure C.1.: Rail system design proposed by *Danfysik*. It consists of an aluminium frame fixed at several flanges which is installed in multiple parts before an experimental run. A cart, holding a hall probe can move along a rail on the frame with the help of a guide wire. This wire is moved with an electric motor on the outside. The wire is also connected with the other end looped through the system to ensure utmost stability.

Bibliography

[A+06] H. Abele et al. Characterization of a ballistic supermirror neutron guide. *Nuclear Instruments and Methods in Physics Research Section A: Accelerators, Spectrometers, Detectors and Associated Equipment*, 562(1):407 – 417, 2006. 43

[A+10] M. Antonelli et al. Flavor physics in the quark sector. *Physics Reports*, 494(3):197 – 414, 2010. 7

[A+15] S. Arzumanov et al. A measurement of the neutron lifetime using the method of storage of ultracold neutrons and detection of inelastically up-scattered neutrons. *Physics Letters B*, 745:79 – 89, 2015. 15

[B+96] J Byrne et al. A revised value for the neutron lifetime measured using a penning trap. *Europhysics Letters (EPL)*, 33(3):187–192, jan 1996. 15

[B+16] T. Bhattacharya et al. Axial, scalar, and tensor charges of the nucleon from $2+1+1$-flavor lattice qcd. *Phys. Rev. D*, 94:054508, Sep 2016. 17

[B+20] M. Beck et al. Improved determination of the $\beta-\overline{\nu}_e$ angular correlation coefficient a in free neutron decay with the aSPECT spectrometer. *Phys. Rev. C*, 101:055506, May 2020. 8, 13

[BCC+12] Tanmoy Bhattacharya, Vincenzo Cirigliano, Saul D. Cohen, Alberto Filipuzzi, Martín González-Alonso, Michael L. Graesser, Rajan Gupta, and Huey-Wen Lin. Probing novel scalar and tensor interactions from (ultra)cold neutrons to the lhc. *Phys. Rev. D*, 85:054512, Mar 2012. 17

[Ber19] Zurab Berezhiani. Neutron lifetime puzzle and neutron–mirror neutron oscillation. *The European Physical Journal C*, 79(6):484, 2019. 15

[CMS04] Andrzej Czarnecki, William J. Marciano, and Alberto Sirlin. Precision measurements and ckm unitarity. *Phys. Rev. D*, 70:093006, Nov 2004. 8, 12

[CMS18] Andrzej Czarnecki, William J. Marciano, and Alberto Sirlin. Neutron lifetime and axial coupling connection. *Phys. Rev. Lett.*, 120:202002, May 2018. 15

[CMS19] Andrzej Czarnecki, William J. Marciano, and Alberto Sirlin. Radiative corrections to neutron and nuclear beta decays revisited. *Phys. Rev. D*, 100:073008, Oct 2019. 8, 14, 15

[COM] COMSOL, Inc. `http://www.comsol.com/comsol-multiphysics`. 25

[D+00] P. G. Dawber et al. *Nucl. Instr. and Meth.*, A 440:543, 2000. 13

[D+08] D. Dubbers et al. A clean, bright, and versatile source of neutron decay products. *Nucl. Instrum. Meth. Phys. Res., Sect. A*, 596(2):238 – 247, 2008. 44

[DKMS05] A. Dinklage, T. Klinger, G. Marx, and L. Schweikhard. *Plasma Physics*. Springer Berlin Heidelberg, 2005. 22, 23

[DRM+14] D. Dubbers, L. Raffelt, B. Märkisch, F. Friedl, and H. Abele. The point spread function of electrons in a magnetic field, and the decay of the free neutron. *Nuclear Instruments and Methods in Physics Research Section A: Accelerators, Spectrometers, Detectors and Associated Equipment*, 763:112 – 119, 2014. 129

[DS11] Dirk Dubbers and Michael G. Schmidt. The neutron and its role in cosmology and particle physics. *Reviews of Modern Physics*, 83(4):1111–1171, oct 2011. 14

[DSM+19] D. Dubbers, H. Saul, B. Märkisch, T. Soldner, and H. Abele. Exotic decay channels are not the cause of the neutron lifetime anomaly. *Physics Letters B*, 791:6 – 10, 2019. 15

[Dub15] Dirk Dubbers. Magnetic guidance of charged particles. *Physics Letters B*, 748:306 – 310, 2015. 129, 130, 131

[E. 16] E. Klinkby (nnbar collab.), T. Soldner (ANNI collab.). Fundamental physics possibilities at the european spallation source. *J. Phys.: Conf. Ser.*, 746(1):012051, 2016. 45

[E+18] V. F. Ezhov et al. Measurement of the neutron lifetime with ultra-cold neutrons stored in a magneto-gravitational trap. *JETP Letters*, 107(11):671–675, June 2018. 15

[F+17] Daniel Furse et al. Kassiopeia: a modern, extensible cpp particle tracking package. *New Journal of Physics*, 19(5):053012, may 2017. 27

[F+18] J. Fry et al. The nab experiment: A precision measurement of unpolarized neutron beta decay. In *International Workshop on Particle Physics at Neutron Sources 2018 (PPNS 2018) Grenoble, France, May 24-26, 2018*, 2018. 8

[FG18] Bartosz Fornal and Benjamín Grinstein. Dark matter interpretation of the neutron decay anomaly. *Phys. Rev. Lett.*, 120:191801, May 2018. 15

[FG20] Bartosz Fornal and Benjamín Grinstein. Neutron's dark secret. *Modern Physics Letters A*, 35(31):2030019, 2020. 15

[FGANC20] Adam Falkowski, Martín González-Alonso, and Oscar Naviliat-Cuncic. Comprehensive analysis of beta decays within and beyond the standard model. *ArXiv e-print: 2010.13797*, 2020. 13, 16

[FGM58] R. P. Feynman and M. Gell-Mann. Theory of the fermi interaction. *Phys. Rev.*, 109:193–198, Jan 1958. 8, 10

[G+95] F. Glück et al. Measurable parameters of neutron decay. *Nucl. Phys. A*, 593:125, 1995. 7

[GANC16] M. González-Alonso and O. Naviliat-Cuncic. Kinematic sensitivity to the fierz term of beta-decay differential spectra. *Physical Review C*, 94(3), Sep 2016. 8

[GANCS19] M. González-Alonso, O. Naviliat-Cuncic, and N. Severijns. New physics searches in nuclear and neutron beta decay. *Prog. Part. Nucl. Phys.*, 104:165 – 223, 2019. 16, 17

[GGS58] M. Goldhaber, L. Grodzins, and A. W. Sunyar. Helicity of neutrinos. *Phys. Rev.*, 109:1015–1017, Feb 1958. 8, 10

[Glü93] F. Glück. Measurable distributions of unpolarized neutron decay. *Phys. Rev.*, D 47:2840, 1993. 55

[Glü11] Ferenc Glück. Axisymmetric magnetic field calculation with zonal harmonic expansion. *Progress In Electromagnetics Research B*, 32:351–388, 2011. 25

[Glü12] F Glück. Axisymmetric electric and magnetic field calculations with zonal harmonic expansion. *Proc. PIERS (Kuala Lumpur, 27–30 March, 2012)*, pages 1698–1702, 2012. 25

[Glü13] Ferenc Glück. EM field, tracking and scattering simulations for the KATRIN experiment. *Journal of Physics: Conference Series*, 410:012039, feb 2013. 27

[GM83] A. C. Genz and A. A. Malik. *An Imbedded Family of Fully Symmetric Numerical Integration Rules*. Society of Industrial and Applied Mathematics, 1983. 28

[H+17a] K. P. Hickerson et al. First direct constraints on fierz interference in free-neutron β decay. *Phys. Rev. C*, 96:042501, Oct 2017. 9, 17

[H+17b] K. P. Hickerson et al. Publisher's note: First direct constraints on fierz interference in free-neutron β decay. *Phys. Rev. C*, 96:059901, Nov 2017. 9

[H+19] Hoogerheide, Shannon F. et al. Progress on the BL2 beam measurement of the neutron lifetime. *EPJ Web Conf.*, 219:03002, 2019. 16

[Her01] P. Herczeg. Beta decay beyond the standard model. *Prog. Part. Nucl. Phys.*, 46(2):413 – 457, 2001. 16

[HT15] J. C. Hardy and I. S. Towner. Superallowed $0^+ \rightarrow 0^+$ nuclear β decays: 2014 critical survey, with precise results for V_{ud} and ckm unitarity. *Phys. Rev. C*, 91:025501, Feb 2015. 7, 14

[HT18] J. C. Hardy and I. S. Towner. Nuclear beta decays and CKM unitarity. *ArXiv e-prints*, June 2018. 7, 14

[Jac99] John David Jackson. *Classical Electrodynamics*. Wiley, New York, NY, 3. ed. edition, 1999. 18, 19, 20, 22, 25

[Jig20] Raluca Jiglau. Post acceleration electrode for the nomos experiment. Master's thesis, Universität Wien, 2020. 22, 25, 36

[JTW57a] J. D. Jackson, S. B. Treiman, and H. W. Wyld. Coulomb corrections

in allowed beta transitions. *Nucl. Phys.*, 4:206, 1957. 11

[JTW57b] J. D. Jackson, S. B. Treiman, and H. W. Wyld. Possible tests of time reversal invariance in beta decay. *Phys. Rep.*, 106:517, 1957. 11

[K+12] G Konrad et al. Neutron decay with PERC: a progress report. *J. Phys.: Conf. Ser.*, 340(1):012048, 2012. 44

[Kar17] Jan Peter Karch. *Design und Aufbau des Experiments tauSPECT zur Messung der Neutronlebensdauer mittels magnetischer Wandspeicherung*. PhD thesis, Johannes Gutenberg-Universität Mainz, 2017. 16

[Kha21] Waleed Khalid. *Detection System for NoMoS experiment*. PhD thesis, Technische Universität Wien, 2021. in progress. 29, 36, 54, 57, 58, 118

[KJM+19] M. Klopf, E. Jericha, B. Märkisch, H. Saul, T. Soldner, and H. Abele. Constraints on the dark matter interpretation $n \to \chi + e^+e^-$ of the neutron decay anomaly with the perkeo ii experiment. *Phys. Rev. Lett.*, 122:222503, Jun 2019. 15

[KM73] Makoto Kobayashi and Toshihide Maskawa. CP-Violation in the Renormalizable Theory of Weak Interaction. *Progress of Theoretical Physics*, 49(2):652–657, 02 1973. 7

[Kon11] G. E. Konrad. *Measurement of the Proton Recoil Spectrum in Neutron Beta Decay with the Spectrometer aSPECT: Study of Systematic Effects*. PhD thesis, Johannes Gutenberg-Universität, Mainz, 2011. 12

[KU98] Arnold R. Krommer and Christoph W. Ueberhuber. *Computational Integration*. Society of Industrial and Applied Mathematics, 1998. 28

[L+11] M. Lindroos et al. The european spallation source. *Nucl. Instrum. Methods Phys. Res., Sect. B*, 269(24):3258 – 3260, 2011. Proceedings of the 10th European Conference on Accelerators in Applied Research and Technology (ECAART10). 45

[Leh64] Bo Lehnert. *Dynamics of charged particles*. North-Holland, Amsterdam, 1964. 18, 20, 22

[Lob98] V.M. Lobashev. Search for the antineutrino rest mass in the tritium

beta decay. *Progress in Particle and Nuclear Physics*, 40:337 – 351, 1998. Neutrinos in Astro, Particle and Nuclear Physics. 9, 29

[LY56] T. D. Lee and C. N. Yang. Question of parity conservation in weak interactions. *Phys. Rev.*, 104:254–258, Oct 1956. 8, 10

[M+19] D. Moser et al. NoMoS: An $R \times B$ drift momentum spectrometer for beta decay studies. In *International Workshop on Particle Physics at Neutron Sources 2018 (PPNS 2018) Grenoble, France, May 24-26, 2018*, 2019. 29

[M+20] D. Moser et al. Recent design studies for the novel momentum spectrometer NoMoS. *Journal of Physics: Conference Series*, 2020. 43, 115

[Nac68] O. Nachtmann. Relativistic corrections to the recoil spectrum in neutron β-decay. *Z. Phys.*, 215:505, 1968. 13

[Nat20] National Nuclear Data Center. Nudat2.8. Technical report, Brookhaven National Laboratory, Last accessed on 9th of September, 2020. 31

[P+18] R. W. Pattie et al. Measurement of the neutron lifetime using a magneto-gravitational trap and in situ detection. *Science*, 360(6389):627–632, 2018. 15

[P+19] Pattie, R.W. et al. Status of the UCNtau experiment. *EPJ Web Conf.*, 219:03004, 2019. 16

[PVSG10] A. Pichlmaier, V. Varlamov, K. Schreckenbach, and P. Geltenbort. Neutron lifetime measurement with the ucn trap-in-trap mambo ii. *Physics Letters B*, 693(3):221 – 226, 2010. 15

[S+05] A. Serebrov et al. Measurement of the neutron lifetime using a gravitational trap and a low-temperature fomblin coating. *Physics Letters B*, 605(1):72 – 78, 2005. 15

[S+12] A. Steyerl et al. Quasielastic scattering in the interaction of ultracold neutrons with a liquid wall and application in a reanalysis of the mambo i neutron-lifetime experiment. *Phys. Rev. C*, 85:065503, Jun 2012. 15

[S+18a] Chien-Yeah Seng et al. Reduced hadronic uncertainty in the deter-

mination of V_{ud}. *Phys. Rev. Lett.*, 121:241804, Dec 2018. 14

[S+18b] X. Sun et al. Search for dark matter decay of the free neutron from the ucna experiment: $n \to \chi + e^+e^-$. *Phys. Rev. C*, 97:052501, May 2018. 15

[S+20a] Chien-Yeah Seng et al. Joint lattice qcd–dispersion theory analysis confirms the quark-mixing top-row unitarity deficit. *Phys. Rev. D*, 101:111301, Jun 2020. 14

[S+20b] X. Sun et al. Improved limits on fierz interference using asymmetry measurements from the ultracold neutron asymmetry (ucna) experiment. *Phys. Rev. C*, 101:035503, Mar 2020. 9, 17

[SBM+15] S. K. L. Sjue, L. J. Broussard, M. Makela, P. L. McGaughey, A. R. Young, and B. A. Zeck. Radial distribution of charged particles in a magnetic field. *Review of Scientific Instruments*, 86(2):023102, 2015. 129

[SBNC06] Nathal Severijns, Marcus Beck, and Oscar Naviliat-Cuncic. Tests of the standard electroweak model in nuclear beta decay. *Rev. Mod. Phys.*, 78:991–1040, Sep 2006. 17

[Sch60] George Schmidt. Plasma motion across magnetic fields. *The Physics of Fluids*, 3(6):961–965, 1960. 22

[Ser19] A. P. Serebrov. Disagreement between measurements of the neutron lifetime by the ultracold neutron storage method and the beam technique. *Physics-Uspekhi*, 62(6):596–601, jun 2019. 15

[Sha71] R. T. Shann. Electromagnetic effects in the decay of polarized neutrons. *Il Nuovo Cimento A (1965-1970)*, 5(4):591–596, October 1971. 8, 11

[SKF+18] A. P. Serebrov, E. A. Kolomensky, A. K. Fomin, I. A. Krasnoshchekova, A. V. Vassiljev, D. M. Prudnikov, I. V. Shoka, A. V. Chechkin, M. E. Chaikovskiy, V. E. Varlamov, S. N. Ivanov, A. N. Pirozhkov, P. Geltenbort, O. Zimmer, T. Jenke, M. Van der Grinten, and M. Tucker. Neutron lifetime measurements with a large gravitational trap for ultracold neutrons. *Phys. Rev. C*, 97:055503, May 2018. 15

[SRA+20] H. Saul, C. Roick, H. Abele, H. Mest, M. Klopf, A. K. Petukhov, T. Soldner, X. Wang, D. Werder, and B. Märkisch. Limit on the fierz interference term b from a measurement of the beta asymmetry in neutron decay. *Phys. Rev. Lett.*, 125:112501, Sep 2020. 9, 17

[Tan19] Wanpeng Tan. Neutron oscillations for solving neutron lifetime and dark matter puzzles. *Physics Letters B*, 797:134921, 2019. 15

[W+19] X. Wang et al. Design of the magnet system of the neutron decay facility PERC. *EPJ Web Conf.*, 219:04007, 2019. 44

[WAH+57] C. S. Wu, E. Ambler, R. W. Hayward, D. D. Hoppes, and R. P. Hudson. Experimental test of parity conservation in beta decay. *Phys. Rev.*, 105:1413–1415, Feb 1957. 8, 10

[Wei20] Wanchun Wei. A new neutron lifetime experiment with cold neutron beam decay in superfluid helium-4. *Journal of Physics G: Nuclear and Particle Physics*, 47(12):125101, oct 2020. 16

[WG11] Fred E. Wietfeldt and Geoffrey L. Greene. Colloquium: The neutron lifetime. *Rev. Mod. Phys.*, 83:1173–1192, Nov 2011. 15

[Wie18] F. E. Wietfeldt. Measurements of the neutron lifetime. *Atoms*, 6(4), 2018. 15

[WKA13] X. Wang, G. Konrad, and H. Abele. $R \times B$ drift momentum spectrometer with high resolution and large phase space acceptance. *Nucl. Instr. Meth. A*, 701:254 – 261, 2013. 29, 50

[Wol] Wolfram Research Inc. Mathematica, Version 12.1. Champaign, IL, 2020. 27

[Y+13] A. T. Yue et al. Improved determination of the neutron lifetime. *Phys. Rev. Lett.*, 111:222501, Nov 2013. 15

[Z+20] P.A. Zyla et al. (Particle Data Group). *Prog. Theor. Exp. Phys. 2020, 083C01*, 2020. 8, 10, 13, 14, 15

Acknowledgements

This exhausting yet exciting adventure would not have been possible without the loving support of my dearest friends and family. First, I want to thank Kathi Luftensteiner for her unconditional love, support and understanding. When things were rough, she always knew how to set my mind straight again. Also, I want to thank my sister and my parents for their immeasurable support and faith in me.
I like to thank my direct supervisor Gertrud Konrad, who accompanied me for the biggest part of my studies and who honed my skills with immense dedication. Her passion for physics inspires me.
I like to thank my supervisor Eberhard Widmann, who laid the foundations for me to grow and prosper in this wonderful environment that is the Stefan-Meyer Institute (including its people) and who supported me more than is customary.
I like to thank Martin Fertl and Albert Young for examining this thesis.
I also like to thank my colleague Waleed Khalid, who was a refreshing change in our group. He could always spice things up. I cordially thank him for prove reading my thesis and for all the interesting discussions.
Manfred Valentan, Raluca Jiglau and Harald Fillunger were wonderful parts of the NoMoS group and I want to thank them for all the hilarious moments and interesting discussions.
Thank you to Ferenc Glück with whom I had various interesting discussions and who provided me with a significant tool for this work.
Thanks to Aaron Capon for prove reading this thesis with an independent perspective.
Finally, I want to thank all my friends, who brightened my days through this adventure.